Novel Binary Calcia-Alumina Systems

for

Device Applications

MARJAN ZAHEDI

SCHOOL OF ENGINEERING AND MATERIALS SCIENCE

QUEEN MARY, UNIVERSITY OF LONDON

A THESIS, SUBMITTED IN FULFILMENT OF THE REQUIREMENTS FOR THE DEGREE

OF PHILOSOPHY OF THE UNIVERSITY OF LONON

September 2009

DECLARATION

I hereby declare that the work carried on and presented in this thesis for the degree of philosophy is original and entirely my own work and that it has not been submitted as an exercise for a degree at any other university.

MARJAN ZAHEDI

This thesis is dedicated to my parents

Mohammad Zahedi

&

Maryam Sadeghi

ABSTRACT

The room temperature sol-gel processing technique was employed for the first time in the present work to fabricate the novel binary compound of the calcia-alumina (C12A7) system consisting of calcium oxide (CaO) and aluminium oxide (Al_2O_3) in a 12:7 ratio. The highest level of homogeneity and transparency of the C12A7 solution in ethanol was achieved by optimizing pH values, reaction dynamics and modified precursor structures. Studies were performed on this binary oxide in both thin film and powder forms. By using High Temperature X-Ray Diffraction (HTXRD) and Simultaneous Thermal Analyzer (STA), phase transformations in C12A7 powder were examined in situ under continuous heat treatment from room temperature to 1200°C. The samples were found to be amorphous at room temperature. As the temperature was increased, crystallisation was completed at 1100°C. The purity of C12A7 and the removal of redundant chemical by-products were confirmed by independent Fourier Transform InfraRed (FTIR) and Raman Spectroscopic measurements. C12A7 thin films were spin coated on single crystal MgO <100> substrates and the effect of heat treatment on crystallinity were investigated using XRD. Initial signs of the crystallisation of C12A7 thin film were observed at 800˚C and the complete crystallisation was achieved on heat treatment at 1100˚C for 3 hours. Optical absorption spectroscopy measurements were made in the UV-Visible region and experimental data were analyzed to evaluate the dependence of the band structure of C12A7 crystalline phase on annealing temperature.

ACKNOWLEDGEMENT

I would like to express the deepest appreciation to my supervisor, Professor Asim Ray who has the attitude and the substance of a genius. Without his kindly support and motivation this dissertation would not have been possible.

I would also like to thank Dr Nima Roohpour for his generous help with the measurements and exceptional information whenever I needed.

I am also thankful to Dr Rory Wilson for helping me with the XRD measurements as well as revising my thesis.

Special thanks to my friends and colleagues at Queen Mary, Carlos, Zahra, Shweta, Nandu, Sunil and Ian.

Thank you to Shokofeh, Niaz, Elnaz, Khale Farzaneh, Nima for their love, support and inspiration.

Special thanks to my dearest Shahin for his encouragement and patience.

Sincere thanks to my family in Iran; mum, dad, Mehrdad, Maryam for everything they provided for me to be where I am now.

Lastly, I offer my regards and blessings to all of those who supported me in any respect during the completion of the project.

Table of Contents

List of Figures

List of Tables

Chapter 1

Introduction

This thesis reports the sol-gel synthesis of a mixed oxide material containing calcium and aluminium at an atomic ratio of 12:14. The constituent calcium oxide [CaO] and alumina [Al_2O_3] in the binary compound, $12CaO.7Al_2O_3$ (C12A7), traditionally belong to ceramics such as porcelain and cements. They are commonly used as abrasive materials due to hardness and refractory materials due to high melting point. C12A7 has a nano-sized cage structure with free oxygen anions randomly distributed inside the cages. Replacing these free oxygen anions with electrons through special treatments, C12A7 can be converted into electronic conductor resulting in the incorporation of electrons inside its cages [1].

Recent advances in electronic/optoelectronic industries such as internet systems, mobile phones, electronic educational systems as well as electronic games have urged the development of new and novel microelectronic devices to enhance the performance of these systems. Metal oxides are commonly employed as the passive and active layers and unique functionalities can be induced into these groups of

materials through manipulation of their crystal and electronic structure [2]. This concept is of great importance since the demand for emerging applications such as high transparency systems, electrically, thermally or optically smart devices and new energy conversion systems is increasing dramatically. Most oxide materials are known to be electrically insulating, while there are a limited number of them that are intrinsically conductive. With the introduction of dopants, it is possible to achieve high electrical conductivity (up to $\sim 10^4\ Scm^{-1}$) for these oxides while keeping their optical transparency (up to ~ 80-90%) [3]. Some potential applications include fully transparent high performance transistors, Ultraviolet (UV) Light Emitting Diodes (LED) [4], invisible circuits (optoelectronics) [3], flat-panel displays, solar cells [5] and energy conservation (smart windows) devices [6].

Most of the metal oxides discovered up to present have almost similar behaviour and require similar treatment for the emergence of electrical and optical functionalities. For this purpose the present work is concentrated on a completely different metal oxide with unique insulating, semiconducting and metallic-like conducting characteristics. C12A7 conceptually follows a different route for its induced conductivity. This conductive oxide belongs to a new class of novel materials known as "electrides" [7-9].

The characteristic features of electrides are connected structural cavities, wide band gap and near-metallic electronic conductivity [10-13]. All these features can be observed in conductive C12A7. If all the O^{2-} ions are eliminated from the cages and replaced with electrons, then such C12A7 with the maximum electron concentration

of $\sim 2.3 \times 10^{21}\ cm^{-3}$ can be regarded as an electride [14-17]. The conductivity of the final conductive C12A7 prepared varies depending on the parameters defined for the conversion treatment. The maximum conductivity reported at room temperature is $\sim 1500\ Scm^{-1}$ [18], [19]. Apart from its application as an electride, C12A7 can exhibit other novel characteristics if active anions are substituted for the free oxygen ions. Some of these characteristics include strong oxidation, efficient field-extraction of O^- ions to vacuum [20] and light induced insulator-conductor conversion (applicable for direct optical patterning of transparent electronic circuits on the insulating media) [21].

The emphasis of the present investigation is to establish synthetic route of C12A7 through the sol-gel technique. This thesis is organized into seven chapters. The following chapter gives a comprehensive account of the crystal structure of C12A7, potential applications and the synthesis techniques such as solid-state reaction at high temperature [22], [23], plasma laser deposition [24], [25], melt-solidification process [26]. No attempt has been reported for the fabrication of C12A7 via room-temperature sol-gel technique. Sol-gel is a simple and low-cost method that can be adapted for preparing thin films as well as single powders with high purity and precise control of the chemical composition [27-29]. Experimental methods for the fabrication of sol-gel derived C12A7 sample and post-deposition characterisation are presented in chapter 3, discussing principal parameters defining the quality of the final sol. The chemical, thermal, elemental and structural characterisation techniques have been employed to elucidate the nature of the reactions and phase

transformations of this synthesis process from the first stage of solvent addition to the final stage of crystalline phase formation. Chapter 4 is devoted to the Fourier Transform InfraRed (FTIR) and Raman Spectroscopic measurements on C12A7 before and after heat treatment. The results are analyzed to interpret the chemical reactions during the sol-gel process. Chapter 5 is concerned with the investigation into elemental and structural changes, as well as the phase transformations during the thermal treatment of as-deposited samples. Optical absorption is an effective tool to define band structure of the material. UV-Visible absorption spectra are discussed in chapter 6 for C12A7 thin films heat treated at different temperatures and a satisfactory agreement between our experimental and reported theoretical results is found to exist. The thesis is concluded with giving a summary of principal observations and outline of future work.

Chapter 2

Nanoporous C12A7 oxide

C12A7 is a transparent material having a unique crystal structure. It can be formulated as a single crystal, single powder, bulk pellet or thin film. This chapter gives a comprehensive review of the reported work on the crystal structure and the preparation techniques. Electrical, optical and emission properties of this binary compound are sensitive to the post-fabrication treatments. These attributes are critically examined in this chapter.

2.1 Crystal Structure

The CaO-Al_2O_3 phase diagram is composed of a series of binary compounds which are formed at various CaO to Al_2O_3 weight percent ratios [30-32]. As illustrated in figure 2.1, C12A7 is one of these binary compounds and melts congruently at 1392°C [23], [33], [34]. This nanoporous material is a typical insulating oxide and is famous as a good refractory material [16], [35].

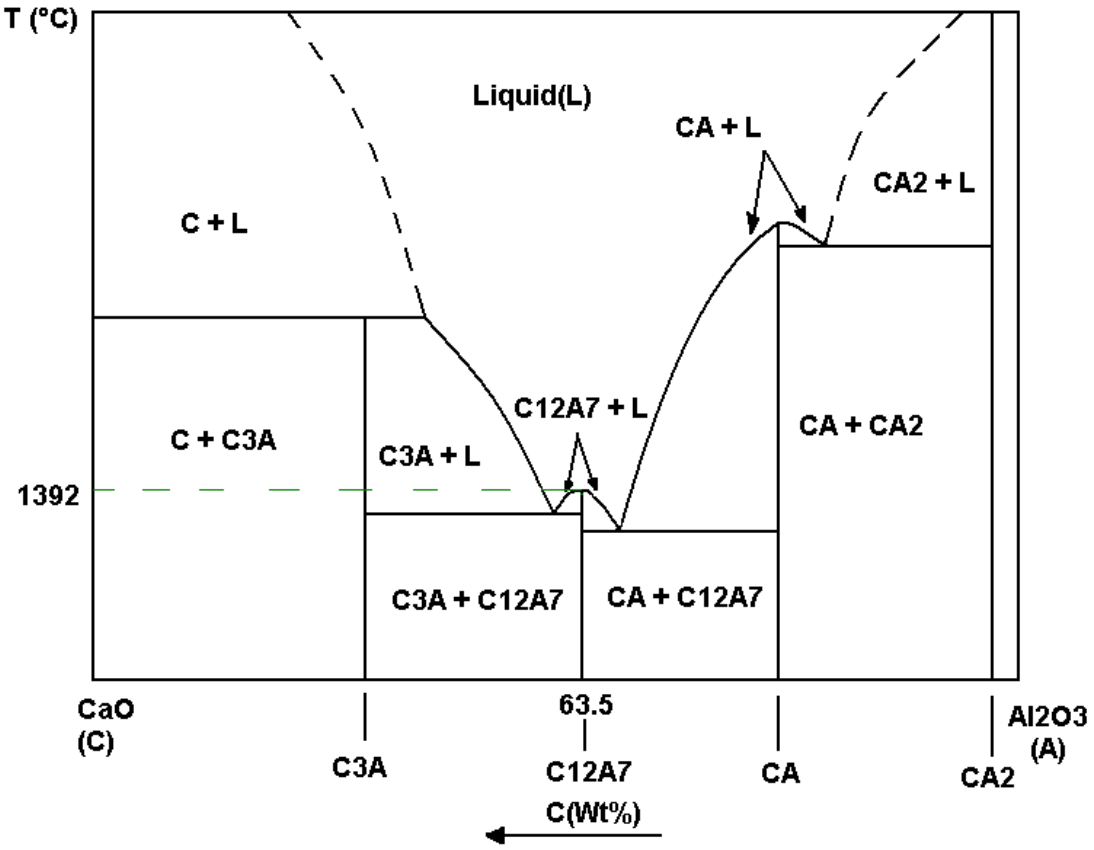

Figure 2.1: Binary phase diagram of CaO-Al2O3, showing CA, C3A, CA2 and C12A7 as stable binary compounds [36]

The crystal structure of C12A7 has a cubic lattice, belonging to the space group $I\bar{4}3d$ with a lattice constant of 1.199 nm [19], [37]. The stoichiometric formula for this 118 atom unit cell (Z=2) is $[Ca_{24}Al_{28}O_{64}]^{4+}+2O^{2-}$, the former denotes the positively charged framework containing 12 crystallographic nanocages with a free space of ~ 0.4nm in diameter and the latter are 2 extra O^{2-} ions , referred as “free oxygen ions” or “excess oxygen ions”. The entrance of the cage is about 0.1nm in

diameter controlling the mass transport between the inner cage and the outside [38-40]. Figure 2.2 shows the structure of one cage.

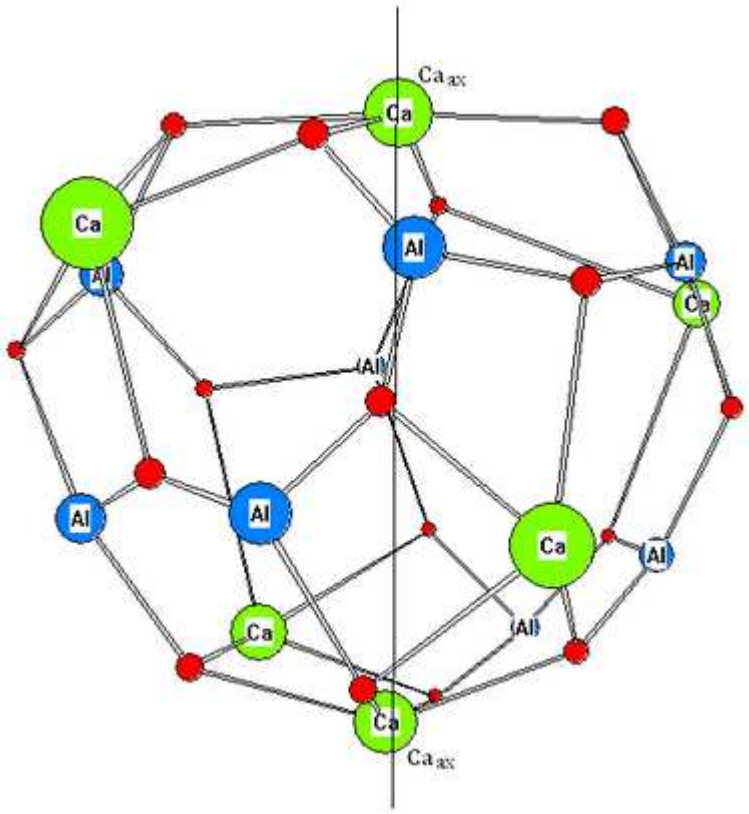

Figure 2.2: Structure of an empty C12A7 cage drawn using chemdraw, composed of 30 individual atoms, some of which will be shared with the neighbouring cage. The unnamed circles represent oxygen atoms.

As illustrated in figure 2.2, each cage is a combination of six Ca, eight Al and 16 O atoms. The two Ca atoms referred as Ca_{ax} are known as “axial Ca”. These Ca atoms

occupy the two poles of the cage on the opposite sites, defining an S_4 symmetry within the cage. The 12 cages present in each unit cell are divided into three groups of four cages. The difference between each group is the direction of the S_4 symmetry axis along x, y and z. These groups are shown in figure 2.3 (a) as S_{4x} , S_{4y} and S_{4z}. Each of these groups is subdivided into two groups. While the two cages in each subgroup carry the same chirality, they form a body-centred cubic (bcc) lattice. Thus, each unit cell is composed of six interlocked bcc lattices of interconnected cages, forming the positively charged framework. In this unit cell each cage is coordinated by eight near neighbour *(nn)* cages and four next near neighbour *(nnn)* cages. Such an arrangement is similar to close packing of spheres, except that in C12A7 each cage shares its opening wall with other neighbouring cages. Each of these cages has a mean effective charge of $(^{+1}/_{3}) = (^{4}/_{12})$ [41].

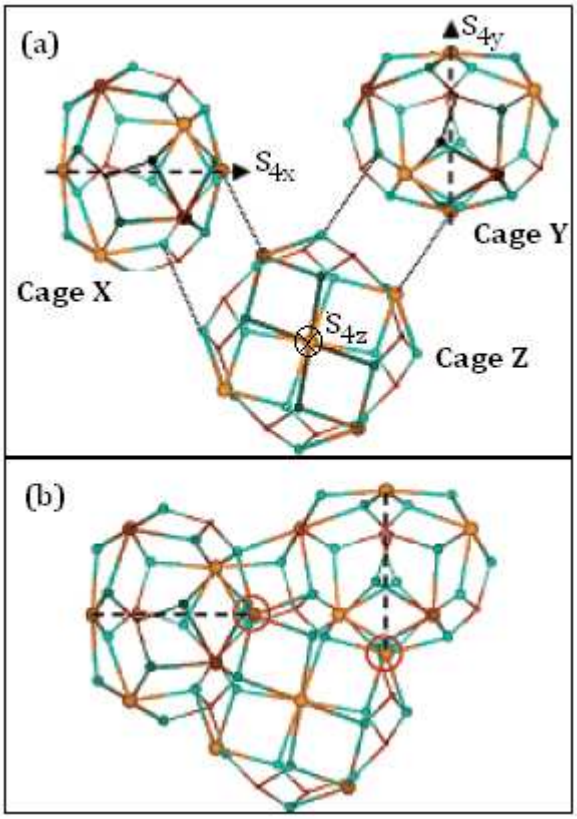

Figure 2.3: C12A7 framework structure: (a) three neighbouring cages belonging to S_{4x}, S_{4y} and S_{4z} symmetrical groups. (b) the same cages after interconnection. Cages X and Y are near neighbour (nn) to cage Z and next near neighbour (nnn) to each other [41]

To compensate for the positive charge of the cage framework, two free oxygen ions are clathrated in the unit cell (this means one in every six of the cages accommodate one O^{2-} ion to maintain the charge neutrality of the crystal [41]. This feature is a zeolite-like one, in which O^{2-} ions are trapped in a Ca-O-Al cage in the stoichiometric composition. This means that the oxide can absorb water over a wide

range of temperatures without a major change of the structure, which is the characteristic of a zeolitic phase [31].

The sum of the ionic radius of the free oxygen ion and Ca^{2+} cation is ~ 0.24nm, but the inter-ionic spacing between these two ions is about ~ 0.36nm, that is 1.5 times longer than the sum of their ionic radii [10]. This indicates that the oxygen ions are loosely bound in the cage; therefore they can be replaced with other monovalent anions with similar ionic radii to the cage size, such as OH^-, F^-, Cl^-, O^- and H^- ions. This substitution leads to the appearance of novel functions such as; strong oxidation [20], ultraviolet (UV) light induced electronic conduction [21] and efficient electron emission [2].

2.2 Synthesis of C12A7

Extensive studies of different aspects of C12A7 with a wide range of applications have urged scientists to introduce new fabrication techniques which would satisfy the requirements for each application. According to each method the final product is single powders, single crystal, thin film or bulk pellet. In the following discussion a brief description for the most effective techniques will be provided.

2.2.1 Single powders

Fabrication of C12A7 single powders using the conventional powder processing techniques requires a solid-state reaction at high temperature. For such processing, $CaCO_3$ and γ-Al_2O_3 powders should be mixed in 12:7 stoichiometric ratio. In the next step the mixture will be fired at temperature ~1100-1350°C in O_2 gas flow for 24hrs. As a result C12A7 powders will be formed. In the final stage these powders will be ground to fine powders [22]. Despite the simplicity of this technique, the high firing temperature is a critical issue, urging scientists to develop a more practical fabrication method which is also capable of being utilized at a much lower temperature. This technique will be discussed in the following.

Tas (1998) succeeded in preparing C12A7 powders at low temperature using a self-propagating combustion method. Calcium Nitrate $Ca(NO_3)_2$ and Aluminium Nitrate $[Al(NO_3)_3]$ powders were mixed in appropriate stoichiometric ratio, and dissolved in distilled water. Urea $[CH_4N_2O]$ was added to the solution as the igniter. If this liquid mixture is exposed to temperature of 510±10°C, within 15 minutes a self-propagating combustion process will take place, which will instantaneously increase the temperature to ~1300°C. The combustion product will be a foamy precursor that is ground to fine powders [30].

In order to investigate the nature of the ignition, it is necessary to study the reaction of each of the elements when heated to the temperature of ~500°C. It is reported that at temperatures higher than 700°C the metal nitrate solution will

decompose, producing nitrous oxides such as NO_2, NO and N_2O_5. Similarly urea will also decompose to biuret (H_2N-CO-NH-NH_2, i.e., $C_2H_5N_3O_2$), cyanuric acid (HCNO) and ammonia (NH_3) when heated to ~200°C. This decomposition is followed by decomposition of biuret itself at temperatures just below 300°C. As a result, the aqueous mixture of metal nitrates and urea will decompose at ~500°C. At this stage, some products that are in the gaseous phase will spontaneously ignite at temperature of ~500°C. Ignition will increase the temperature of the dried foam produced to ~1300°C, leading to the formation of C12A7 single phase [30].

After producing the C12A7 single phase, another heat treatment should be conducted in order to crystallise the amorphous phase formed. The crystallisation of C12A7 powders starts at a temperature of ~600°C. Additional heating up to 1000°C only improves the extent of crystallisation achieved.

2.2.2 Single crystal

Watauchi et al (2002) fabricated C12A7 single crystals using a so-called "Floating Zone Method". For this purpose C12A7 powders were used as the primary materials. These powders are initially formed into a rod to be utilized as a feed rod in the single crystal growth. The feed rod is sintered at a temperature of 1250°-1300°C for 12 hrs in an oxygen flow. Using a similar rod as the seed crystal, the C12A7 single crystal is grown in a four-mirror type infrared-heating furnace [33].

Although C12A7 is a congruently melting compound, samples manufactured using this technique are reported to have many bubbles and cracks appearing in the grown single crystal. The possible reasons for these cracks and bubbles are the concave shape of the solid-liquid interface between the molten zone and the grown crystal due to the transparency of C12A7 as well as the growth rate being higher than the optimum. In fact the density difference between the crystalline phase (2.69 g/cm^3) and the liquid phase (2.92 g/cm^3) is also reported to cause the appearance of cracks at the interface. The centre of this concave interface is an ideal point for the accumulation of small bubbles which can then coalesce into big bubbles. During crystal growth the infrared light that is used to melt the feed rod can easily penetrate the grown crystal. As a result the centre area of the grown crystal will be at a higher temperature compared to the interface, causing expansion at this centre point [33].

To modify the shape of the interface from concave to convex, *Watauchi et al* (2002) suggested the insertion of an alumina tube at the centre of the heated area, so as to act as a heat sink in the grown crystal region. As a result there will be an almost uniform temperature throughout the growing crystal and its surface. By optimizing the position of this alumina tube it is possible to obtain a convex shape at the interface. Such conversion as illustrated in figure 2.4 is believed to reduce the number of both cracks and bubbles drastically. In addition, decreasing the growing rate to < 0.3 (mm/hr) can significantly reduce the bubbles formation [33].

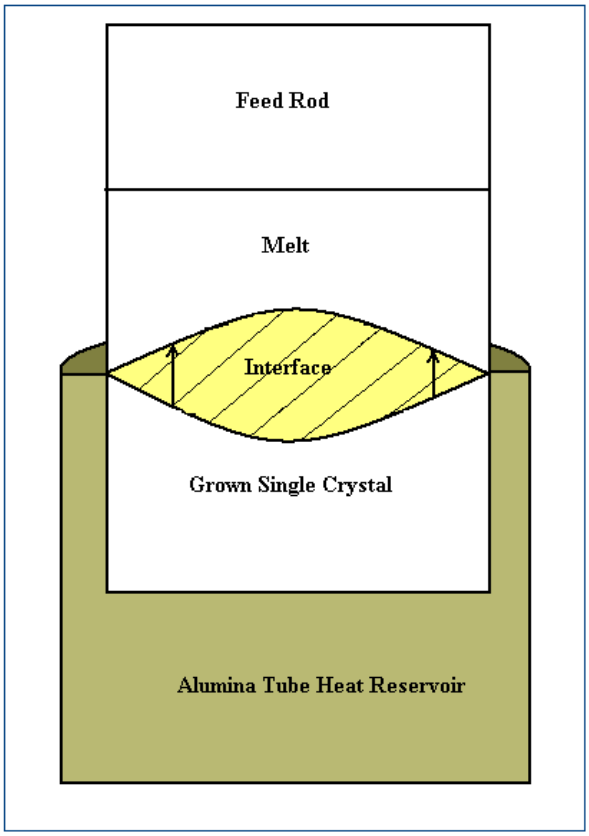

Figure 2.4: Insertion of alumina tube and the conversion of the interface from concave to convex shape, as shown with arrows

2.2.3 Bulk pellet from melt

Although it is always possible to fabricate ceramic materials from a melt-solidification process, powder processing is usually the method preferred for these materials. This is not only because of the sintering temperature that is much lower compared to the melting temperature, but also to avoid the excess grain growth. Such excess grain growth of the crystallised phase causes cracks in the bulk material fabricated [42].

Sakamoto et al (2006) fabricated C12A7 bulk material by melting and solidifying $CaCO_3$ and Al_2O_3 powders in an arc imaging furnace. The powders were dissolved in ethanol for preparing a homogenous mixture. The solution was left at 80°C for 1 day for the evaporation of ethanol. This stage is followed by an annealing at 830°C for 15 minutes. The samples are free of cracks at this stage. But if they are treated for thermodilatometry analysis, then many cracks appear on the samples. The cracks appearance can be ascribed to the residential thermal stress caused by quenching [42]. There has not been any attempt to modify the parameters in this process.

2.2.4 Thin film

In the formation of a thin film of any material the most critical parameter is the substrate. This parameter is more important if the thin film requires high annealing temperature. C12A7 crystallization temperature is ~1100°C, making the substrate options limited.

Teda et al (2003) examined different substrates that seemed to be good candidates for C12A7 deposition. They used SiO_2 glass and single crystals of sapphire (0001), Y stabilised ZrO_2 (YSZ) (100) and MgO (100) as the candidate substrates. The only substrate that resulted in the satisfactory formation of C12A7 thin film was MgO (100) single crystal. It is noteworthy that the film deposited did not show any specific grain orientation with respect to the MgO substrate. Other substrates reacted with the CaO component of the C12A7 film during crystallization, producing

second phases; $CaSiO_3$ on quartz glass, $CaAl_2O_4$ on sapphire and $CaZr_4O_9$ + Al_2O_3 on YSZ, as confirmed by XRD measurements. Figure 2.5 shows the XRD pattern of C12A7 thin film on different substrates. Therefore MgO is the appropriate substrate for thin film deposition of C12A7. The deposition technique used for this investigation is Pulsed Laser Deposition (PLD). As reported, C12A7 pellets are used as the target material where thin films are deposited on different substrates [43].

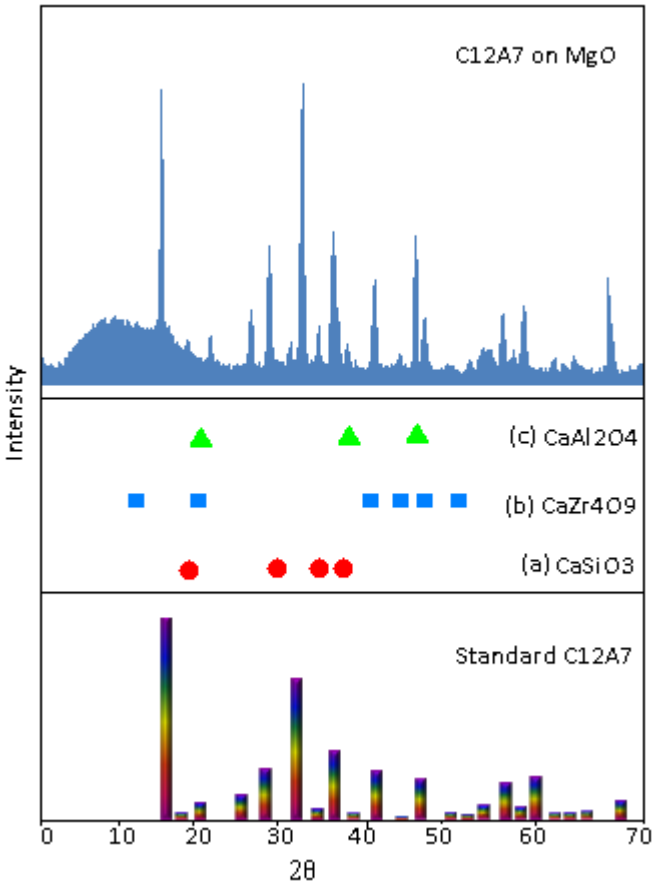

Figure 2.5: XRD spectra of C12A7 film (a) standard, (b) on MgO <011> single crystal. Symbols indicate peak positions for ● Silica, ■ YSZ<100>, ▲ Sapphire <0001> as substrate

Goktas et al (1994) tried using sol-gel processing techniques to fabricate different compositions in Calcia-Alumina systems. However, the closest compound to C12A7 being produced was a mixture of C12A7 and C3A. This is not surprising since a 50C.50A (wt %) composition starting blend was used, with the main focus being merely on the formation of different calcia-alumina compositions and not just C12A7 itself. Nonetheless more than 8 times the amount of C12A7 was formed than C3A, presumably since the 50C.50A (wt%) gel is quite close in composition to the C12A7 crystalline phase. This was the only attempt to fabricate sol-gel C12A7 thin film [36].

2.3 Ion doping in C12A7

As stated earlier, the framework of the C12A7 crystal is composed of 116 atoms in the form of 12 Ca-O-Al cages, which is capable of taking up two O^{2-} ions into its structure. The cages have an entrance of 0.1nm in diameter, which controls the elemental substitution within the cages. Only a limited number of ions meet the criteria to be replaced by the oxygen ions, inducing a wide range of characteristics into this oxide material [20]. Such characteristics have inspired materials scientists to develop novel properties in this oxide. Here a brief introduction to some of the most significant substitution processing is presented. A complete discussion of each of these processes lies out of the scope of this project.

2.4 C12A7 bearing oxygen ions

Synthesis of C12A7 samples in air incorporates O^{2-} ions as the majority ions in the cages. In order to implant O^- and O_2^- ions in the nanocages, a simple heat treatment should be conducted in a dry oxygen atmosphere at a temperature between 600-800°C [10], [44]. The mechanism for such substitution in the first stage involves the diffusion of oxygen molecules from the atmosphere into the cages of C12A7. In the next stage the encaged O_2 reacts with O^{2-} to form O^- and O_2^-, which is outlined in the reaction below:

$$O^{2-}(\text{cage}) + O_2(\text{gas}) \Rightarrow O^-(\text{cage}) + O_2^-(\text{cage})$$

If the heat treatment conditions are optimised it is possible to have the maximum concentration of $\sim 2X10^{21}$ (cm^{-3}) for the O^- ions in the cages. It should be noted that if, instead of using a dry oxygen atmosphere, the post-annealing is conducted in a flowing air atmosphere, the concentration of O^- ions will decrease drastically. Such a decrease is attributed to the reaction between O^{2-} and H_2O (in the air) leading to the consumption of free oxygen ions (O^{2-}) [45], [46]:

$$O^{2-}(\text{cage}) + H_2O(\text{air}) \Rightarrow 2OH^-(\text{cage})$$

Two properties that are the most characteristics of O^- + O_2^- doped C12A7 are reported to be strong oxidizing properties as well as O^- ion emitter under DC electric field, as will be discussed below.

2.4.1 The strongest oxidant

It is believed that O^-, O_2^- and O_3^- are the most active oxygen species in the oxidation of hydrocarbons or biochemical reactions. The highest reactivity among these belongs to O^- as the strongest oxidizing agent [46], [47]. It has been reported that if high concentrations of O^- ions are incorporated into C12A7 this oxide compound can even oxidize Platinum (Pt). As shown in figure 2.6, *Hosono et al* (2004) introduced the oxidization of Pt foil in contact with C12A7: O^- + O_2^- into Pt^{4+} under heat treatment at temperatures higher than 1000°C in air [46].

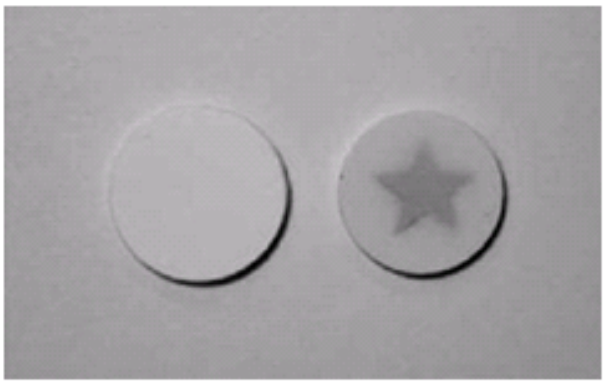

Figure 2.6: C12A7 pellets sintered in wet air (left) and in dry oxygen (right). Star-shaped Pt plates were placed in contact with the samples. Dark star shape is due to the formation of Pt^{4+} [46]

2.4.2 O^- Ion Emitter

It has been confirmed that if an external DC electric field is applied to C12A7: $O^- + O_2^-$ under vacuum; a monochromatic O^- ion beam will be emitted from the material. Such emission shows a maximum current density of 2.74 (μAcm^{-2}) which is three times higher than the maximum value recorded for the conventional Y- stabilised ZrO_2 (YSZ) [48].

YSZ is reported to exhibit thermionic O^- ion emission; however its emission current is limited to nanometre level at maximum. The main disadvantage of YSZ is that in order to dissociate O^{2-} ions into O^- ions and electrons it needs a surface metal electrode such as Pt which will result in the emission of electrons as well as O^- ions [48].

In C12A7 bearing $O^- + O_2^-$ due to the presence of extremely high concentrations of O^- and O_2^- ions, and the fast ionic conductivity in C12A7 itself means that the O^- ions will be extracted from the surface directly. Emission from C12A7: $O^- + O_2^-$ starts when the O^- ions migrate from the bulk crystal onto the sample surface by field-enhanced thermal diffusion and are then desorbed into space to form gas phase anions of O^- . There is also a negligible amount of electron emission from the surface. There is a strong correlation between the O^- ion emissions from C12A7: $O^- + O_2^-$ and the surface temperature as well as the applied extraction field [25], [44], [48]. A Complete discussion of this subject is not considered in this work.

2.5 A reversible semiconductor

As a suitable monovalent anion to replace O^{2-} free ions, H^- ions can be incorporated into the C12A7 bulk crystal. By such replacement we can expect a variety of novel electronic, optical and ionic properties in C12A7:H^-. Here we will discuss various incorporation techniques involved while exploring the main characteristics of this new semiconducting oxide.

2.5.1 Heat Treatment in H_2 Atmosphere

This method involves annealing the as-prepared sample in a hydrogen atmosphere (20% H_2 – 80% N_2), at a temperature of 1300°C for 1 hour. The samples for such treatment can be thin films, single crystals or polycrystalline powders. At this stage the sample would keep its original colour with conductivities less than 10^{-10} Scm^{-1}. Subsequent illumination of C12A7:H^- with UV light results in the conversion of C12A7:H^- into a conductive oxide with conductivities as large as 0.3 Scm^{-1} at room temperature. This conductive state persists even after irradiation ceases and is accompanied by a shift in the colour of the sample from colourless to yellowish green suggesting that the photo excitation of the hydride ions is responsible for the coloration of the sample and that these ions are controlling the absorption in the oxide [49], [50].

As illustrated in figure 2.7 hydride ion implantation results in the appearance of two optical absorption bands at ~2.8eV and ~0.4eV. These bands are attributed to an F^+-like centre that is created by the hydride ion trapped in the cage [2]. A full discussion on the nature of ion entrapment can be found in section 2.3.3.

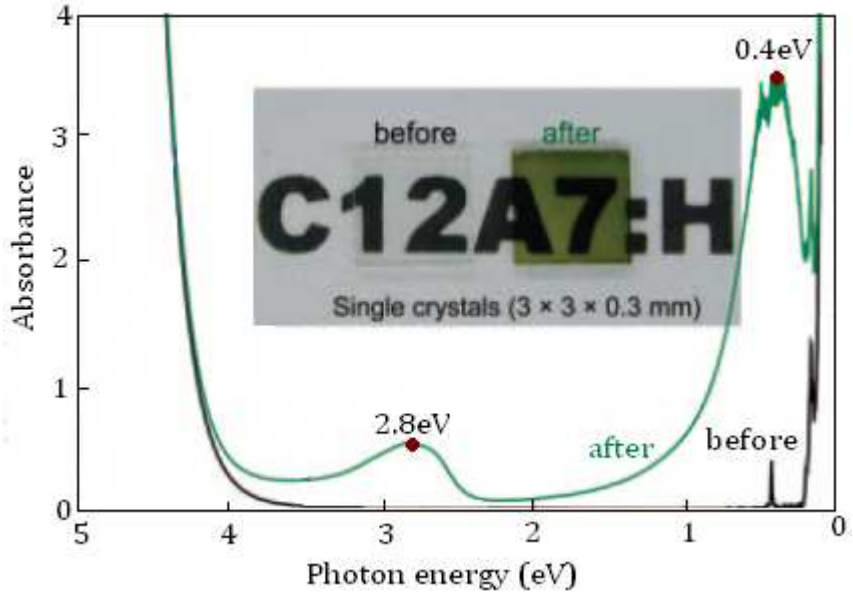

Figure 2.7: The absorption spectra of C12A7:H^- single crystal before and after UV-illumination, Inset is the photo of the sample (0.3mm thick- single crystal) before and after UV-illumination [2]

The mechanism for the conversion of C12A7:H^- from insulator to semiconductor can be explained in the following steps:

1) Incorporation of hydride ions in the cages through the following chemical reaction:

$$O^{2-}(\text{cage}) + H_2(\text{atmosphere}) \Rightarrow OH^-(\text{cage}) + H^-(\text{cage})$$

OR

$$O^{2-}(\text{cage}) + H_2(\text{atmosphere}) \Rightarrow \frac{1}{2}O_2(\text{atmosphere}) + 2H^-(\text{cage})$$

2) The UV irradiation induces the emission of an electron from H^- ions:

$$H^- \Rightarrow H^\circ + e^-$$

During step 1 the O^{2-} ions are replaced for the H^- ions which occupy the centre of the cage. These ions induce an inward relaxation to the cage, in which the axial Ca atoms are displaced towards the H^-, decreasing the Ca_{ax}-Ca_{ax} distance from 5.6A° to 5.0A° [49], [51].

As can be seen in figure 2.8 these hydride ions are stabilized at an energy level of ~1.1eV above the top of the valence band, while the empty cages form a narrow conduction band at ~5.7eV above the valence band. The electrons freed from the hydride ion during step 2 will be well localized within the cage, lowering the cage energy level by ~0.4-1.1eV due to strong lattice relaxation in the same manner as H^- ions. This new energy level for the entrapped electrons is ~2.4-2.8eV below the framework conduction band [52].

In conclusion, the intercage s-to-s transition would introduce the strong absorption peak at ~0.4eV, while the peak at 2.8eV is due to the partially allowed intracage s-to-p transition. The absorption peak at 2.8eV is relatively low in

intensity, confirming that the film is reasonably transparent in the visible region. Figure 2.9 shows these two transitions within cages [49], [50].

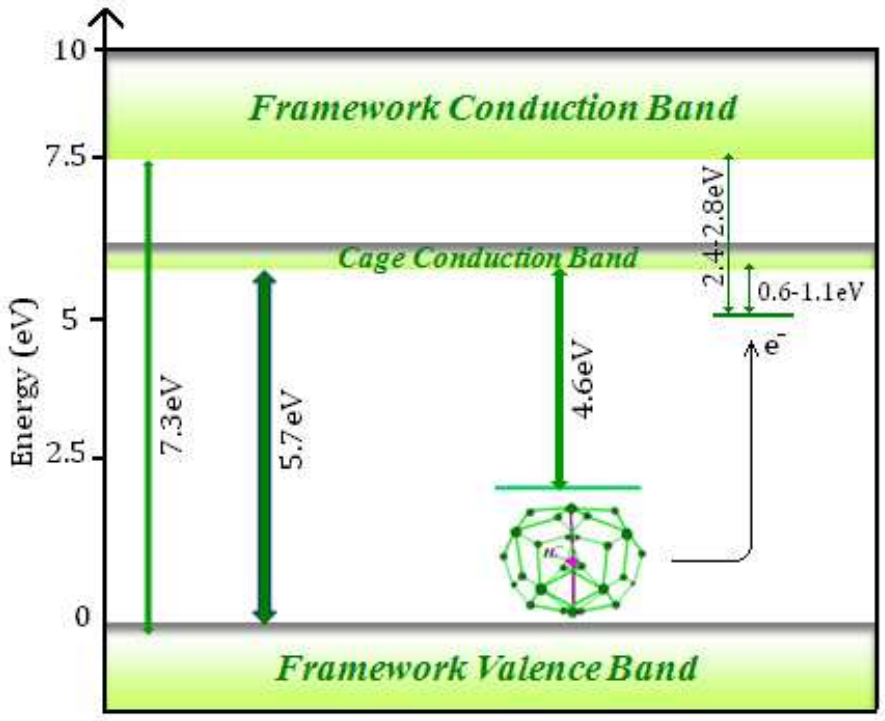

Figure 2.8: Energy diagram of C12A7 showing the $1S^2$ state of hydride ions at 1.1eV above the valence band. The energy level of occupied cages is lowered by ~0.6-1.1eV compared to empty cages

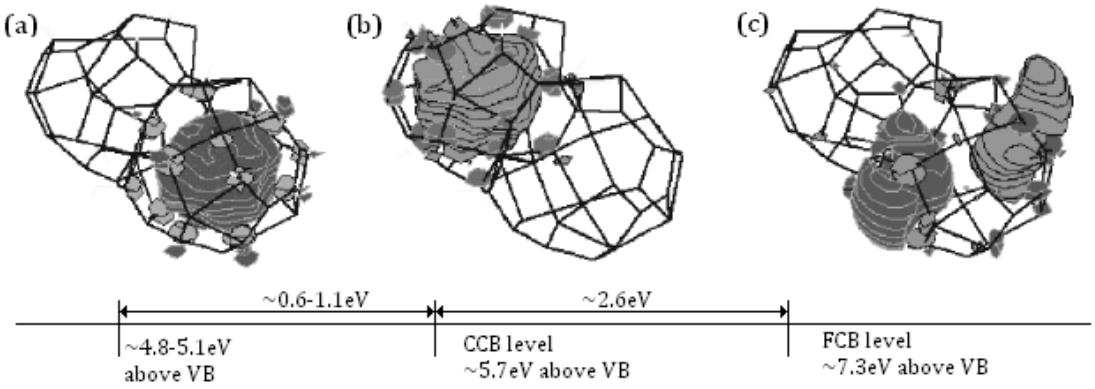

Figure 2.9: Entrapped electron in C12A7 nanocage, (a) in relaxed state, (b) intercage transition and (c) intracage transition [15]

It has been reported that in C12A7:H^- the released electrons can hop between empty cages only in the area exposed to UV irradiation. This suggests that the conductivity channels do not involve empty cages and are formed only in the UV-irradiated area. The untreated hydride ions prevent the creation of such hopping paths. Therefore the released electrons migrate through a well-defined channel: the hopping path. Such behaviour is the basis of the main application of C12A7:H^- for direct optical writing of electric circuits in insulating media (figure 2.10) [53], [54].

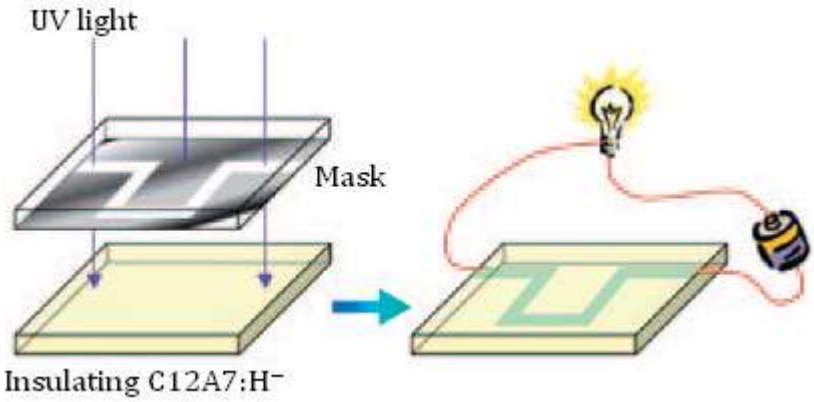

Figure 2.10: Direct patterning of a circuit by UV illumination [25]

It should be mentioned that at temperatures higher than 320°C the H° atoms created in the cages may recombine with each other to form H_2 molecules. As a result of such recombination the optical absorption will decrease rapidly. Further heating to temperatures higher than 550°C causes the release of H_2 gas from the material. Therefore the insulating-conducting conversion of C12A7:H^- is reversible only if the temperature is less than 500°C [21].

2.5.2 H^+ Hot Ion Implantation

Heat treatment in an H_2 atmosphere is a reasonably straightforward method to incorporate hydride ions in C12A7. The process is a chemical equilibrium, which limits the concentration of hydride ions. As a result the highest conductivity that can

be attained via such a process is limited to ~0.3 Scm^{-1}. On the other hand, H^+ ion implantation is a non-equilibrium process. Therefore it is possible to implant much higher concentrations of hydride ions in the crystal, leading to conductivities as high as ~10 Scm^{-1} [15], [55].

It has been suggested that the formation of F^+ -like centres via this method starts at implantation temperatures of ~300°C and increases exponentially at higher temperatures. The concentration of these F^+ -like centres saturates at temperatures of ~600°C. At this temperature the hydride ions are fully incorporated in the cages, showing the saturation. After implantation at this temperature the concentration of OH^- species in nanocages decreases drastically. The mechanism suggested for this incorporation is that the H^+ ion reacts with OH^- species accommodated in the cages to form molecular H_2O. Other H^+ ions occupy empty cages with a positive charge and capture two electrons to maintain charge neutrality of the lattice [56].

By increasing the fluence of implantation, it is possible to obtain higher conductivities at room temperature. The maximum conductivity achieved is ~10 Scm^{-1} corresponding to hydride concentration of ~$7.6X10^{18}$ cm^{-2} [56].

2.6 Room temperature stable inorganic electride

The versatility of C12A7 is such that it is possible to extract the O^{2-} ions from the structure, while trapping their electrons inside the nanocages which can be regarded

as quantum dots. The properties of an electron in such a lattice will resemble the properties of an electron localized in an anion vacancy in, for example alkali halides. These defects known as F^+ -centers exist in a variety of ionic crystals [2]. Moreover in C12A7 the continuous connection of cages as a precursor of F^+-like centers form a pattern similar to close packing of spheres. Such continuous arrangement of F^+-like centers and their high concentrations, facilitate the hopping of mobile electrons between neighboring unoccupied cages, leading to the emergence of high conductivity in this novel oxide. Such characteristic is similar to those observed in electrides [2], [15].

"Electrides" are known as a group of ionic compounds in which anions electrons trapped in a complex array of cavities formed from one or two organic complexants. In these compounds cations are composed of alkali metal ions which provide charge neutrality. The drawback of these organic electrides is their instability at room temperature due to rapid degradation of organic compounds [12], [20]. Unlike these conventional electrides, C12A7:e^- is believed to be stable at room temperature as an inorganic electride with work function as low as 2.4eV [18], [19]. With such unique structure, C12A7 as an electride provides broad or potential applications to nanodevices, mainly as a cold-cathode electron emitter [57].

It should be noted that the intrinsic defect sites (cages) in C12A7 exist at the density of cages (12 per unit cell, corresponds to $7.0X10^{21}$ cm^{-3}). However, the theoretical maximum electron density is reported to be $2.3X10^{21}$ cm^{-3}, indicating that only one third of the cages can be occupied by electrons at maximum [11], [12].

In the following the classical attempts to induce high concentrations of electrons inside C12A7 structure will be discussed.

2.6.1 Heat Treatment in Ca Vapour

Matsuishi et al (2003) reported ~100% replacement of the free oxygen ions with electrons in C12A7 single crystal. The method involves the extraction of the free oxygen ions by a base metal such as calcium via oxide formation. As a result, the electrons will be incorporated in the nanocages. In this method the as-grown C12A7 single crystals should be sealed in silica glass tubes under vacuum together with metal calcium shots and heated at 700°C [20].

According to figure 2.11 Ca treatment will alter the colour of the samples, which change from colourless to green and finally to black. In this treatment all the free oxygen ions are almost exclusively replaced by electrons. The conductivity of Ca treated samples strongly depends on the duration of the treatment. It has been reported that Ca treatment for 4 hours will increase the conductivity from less than 10^{-10} cm^{-1} to 10^{-3} Scm^{-1}. Longer treatment duration will lead to a significant increase in conductivity [34].

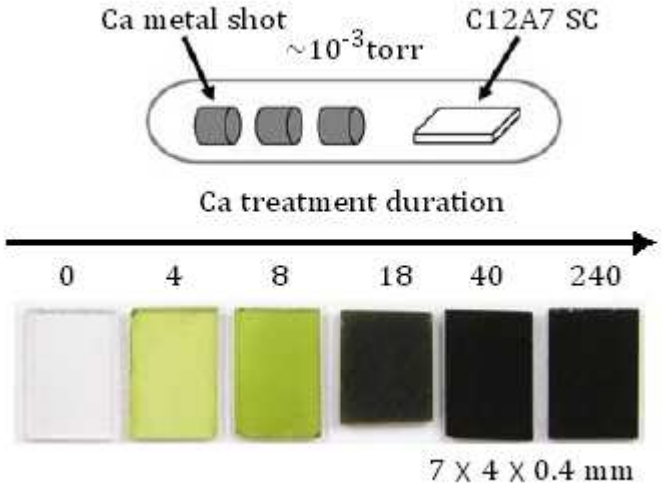

Figure 2.11: C12A7 single crystal after 0, 4, 8, 18, 40 and 240 hours of Ca treatment [34]

The mechanism for such electron implantation can be understood through the following reaction:

$$[Ca_{24}Al_{28}O_{64}]^{4+}(2O^{2-})+2Ca \Rightarrow [Ca_{24}Al_{28}O_{64}]^{4+}(4e^{-})+2CaO$$

As a result Ca atoms will extract free oxygen ions preferentially forming a crystalline CaO layer on the sample surface. This will incorporate electrons inside the nanocages. The electrons migrate throughout the crystal as a polaron, thereby enhancing electronic conductivity in the material.

The formation of CaO layer is the drawback of this method making it inapplicable to thin films. This layer should be removed from the surface of the sample by polishing which may also remove part of the C12A7 thin film. Another disadvantage of this method is the chemical equilibrium nature of the process which requires prolonged timing to achieve 100% efficiency. The maximum conductivity reported through this method is $100 Scm^{-1}$ [34].

2.6.2 Heavy Inert Gas Ion Implantation

In this method C12A7 thin films are exposed to heavy ion bombardment, which results in the extraction of free oxygen ions from the cages. The process is a non-equilibrium physical process which does not require a long time for completion. Furthermore, similar to H^+ ion implantation, the lattice framework shows high tolerance against heavy inert gas ion implantation due to the flexibility of the structure [58], [59].

During implantation electrons will be produced via nuclear collision according to the following reaction:

$$O^{2-}(\text{cage}) \Rightarrow \frac{1}{2} O_2(\text{atmosphere}) + 2e^-(\text{cage})$$

Such nuclear collision is dominant at fluence of greater than $5X10^{17}$ cm^{-2}. At the same time, the OH^- ions that pre-exist in the cages from the post-annealing

crystallization of the amorphous C12A7 will decompose using the kinetic energy of the heavy ions dissipated via electronic excitation. This will create protons in the cages according to the following reaction:

$$OH^-(cage) \Rightarrow O^{2-}(cage) + H^+(cage)$$

To maintain charge neutrality, these H^+ ions will react with the electrons trapped in the cages to form hydride ions according to the following reaction:

$$H^+(cage) + 2e^-(cage) \Rightarrow H^-(cage)$$

After implantation if the number of electrons is higher than the number of protons, they will be incorporated in the cages directly leading to enhanced electronic conductivity without further UV-illumination. In this case the number of hydride ions incorporated in the cages is so little that light illumination will not increase the conductivity. On the other hand if the number of protons exceeds those of electrons, more hydride ions will be formed in the cages. Consequently further light illumination will be required to incorporate electrons [58], [59].

The maximum concentration of electrons that is reported for this method is $1.4X10^{21}$ cm^{-3}, that is 63% of the theoretical maximum concentration with the

corresponding conductivity of 10Scm^{-1}. However, the electron concentration can be controlled precisely by changing the process parameters [58], [59].

2.6.3 Direct solidification in a reducing atmosphere

The heat treatment of stoichiometric C12A7 melt in wet air, where O^{2-} and/or OH^- ions act as templates will lead to the formation of crystalline C12A7 phase. In fact, the formation of C12A7 from melt is markedly affected by the presence of suitable template anions. It is known that the reducing atmosphere has the potential to exclude the extra framework oxygen anion during solidification, simultaneously generating electrons in the cages. However, the solidified product is a mixture of $3CaO.Al_2O_3$ (C3A) and $CaO.Al_2O_3$ (CA) eutectic phases rather than C12A7:e^- due to the lack of a suitable template anion [26], [60].

Kim et al (2006) reported a two step melt-solidification process (figure 2.12) under reducing atmosphere as a simple method to fabricate C12A7:e^- polycrystalline samples.

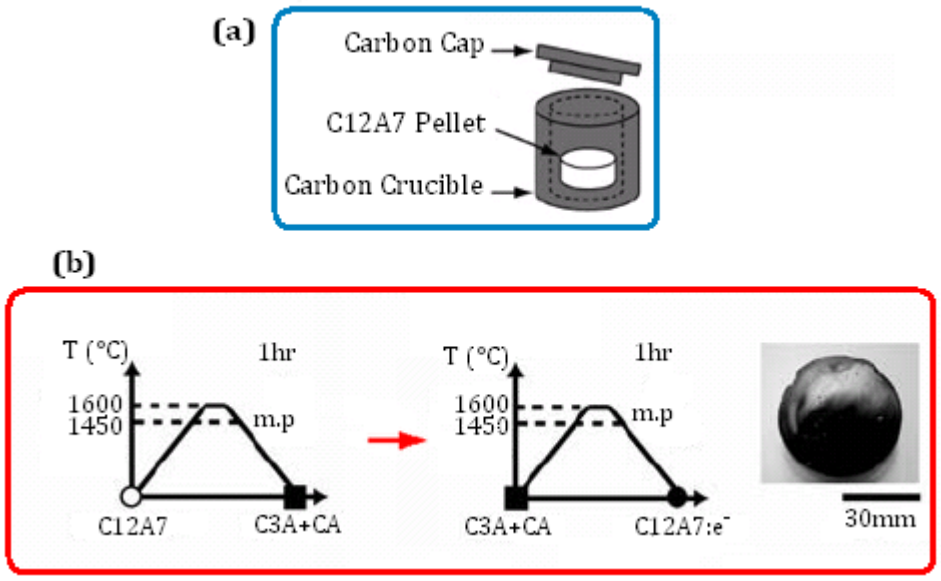

Figure 2.12: (a) Reducing atmosphere in nitrogen gas flow chamber, (b) melt solidification process. The sample undergoes two thermal treatment cycles in which C12A7:e⁻ is produced [20]

In the first step, C12A7 powders are melted in a carbon crucible with carbon cap at 1600°C for 1 hour in air, followed by solidification at 400°C per hour rate. The solidified product will be C3A and CA eutectic phase. In this stage, the free oxygen anions are preferentially excluded due to the reducing atmosphere, although the absence of a suitable template leads to the decomposition of C12A7 into the C3A and CA eutectic phase [26].

In the second step, the C3A and CA eutectic phase melts and solidifies under the same conditions. It has been proven that this heat treatment will introduce C_2^{2-} ions

into the system. The C_2^{2-} ions will be dissolved into the melt from the carbon crucible to compensate for the oxygen deficiency caused by the strongly reducing atmosphere. The ionic radius of C_2^{2-} (1.2A°) is similar to that of the O^{2-} ions (1.4A°), which suggests that the C_2^{2-} anion serves as the template in the reducing atmosphere, instead of the extra framework oxygen ions in an oxidizing atmosphere [26].

At the nucleation stage the cage structure is formed around the C_2^{2-} anions, developing the C12A7 phase. However, during the cooling-down process the C_2^{2-} ions are released from the cages in the form of either C or CO leaving electrons in the lattice. The total electron formation can be expressed by the following reactions:

$$C_2^{2-}(\text{melt}) \Rightarrow C_2^{2-}(\text{cage}) \Rightarrow 2C(\text{solid}) + 2\ e^-(\text{cage})$$

and/or

$$C_2^{2-}(\text{cage}) + O^{2-}(\text{cage}) \Rightarrow 2CO(\text{atmosphere}) + 6\ e^-(\text{cage})$$

The two step melt-solidification process leads to the formation of C12A7:e^-. The concentration of electrons is reported to be ~$3.0X10^{19}$ cm^{-3}. Although this value can be increased up to the theoretical maximum value of $2.3X10^{21}$ cm^{-3}, if the process parameters are optimised. The product is green in colour and exhibits an electrical conductivity of ~5 Scm^{-1} as a result of electron incorporation [26].

2.6.4 Thermal treatment in CO/CO2 gas flow

In this method C12A7 is exposed to a reducing gas atmosphere. For this purpose, CO/CO_2 gas flow is preferred to hydrogen, since thermal treatment in the presence of H_2 is favorable for the formation of H^-, preventing the accumulation of electrons. Consequently the treatment is carried out at 1000-1200°C for 24 hours under nitrogen gas flow, with the sample placed in a carbon crucible with a carbon cap. As a result CO gases react with the free oxygen ions to form CO and CO_2 gases. This creates oxygen vacancies inside the crystal. To compensate for the positive charge of the lattice framework, electrons are ejected into the cages instead of the excited free oxygen ions:

$$O^{2-}(\text{cage}) + CO(\text{gas}) \Rightarrow 2e^-(\text{cage}) + CO_2(\text{gas})$$

The maximum concentration of $\sim 8X10^{19}$ cm^{-3} is obtained through this process leading to conductivities of ~ 4 Scm^{-1} [14], [20].

2.6.5 Reducing via amorphous C12A7 overlayer

Miyakawa et al (2007) could obtain high level of conductivity ($\sim 800 Scm^{-1}$) through a two step pulsed laser deposition (PLD) process. In this approach the thermally treated crystallized C12A7 would undergo a further treatment in the presence of

amorphous C12A7 top layer. This overlayer acts as a chemical reducing layer, working in a manner similar to Ca metal in the Ca-treatment method. It has been suggested that in amorphous C12A7 the oxygen ions can diffuse faster than in CaO. In addition, the thickness of this amorphous layer is much smaller than that of the CaO layer, as a result of which the oxygen ions are more exclusively extracted from the bulk crystal. This allows more electrons to be doped into C12A7 film [60], [61].

The nature of the conductivity as a result of such treatment is completely different than that observed in other techniques. Here we would have metallic conductivity where conduction is governed by band conduction free carriers rather than a semiconducting behavior as observed in other methods. Figure 2.13 compares conductivity for C12A7:e^- obtained from the current method and inert gas ion implantation. As can be seen for the current method there is an indirect relationship between conductivity and temperature, whereas for C12A7:e^- obtained from inert gas ion implantation the conductivity and temperature have a direct relationship [61].

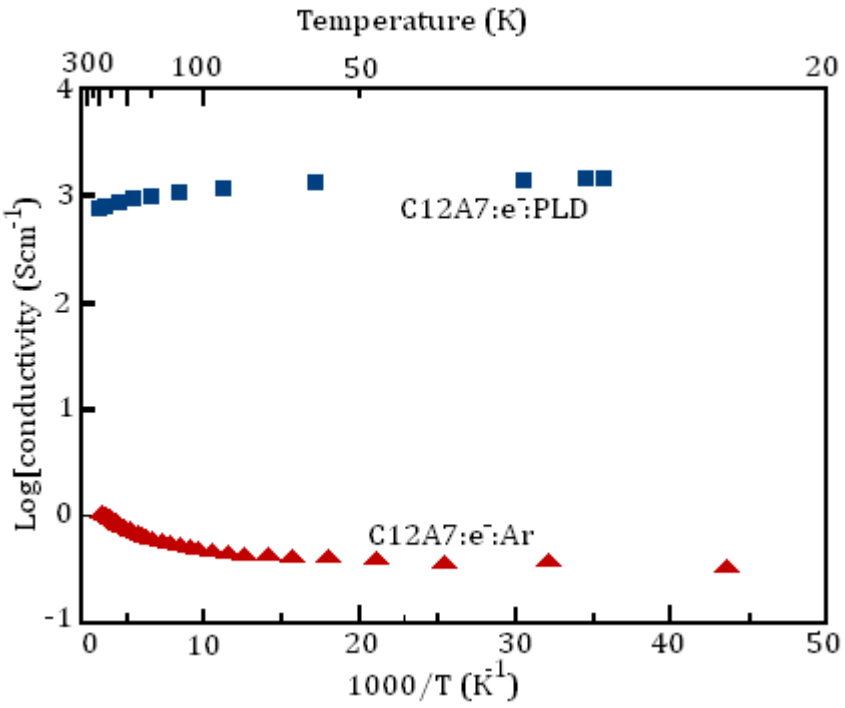

Figure 2.13: Temperature dependence of electrical conductivity in C12A7:e- obtained using amorphous C12A7 overlayer and inert gas ion bombardment [61]

Figure 2.14 shows the optical absorption spectra of C12A7:e- fabricated via this method. As can be seen the 0.5eV peak corresponding to intercage s-s transition that was observed in other types of conductive C12A7 oxides is not distinctly observed. Instead a "Drude-type" absorption profile is observed that corresponds to delocalised free electrons. The peak at 2.7eV corresponding to intracage s-p transitions is still present [61].

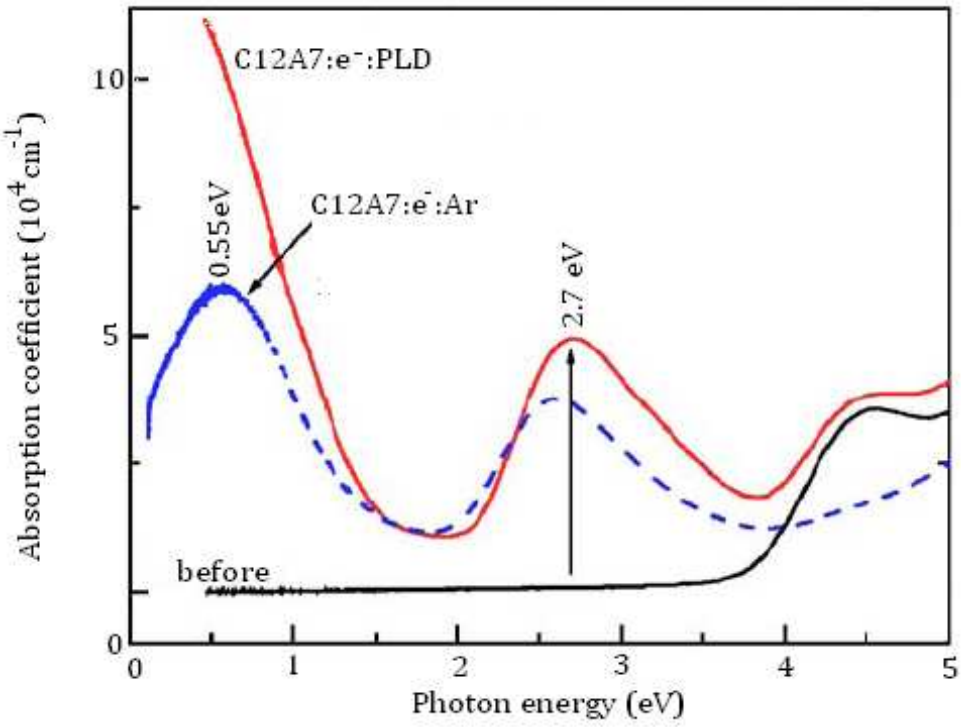

Figure 2.14: Absorption spectra of C12A7:O^{2-} , C12A7:e^-:PLD and C12A7:e^-:Ar [61]

C12A7:e^-:PLD has the potential to be used as the electron emitter in many devices. The electronic emission of this inorganic electride follows two separate mechanisms according to the acceleration voltage applied. As illustrated in figure 2.15, at low extraction voltage (<1000V) the electron emission is controlled by thermionic emission. The emission current increases with temperature and follows the Richardson-Dushman model;

$$I=I_{\circ}\exp\left(\frac{e}{KT}\sqrt{\frac{e\beta V}{4\pi\varepsilon_{\circ}}}\right) \qquad (2.1)$$

Where I_0 is the prefactor, K is the Boltzman constant and ε_0 is the dielectric permittivity of vacuum. At higher voltages (>1500V), the Fowler-Nordheim tunneling model dominates the electron emission;

$$I=A\frac{(\beta V)^2}{\alpha\varphi}\exp\left(-\frac{B\varphi^{3/2}}{\beta V}\right) \qquad (2.2)$$

where A is $1.5X10^{-6}$ $eV.V^{-2}$, B is $6.831X10^{-7}eV^{-3/2}.V.cm^{-1}$, α is the emitting area, β is the structure factor and φ is the work function [2], [26], [57].

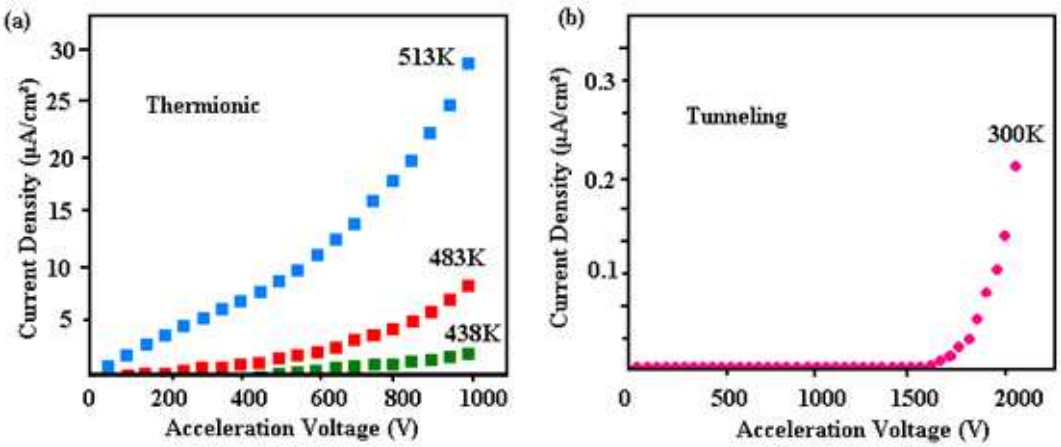

Figure 2.15: Electron emission I-V characteristics for C12A7:e⁻ (a) extraction voltage <1000V and (b) extraction voltage>1500V [2]

Chapter 3

Experimental Methodology

The sol-gel technique was employed to fabricate C12A7 oxide. Crystalline and amorphous phases were obtained depending upon the degree of heat treatment of the pristine sample. This chapter describes the preparation of the starting materials for the sol-gel fabrication and the substrates for thin film deposition. The parameters required to obtain highly crystalline phase are also explained in this chapter. Characterisation techniques employed to investigate the optical, chemical, elemental and thermal properties of both the films and single particles are presented in this chapter.

3.1 Sample Preparation

3.1.1 Sol-gel Processing of C12A7

The components used for the formation of the final C12A7 solution were as follows:

Aluminum sec-butoxide ($Al[OCH(CH_3)C_2H_5]_3$) known as ($Al(OBu)_3$) with purity of 99.99% , Ethyl acetoacetate ($CH_3COCH_2COOC_2H_5$) known as etac with purity of ≥90.0% , Calcium Nitrate Tetrahydrate ($Ca(NO_3)_2 \cdot 4H_2O$) with purity of ≥90.0%, Hydrochloric Acid 1M (HCl) and Ethanol (CH_3CH_2OH) with purity of ≥98.0%, all chemicals were purchased from Sigma Aldrich Chemicals Ltd.

The nominal composition of the C12A7 solution is $63.5CaO - 36.5Al_2O_3$ (wt %). C12A7 sol was prepared through the hydrolysis of two separate solutions. The first solution is prepared using aluminum sec-butoxide as the precursor, forming boehmite particles through as series of chemical reactions. The calcia particles are formed in the second solution which uses calcium nitrate as the precursor. Figure 3.1 illustrates how hydrolysis of two initial precursors would lead to the formation of C12A7 sol.

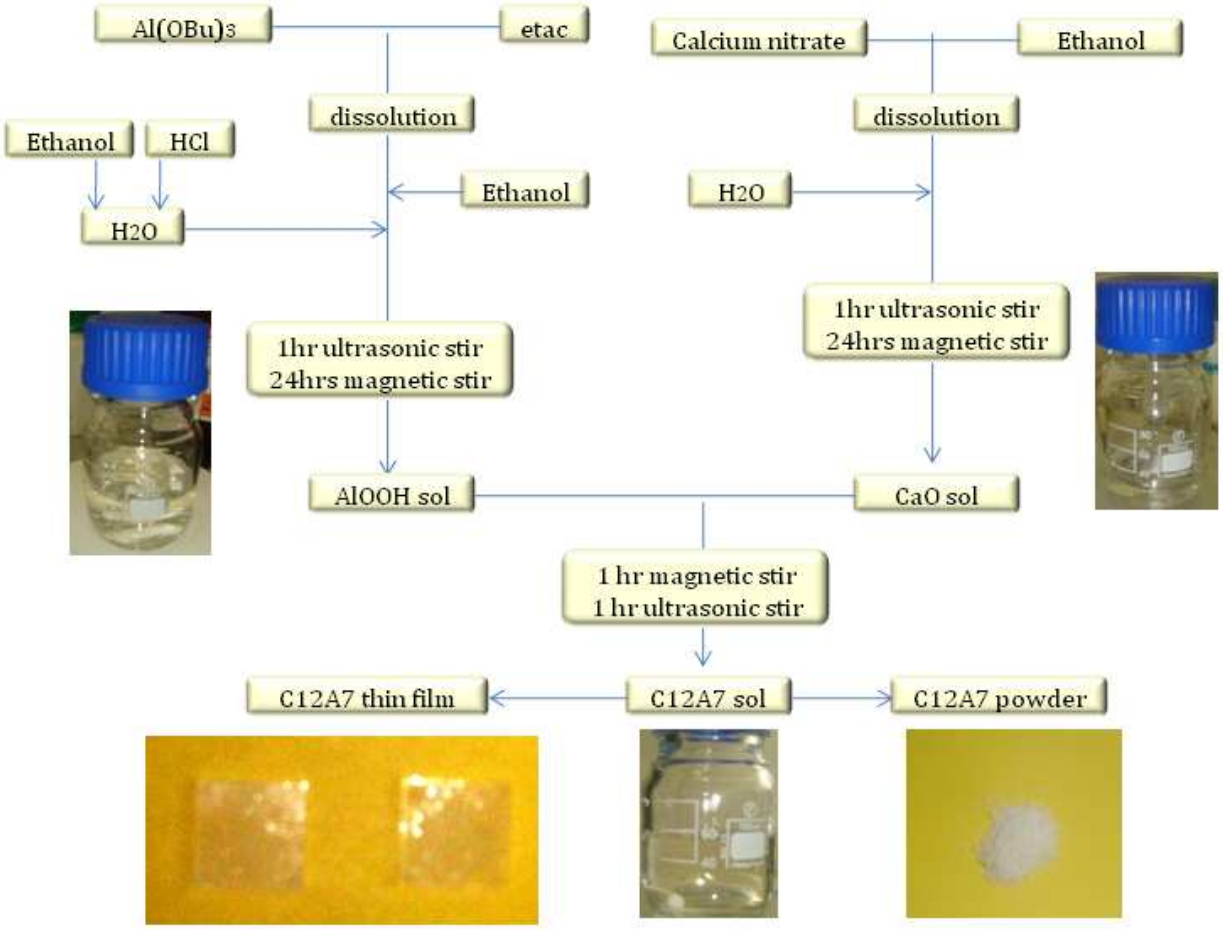

Figure 3.1: C12A7 sol-gel processing diagram, showing how the AlOOH and CaO sol formation are used as the precursors for the formation of C12A7 sol

AlOOH sol- To prepare the AlOOH sol 5.83g of aluminum sec-butoxide was mixed with 6.073ml of etac comprising the molar ratio of $Al(OBu)_3$: etac=1:1. $Al(OBu)_3$ is hydrolytically unstable and its hydrolysis leads to immediate precipitation. However modifying $Al(OBu)_3$ using etac mediates the hydrolysis of Al^{3+} ions, through

substitution of monodentate butoxy ligands of $Al(OBu)_3$ with etac groups. Etac groups will be bonded to Al atoms in enolic form [62-65], whose nature will be discussed in chapter 4.

The mixture was magnetically stirred for 30 minutes at room temperature followed by 1 hour of ultrasonic mixing to ensure the complete substitution of butoxy ligands with etac groups. Ultrasonic mixing is believed to facilitate particle break down, providing more surface area for any chemical reaction or physical dissolution. The new precursor was diluted with 18.95ml of ethanol ($Al(OBu)_3$: ethanol =1:4) prior to hydrolysis.

In the final step hydrolysis is initiated by addition of distilled water diluted with ethanol to avoid precipitation. For this purpose 3.5 ml of distilled water was diluted with 11.48 gr of ethanol (H2O: Ethanol = 1:4), followed by addition of 2ml HCl. The molar ratios were regulated at $Al(OBu)_3$:H2O: HCl = 1: 3: 0.075. HCl is used to regulate the pH of the sol [66], [67]. This will help the Isoelectric point of the sol within the allowed region to avoid particle accumulation [68-70]. The hydrolysis was performed under vigorous stirring using ultrasonic bath, followed by gentle stirring at room temperature for 24 hours using the magnetic stirrer. The final product is a clear, transparent solution of AlOOH particles in ethanol.

CaO sol- To prepare the CaO sol 5g of $Ca(NO_3)_2 . 4H_2O$ was dissolved in 6.85ml of ethanol ($Ca(NO_3)_2 . 4H_2O$: ethanol = 2 : 5) and stirred for 1 hour. Additional distilled water (3.65 ml) was added to the solution ($Ca(NO_3)_2 . 4H_2O$: H_2O = 3:4) to initiate

partial hydrolysis. The dispersion of calcium nitrate in the solvent was facilitated using ultrasonic bath followed by 24 hours of magnetic stirring. The solution formed required no further acid addition since HNO_3 was formed inside the solution.

In the final step of the sol-gel process AlOOH and CaO sols were mixed allowing the formation of homogenous C12A7 amorphous solution. At this stage the two sols were mixed magnetically for 1 hour which would lead to the formation of transparent solution. As illustrated in figure 3.2 after leaving the solution for 10 minutes precipitation is initiated accompanied by loss of transparency in the sol. This phenomena shows that magnetic stirring is not solely sufficient for the reaction between the two sols to occur. However, further ultrasonic stirring of the sol results in the formation of stable transparent solution. The ultrasonic mixing is performed for 1 hour to ensure completion of any reaction.

Figure 3.2 shows the condition of the sol after each of these stirring steps, confirming that the final sol prepared is stabilized with no sign of precipitation.

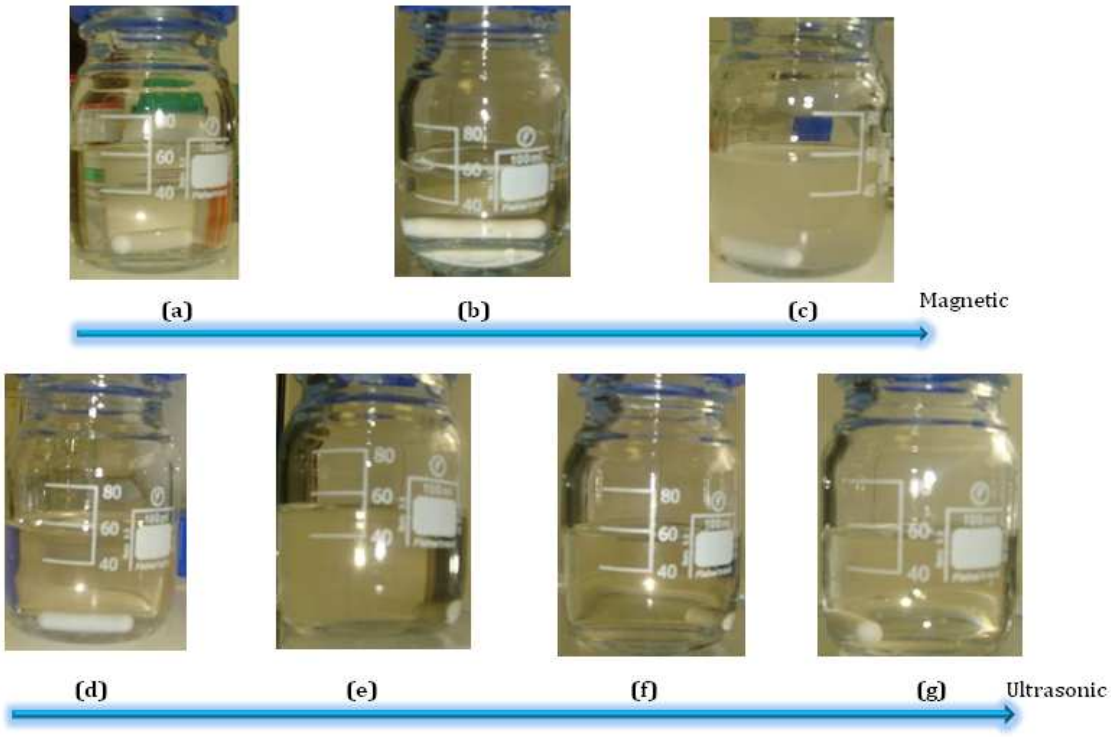

Figure 3.2: Mixing steps of C12A7 sol; (a) just mixed sol with no stirring, (b) after 1 hour magnetic stirring, (c) 10 minutes after left with no stirring, (d) 15 minutes after ultrasonic stirring, (e) 30 minutes after ultrasonic stirring, (f) 45 minutes after ultrasonic stirring, (g) 1 hour after ultrasonic stirring

C12A7 single powders were formed by dispersing the amorphous sol onto a petri dish at room temperature, allowing the solvents to evaporate. The product is a white powder as shown in figure 3.1. The as-prepared sample is exposed to heat treatment for the crystallization and further preparation procedures required for chemical, elemental and thermal characterization.

For the final device application, thin films are of much interest. Consequently, we have attempted to prepare uniform, crack-free and transparent thin films of C12A7 onto an appropriate substrate. As stated in chapter 2 there has been a comprehensive study on the type of substrate that is suitable for C12A7 film deposition. The heat treatment of C12A7 involves exposing the sample at temperatures as high as 1100˚C; therefore it requires a substrate that is stable at this temperature. Previous studies have confirmed that MgO single crystal with the <100> orientation shows no reaction between the substrate and the deposited film after high temperature heat treatment and can be used as the most stable substrate for C12A7 film formation [43].

3.1.2 Substrate Cleaning

The structure and properties of thin films will be affected by the quality of the substrate used. A rough and contaminated surface will affect the homogeneity and uniformity of the film deposited. Any contamination will increase the possibility of crack formation and will significantly affect the film quality. A clean surface will also improve the adherence of the film. In this work MgO single crystal with <100> orientation is used as suggested by previous researchers as the appropriate substrate. The cleaning procedure carried on in the current project involves 1 hour ultrasonic bath of the substrate in ethanol followed by 10 minutes soaking in HCl for

suitable etching of the substrate surface. Finally the substrate is left in isopropanol for 1 hour and dried before deposition.

3.1.3 Film Deposition

The deposition was performed through spin coating of amorphous C12A7 solution on the clean MgO single crystal. For the deposition process, 1mL of the prepared C12A7 solution was dispersed onto the substrate through a two step deposition process. In the first stage, the solution was dispersed at a speed of 2500 r.p.m, followed by 8500 r.p.m spinning for the complete evaporation of the solvent. This two step deposition ensures the uniform dispersion of the sol throughout the substrate. After spin coating the films contain residual ethanol and water. The C12A7 films were therefore left in a moisture free atmosphere desiccator at room temperature for 24 hours prior to heat treatment. A detailed discussion about the spin coating procedure is presented in chapter 5.

For the annealing and sintering process a Lenton furnace was used, which has a temperature range of 27-1600°C. A variety of annealing temperatures up to 1200°C have been investigated in this study to evaluate the crystallisation temperature for C12A7 thin films. The duration of annealing was 3 hours for all heat treatments.

3.1.4 Safety Considerations

The chemicals used for the solution preparation can be dangerous if they are in direct contact with the skin or if they are inhaled. Therefore all the solution preparation procedure was conducted under a fume cupboard and appropriate protective clothing such as gloves, lab coat, mask and glasses was worn.

3.2 Characterisation Procedures

3.2.1 Fourier Transform Infrared Spectroscopy (FTIR)

When the sample is illuminated through a light source, the photons interact with the system resulting in absorption or scattering of the light radiated. These photons may also pass through the sample without interaction [71], [72]. The process of absorption or scattering of light is used in a wide range of spectroscopic measurement techniques such as acoustic, X-Ray absorption, Nuclear Magnetic Resonance (NMR), Raman Scattering, Infrared (IR) absorption and vacuum Ultraviolet (UV) spectroscopy that operate in wide range of radiation wavelengths as illustrated in figure 3.3 [71].

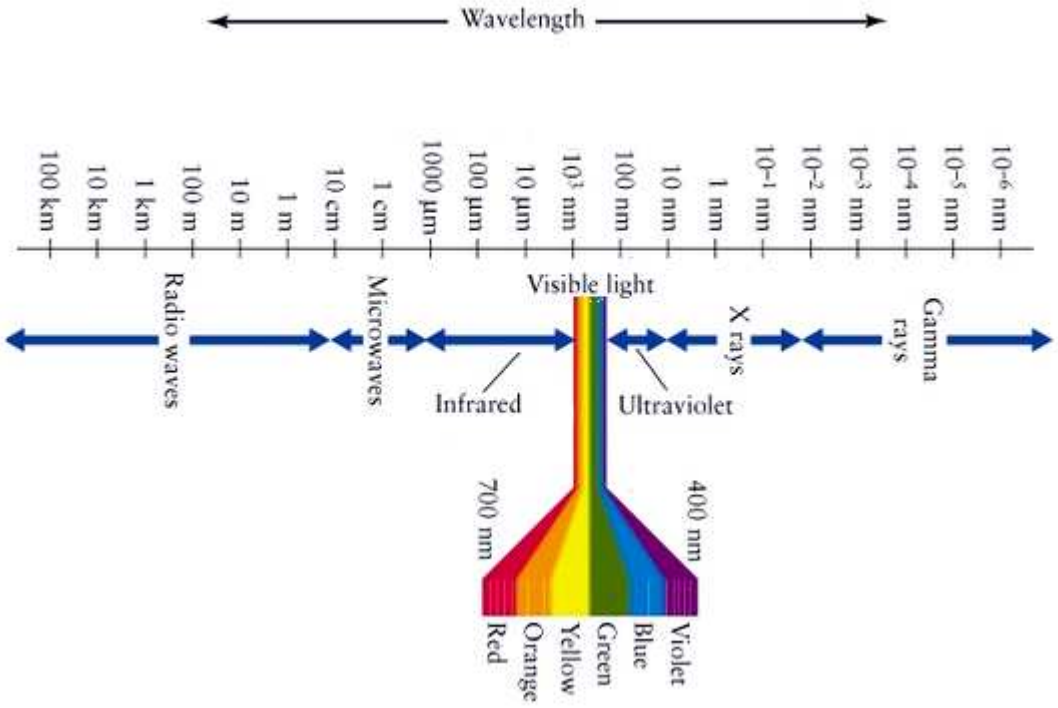

Figure 3.3: Electromagnetic radiation spectrum showing an approximate scale of the most common wavelengths [71]

In spectroscopy since the interaction of the beam with states of molecules is studied, characterizing the radiation by its energy (E) or frequency (ν) is preferred. The relationships between these scales are given below:

$$\lambda = \frac{c}{v} \tag{3.1}$$

$$v = \frac{E}{h} \tag{3.2}$$

where $c=3\times10^{17}$ (nm/S) is the speed of light and $h= 6.62\times 10^{-34}$ (m^2 kg/S) is Planck's constant. Equations (3.1) and (3.2) show the reciprocal relation between that energy and wavelength of light [71], [73], [74].

If the energy of an incident photon corresponds to the energy bandgap of the system, the photon can be absorbed promoting the molecule to a higher energy level. Calculating the loss of energy of the incident light is the principle of absorption spectroscopic measurements. Infrared spectroscopy lies in the same category where after passing through the "monochromator", Infrared (IR) radiation is guided through the sample. Absorption occurs where the frequency of the IR beam matches that of the vibrational or rotational mode of the molecule. Detecting the loss of this frequency from the beam provides a characteristic pattern of the matter. Fourier Transform Infrared Spectroscopy (FTIR) follows similar route. In this technique instead of varying the frequency of the incident light using the monochromator, the waves are interfered using an "interferometer". Fourier Transform Spectrometer is then used to analyse the corresponding Infrared spectrum. Figure 3.4 indicates a typical FTIR spectroscopy procedure [71].

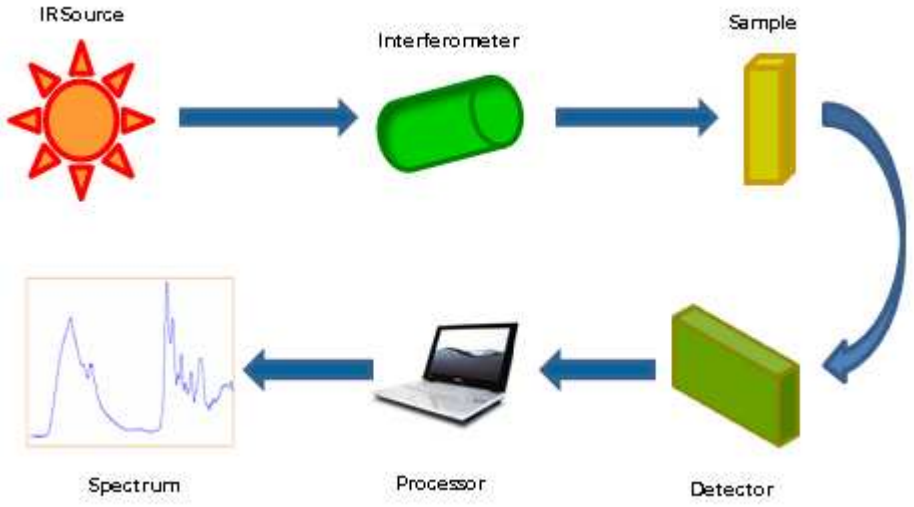

Figure 3.4: FTIR spectroscopy stages using Fourier Transform Spectrometer

In the current project FTIR spectroscopic measurements were carried out using a Nicolet 8600 FTIR spectrometer (Thermo Electron Corporation, UK) in conjunction with an MTEC Photoacoustic Spectrum (PAS) cell. Spectra were obtained in the mid infrared region (4000-400 cm^{-1}) at 4 cm^{-1} resolution and averaging of 256 scans and two different loadings; one with amorphous C12A7 dried gel and the other with crystallised C12A7 powder. The crystallised C12A7 powders were obtained upon a heat treatment of the amorphous dried gel at 1100°C for 3 hours. The heating and cooling rate were adjusted to 10°C per minute.

3.2.2 Raman Spectroscopy

As discussed in previous section due to interaction of photons with the system absorption or scattering of the radiated light occurs both of which can be utilized in spectroscopic measurements. Raman Spectroscopy is regarded as the most useful scattering technique for molecular identification.

In this scattering method, the photons polarize the cloud of electrons round the nuclei to form an unstable state known as “virtual state”. Such distortion causes rapid scattering of photons with very small changes in frequency due to light weight of electron clouds. This is the dominant scattering known as “elastic scattering or “Rayleigh scattering”. If nuclear motion is involved in the scattering there will be an energy transfer between the photon and the molecule resulting in a difference between the energy of the incident and scattered photon. This is regarded as “inelastic scattering” and is the basis of Raman Spectroscopy. Modern Raman spectrometers use very high power lasers and microscope increasing the efficiency of this technique. The disadvantage of using such high power lasers are sample degradation and fluorescence [71], [75].

As stated above Raman spectroscopy relies on inelastic scattering (Raman scattering) of laser light producing a “fingerprint” of the system, characteristic of vibrational and rotational modes of molecule. Figure 3.5 shows the principle of a molecular vibration [76].

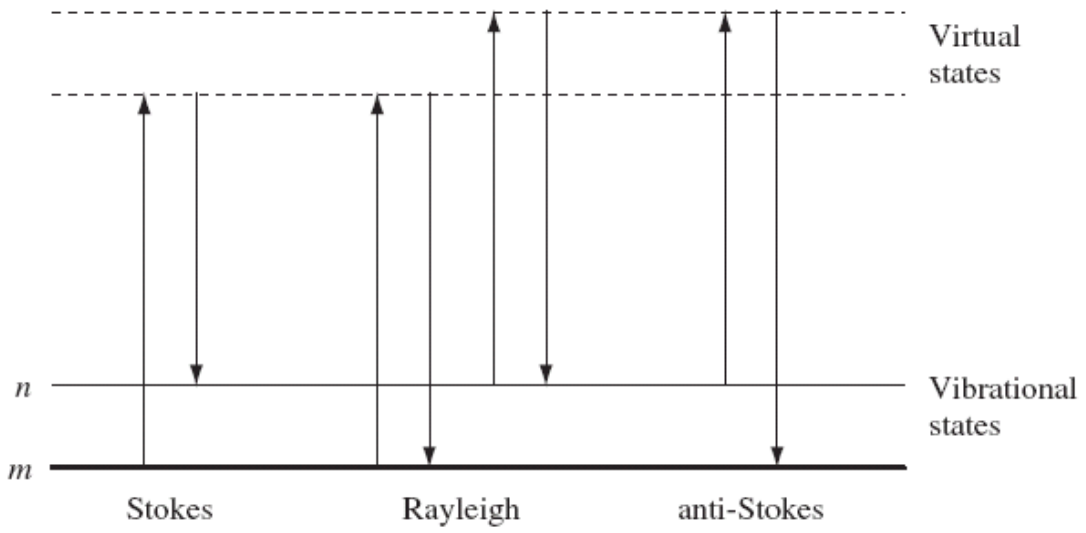

Figure 3.5: Diagram of the Rayleigh and Raman scattering processes [71]

As a result of the interaction between photons and the molecule both elastic and inelastic scattering occur. Since elastic or (Rayleigh) scattering does not require any change in the energy state most of the photons are elastically scattered increasing the intensity of this process. Inelastic or "Raman" scattering is categorized into "Stokes" and "anti-Stokes" scattering. As illustrated in figure 3.5, during Stokes scattering atoms are excited from state *m* to state *n* absorbing energy. Scattering from the excited *n* states to ground states *m* is regarded as "anti-Stokes" scattering during which energy is transferred to the photon. At room temperature most molecules are expected to be in ground state increasing the possibility of "Stoke" scattering. Usually, Raman spectroscopy is performed on the low-energy side to give Stokes scattering [75].

Figure 3.6 shows different stages involves in Raman Spectroscopy. As can be seen, laser light is radiated to the sample. This light is filtered prior to illumination to block any undesired light being scattered. The light being collected from the sample requires a second filtration to block the elastic scattered light at the laser wavelength. This filtered light is then guided through the detector where the corresponding spectrum is obtained.

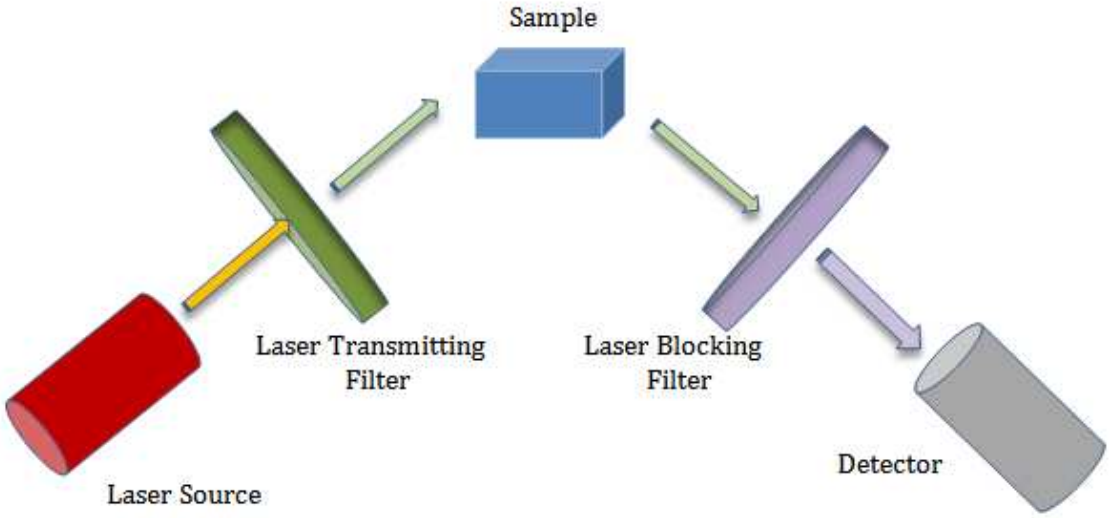

Figure 3.6: Raman Spectroscopy stages using laser transmitting and blocking filters

As a complementary to FTIR spectroscopy Raman Spectroscopy was carried out using a Nicolet Almega XR dispersive Raman spectrophotometer (Thermo Fisher Scientific, Madison Wisconsin, USA), equipped with 532nm and 785nm lasers with two different loadings; one with amorphous C12A7 dried gel and the other with crystallised C12A7 powder. All the spectra were collected in the range 4000-400 cm-

[1] using a 10X objective and over an average of 256 scans, 1 second exposure time at low resolution.

3.2.3 Simultaneous Thermal Analysis (STA)

Simultaneous Thermal Analysis (STA) is a combination of Differential Scanning Calorimetric (DSC) and Thermogravimetric Analyzer (TGA). This technique is used to follow the course of chemical reactions, thermal decompositions or phase changes by measuring both enthalpy changes (DSC) and weight gain or weight loss (TGA) as a function of temperature or time. In this analysis the sample will undergo a precisely controlled thermal cycle along with an inert reference with known thermal response. Any changes in specific heat, exothermic/endothermic reaction, or phase change result in temperature difference between the sample and the reference which in turn analyses the thermal behavior of the sample by showing the heat flow values as a function of temperature. Simultaneously, any changes in mass of the sample during heating cycle can be measured as a function of temperature.

STA was performed using STA 1500 equipment as shown in figure 3.7. These studies were necessary in order to identify the critical temperature for phase transformation and crystallisation of C12A7 and also the evaporation temperatures for any water, solvents or organic residue. For the STA analysis the dried C12A7 gel was placed in a small crucible and fitted inside the instrument and exposed to heat treatment at various rates over a programmed temperature range (30-1200°C).

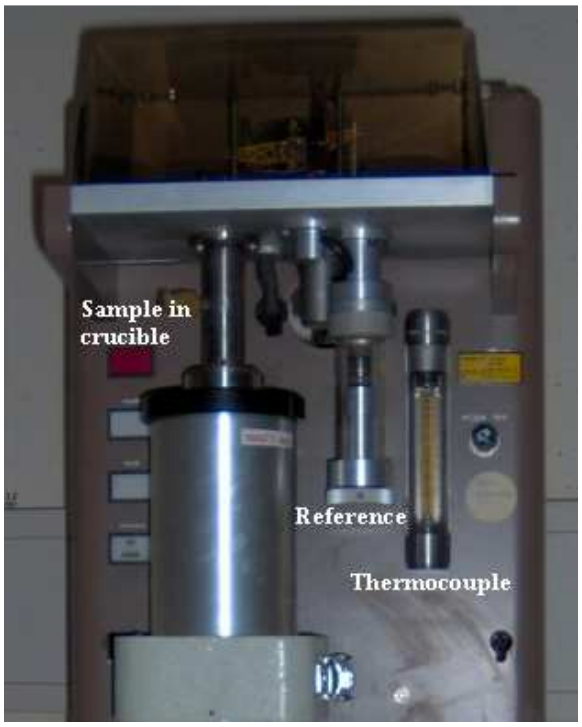

Figure 3.7: STA 1500 instrument with two crucibles for sample and reference

3.2.4 X-Ray Diffraction

X-Ray Diffraction (XRD) is a non-destructive analytical method based on the elastic scattering of X-ray radiation from sample. This technique measures the intensity of the scattered X-ray beam as a function of incident angle revealing information about the crystallographic structure and physical properties of materials. As mentioned in previous section "Rayleigh" or "elastic" scattering of photons occurs when the electron clouds round the nuclei are involved in the scattering process. Crystals are defined as regular arrays of atoms and if X-ray waves

interact with these ordered atoms they will produce a regular array of waves. Due to destructive interference the scattered waves cancel one another in many directions. Only a few specific directions are favorable for constructive interference of waves which can be determined using Bragg's Law:

$$2dsin\theta = n\lambda \tag{3.3}$$

where d is the spacing between scattering planes, θ is the incident angle, n is any integer, and λ is the wavelength of the X-Ray beam. Figure 3.8 shows the constructive interference of waves following Bragg's Law [77], [78].

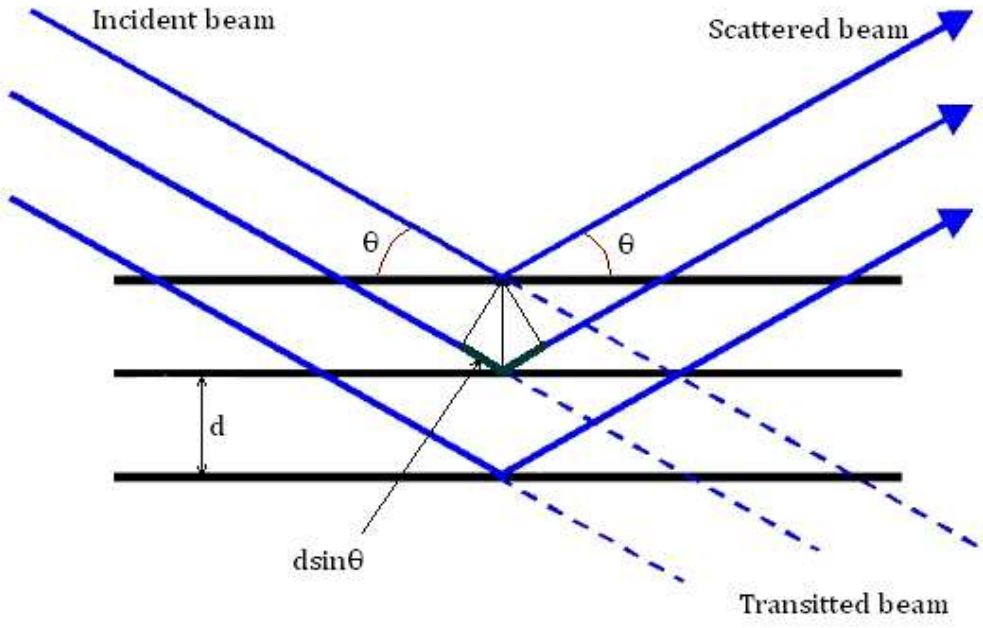

Figure 3.8: Bragg's Law [77]

The sample under XRD examination can be in the form of powders, bulk or thin film in both hot and cold states. Powders will be pressed into a sample holder to obtain a smooth flat surface prior to measurements. The mechanical assembly of the sample holder, detector and X-Ray tube is referred to as "Goniometer". Figure 3.9 shows the goniometer in θ: θ and θ: 2 θ positions. The spacing between the sample and the X-ray spot is the same as between the sample and the detector.

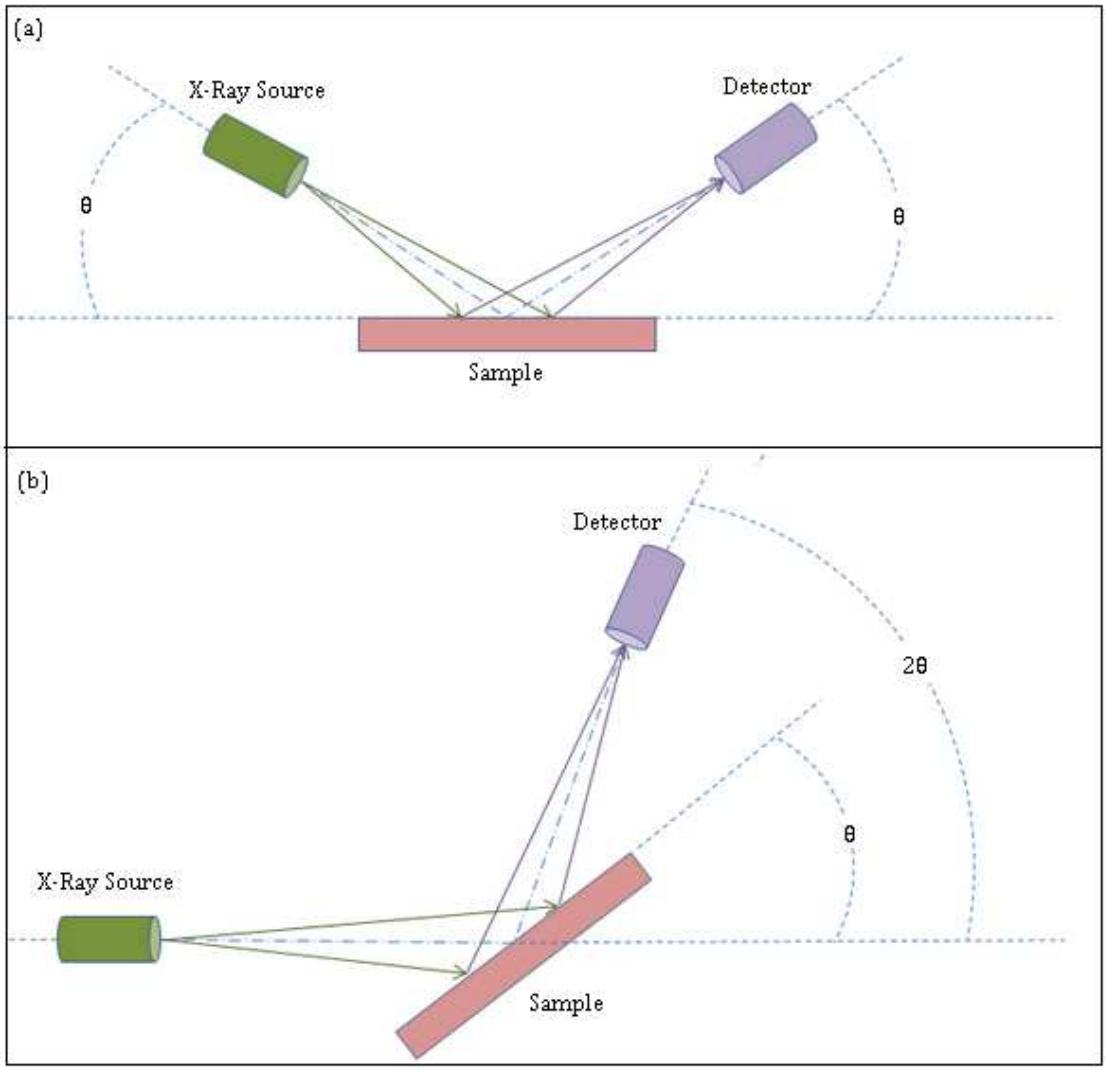

Figure 3.9: X-Ray Diffraction goniometer in (a) θ: θ and (b) θ: 2θ set up

As illustrated for the θ: θ setup, the sample is stationary and the X-ray tube and the detector move simultaneously over the angular range of θ. In θ: 2θ set up, the X-ray tube is stationary, the sample moves over the angular range of θ while the detector moves by the angle 2θ. For the analysis of thin films it is some times difficult to use θ: θ or θ: 2θ assembly due to small diffracting volumes. The diffracted intensity will be very low compared to the substrate and background making it difficult to identify the phases present in the thin film. "Grazing Angle" is the most common arrangement used in the analysis of thin films. Figure 3.10 illustrates the grazing angle set up used for thin films.

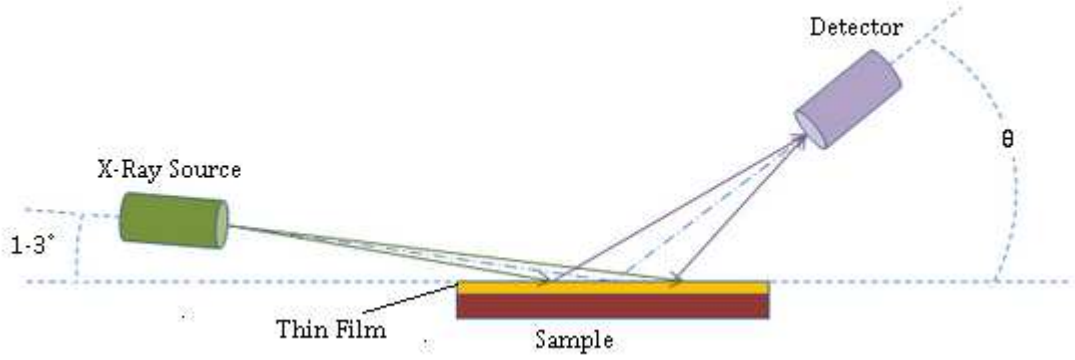

Figure 3.10: Grazing Angle set up for thin film X-Ray Diffraction

In the grazing angle set up only the detector rotates through the angular range of θ while the sample and the X-Ray tube are stationary. The incident beams makes a very small angle (1-3°) with the thin film surface increasing the path length of the

beam through the film. This will reduce the diffracted intensity from the substrate while the overall diffraction from the film is increased [78].

In the current investigation two sets of diffraction spectroscopy were performed on thin films and powders of C12A7. A series of XRD spectra were obtained through grazing angle X-Ray spectroscopy performed on thin films of C12A7 on MgO single crystal being subjected to thermal treatments at 700˚C-1200˚. . For this purpose a Siemens D5000 X-Ray Diffractometer is used in which the incident angle was set to 2˚.

To determine any crystalline phase present at various heat treatment temperature, a High Temperature X-Ray Diffraction (HTXRD) study is carried on. X-Ray diffraction was performed in θ:θ goniometer assembly at variable temperature using a D5000 X-Ray diffractometer equipped with an Anton Paar HTK-16 vacuum furnace using CuK α radiation (λ=1.54A°). An Anton Parr TCU 2000 temperature control unit provides direct temperature control. The detector is a Panalytical X'Celerator solid state detector which scans continuously. Samples were placed on the pre-stressed Platinum strip. Experiments were performed from room temperature up to 1200°C, in the 5°-65° 2θ domain.

3.2.4 Energy Dispersive X-Ray Spectroscopy (EDX)

Energy dispersive X-ray spectroscopy (EDX) is another spectroscopic technique which relies on the analysis of the light emitted from the sample as a result of electromagnetic radiation. Using this method it is possible to reveal information about the elemental and chemical characteristics of the matter. Each element in the periodic table has a unique atomic structure and will emit x-rays that are characteristic of that element allowing the identification of the atomic structure.

As stated earlier, the atoms are mostly in the ground state when not excited and the electrons round the nuclei are in discrete energy levels. As illustrated in figure 3.11, when the sample is illuminated by electromagnetic radiation the electron will be excited to a higher energy creating a hole. To fill this hole, an electron from higher energy level will release energy to move to the lower unoccupied energy level. The released energy will be emitted from the matter in the form of X-Ray which can be measured using an energy dispersive spectrometer. The measured X-Ray energy is the difference between the energy levels within the atomic structure and is the unique for each element. EDX spectroscopy provides the elemental composition of the sample through this analysis with the precise amount of each element present [79].

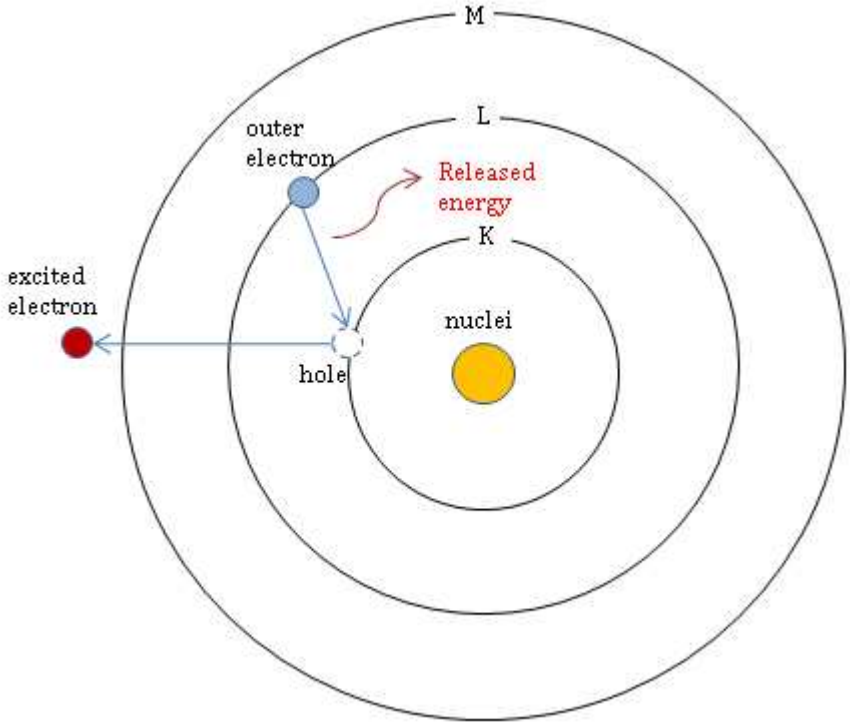

Figure 3.11: Atomic structure and the principle of EDX [79]

To conduct such detailed chemical and elemental analysis on C12A7 thin film heat treated at 1100˚C for 3 hours, JEOL Scanning Electron Microscope with a Link pentafet-ST windowless energy dispersive X-ray detector was used.

3.2.5 UV-Visible Spectroscopy

UV/Vis spectroscopy is conducted using photons in the visible and adjacent (near ultraviolet (UV) and near infrared (NIR)) ranges. The energy of the incident photon can promote the atom from the ground state to the excited state. Calculating the loss

of energy of the incident light is the principle of absorption spectroscopic measurements. Such aanalysis allows the determination of a variety of fundamental material parameters such as optical energy bands and the nature of the transition between different energy levels.

UV/Vis spectrometer includes a light source, sample holder, monochromator and a detector. Photodiodes are used in conjunction with monochromators to filter the light before reaching to the detector.

During the course of spectroscopic measurements the intensity of the light before passing through the sample (I_o) is compared to the intensity of the transmitted light (I). The absorbance (A) of the sample is expressed as a function of the two measured intensities [71]:

$$A = -\log\left(\frac{I}{I_o}\right) \tag{3.4}$$

To study the optical properties, the optical absorption spectra of the films heat treated at various annealing temperatures were obtained using a Perkin Elmer Lambda 950 spectrometer. The spectroscopy was performed in the wavelength range of 200-1000nm. In order to avoid the effects of substrate absorption the optical absorption of an uncoated MgO <100> single crystal was measured and deducted from that of the coated samples. The data was converted to absorbance vs. photon energy when required.

Chapter 4

The Chemistry of Sol-gel Processing of C12A7

C12A7 films and dried gel were successfully fabricated using the sol-gel method. Precise control over the chemical composition, thickness and size of the final sample as well as the possibility to coat large and complex shaped substrates, can be counted as the main reasons for choosing this method for the fabrication of C12A7. In this chapter the results of the FTIR and Raman spectroscopy is presented followed by a comprehensive chemical analysis on the final dried gel before and after thermal treatment. The chemical analysis is complemented by a brief introduction to the sol-gel process and the main parameters involved.

4.1 Results of Chemical Analysis

The chemistry of sol-gel processing of C12A7 can be studied using FTIR and Raman spectroscopy. These analytical tools identify the chemical functionalities and structural changes during the process. FTIR spectra of amorphous C12A7 dried gel and crystallised C12A7 powders are presented in figure 4.1 and 4.2 respectively.

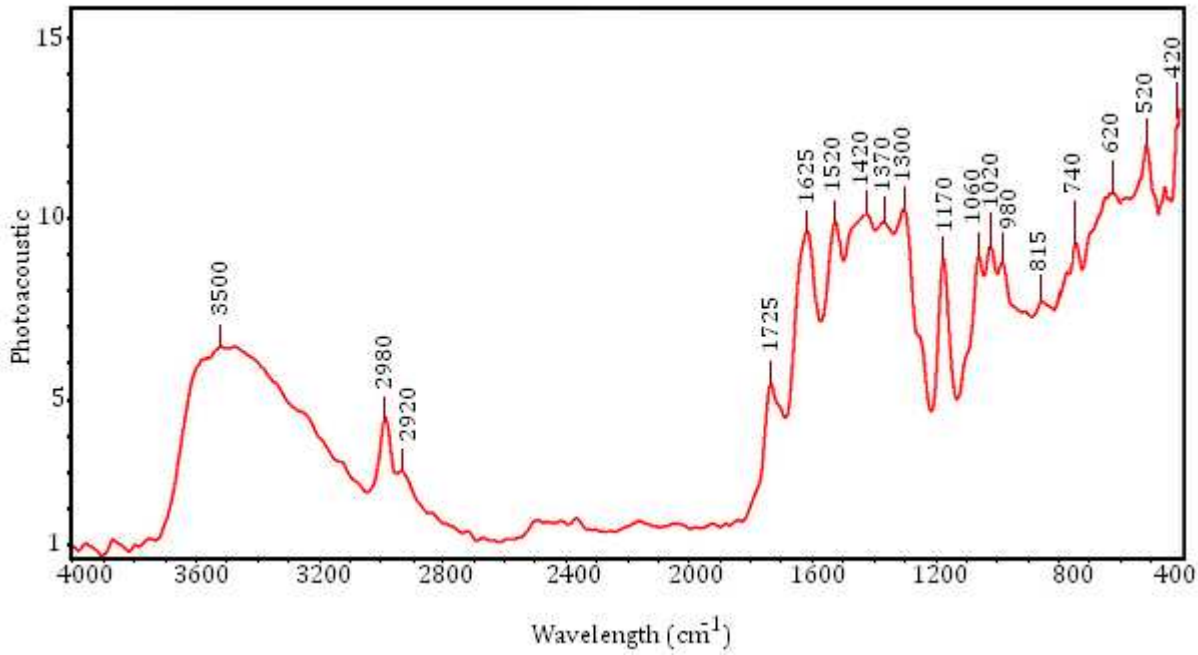

Figure 4.1: FTIR spectrum of amorphous C12A7 dried gel

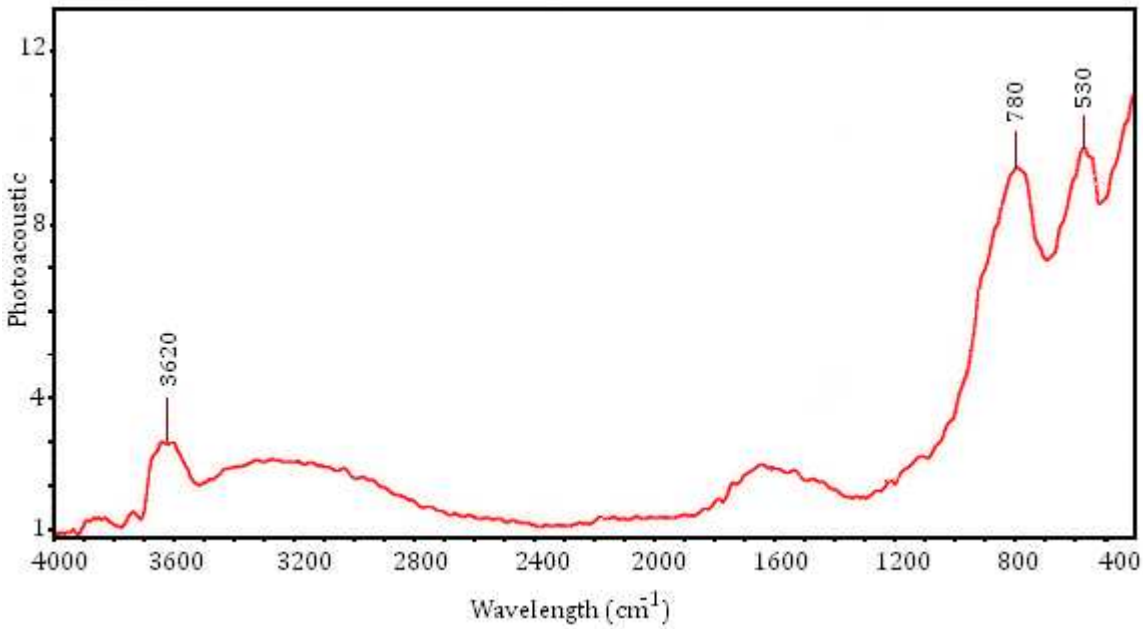

Figure 4.2: FTIR spectrum of crystallized C12A7 powder

Raman spectroscopy is performed using two different lasers of 532nm and 78nm to ensure every single vibration is detected. Figures 4.3 and 4.4 illustrated the spectra of amorphous C12A7 dried gel and crystallized C12A7 powders collected using 532nm laser. Figures 4.5 and 4.6 demonstrate the spectra of amorphous C12A7 dried gel and crystallised C12A7 powders collected using 785nm laser.

The peak assignments of amorphous and crystalline C12A7 phases for both FTIR and Raman spectroscopy are listed in tables 4.1 and 4.2.

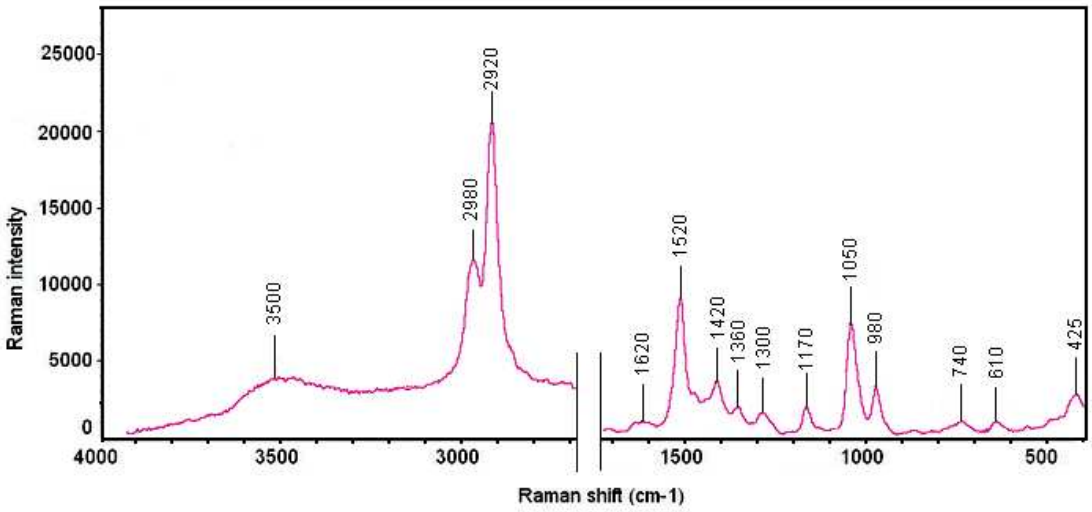

Figure 4.3: Raman spectrum of amorphous C12A7 dried gel with 532nm laser

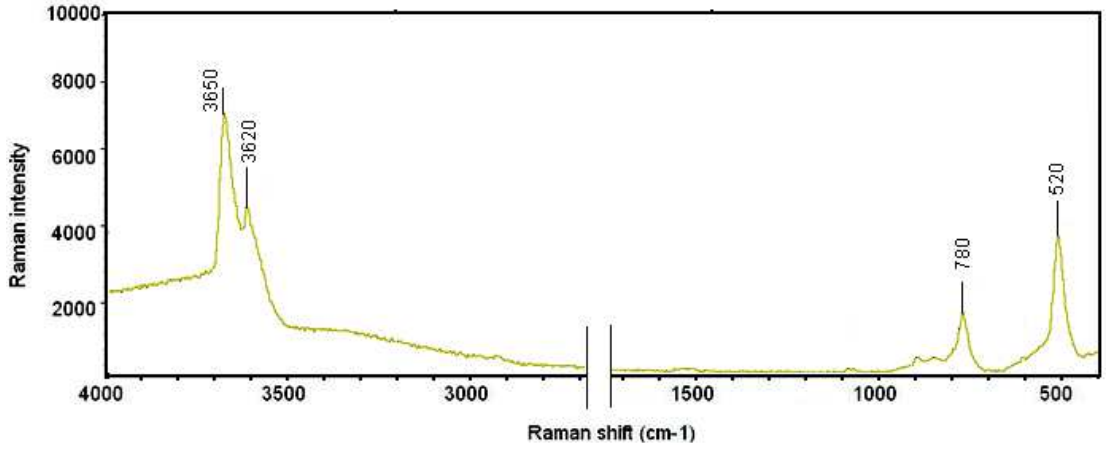

Figure 4.4: Raman spectrum of crystallized C12A7 powder with 532nm laser

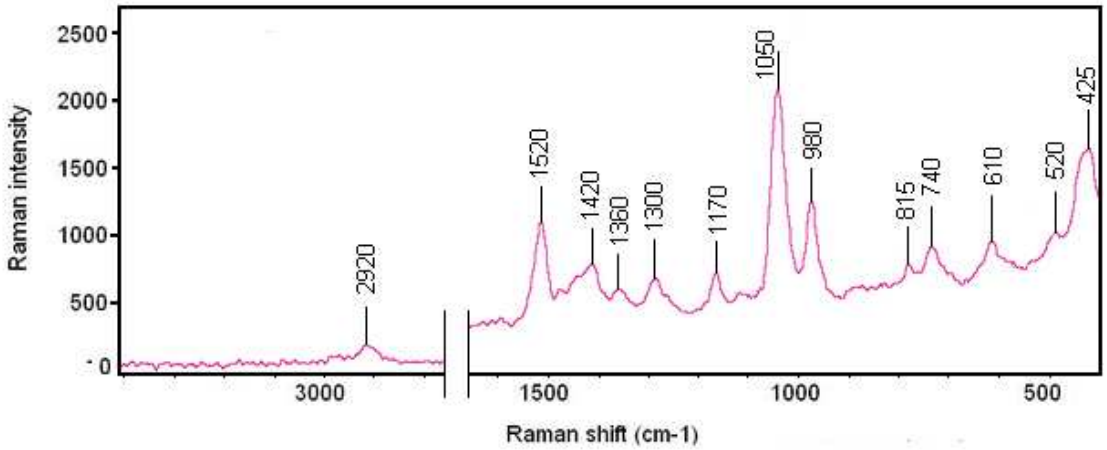

Figure 4.5: Raman spectrum of amorphous C12A7 dried gel with 785nm laser

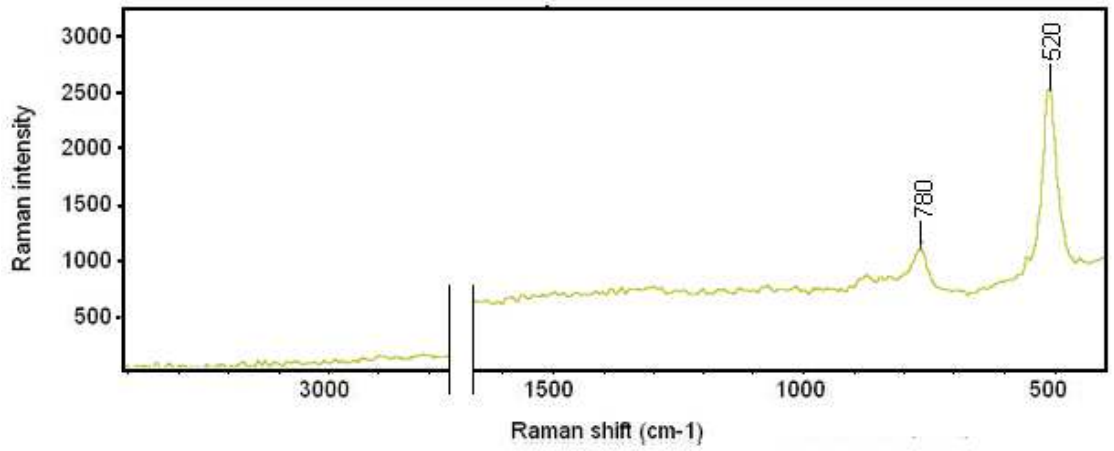

Figure 4.6: Raman spectrum of crystallized C12A7 powder with 785nm laser

Table4.1: FTIR and Raman assignments of amorphous C12A7

Compound	FTIR	Raman I	Raman II	Bonding	References
$Ca(NO_3)_2.4H_2O$	740	740	740	Ca-O-No_2(C_{2v} symmetry)	[80], [81]
	815	-	815	Ca-O-No_2(C_{2v} symmetry)	[80], [81]
	1060	1050	1050	Ca-O-No_2(C_{2v} symmetry)	[80], [81]
	1370	1360	1360	Ca-O-No_2(C_{2v} symmetry)	[80], [81]
	3500	3500	-	Stretching vibration of OH^-	[81], [82]
Boehmite (AlOOH)	420	425	425	Al-O vibration	[83], [84]
	520	-	520	Al-O vibration	[83], [84]
	620	610	610	Al-O vibration	[83], [84]
	740	740	740	Al-O vibration	[83], [84]
	980	980	980	Bending vibration of OH^-	[82], [84]
	1020	-	-	Bending vibration of OH^-	[82], [84]
	1060	1050	1050	Bending vibration of OH^-	[82], [84]
	3500	3500	-	Stretching vibration of OH^-	[82], [84]
Ethyl acetoacetate	1170	1170	1170	Stretching vibration of C-H	[63], [81]
	1300	1300	1300	Bending vibration of C-C	[63], [81]
	1370	1360	1360	Stretching vibration of CH_3	[63], [81]
	1420	1420	1420	Stretching vibration of CH_3	[63], [81]
	1520	1520	1520	Bending vibration of C=C	[63], [81]
	1615	1620	-	Stretching vibration of C-O for enolic form	[63]
	1735	-	-	Stretching vibration of C-O for ketonic form	[63]
	2920	2920	2920	vibration of CH_2	[63], [81]
	2980	2980	-	vibration of CH_2	[63], [81]
Butoxy ligands	1060	1050	1050	Stretching vibration of C-O	[81]
	1370	1360	1360	Stretching vibration of CH_3	[81]
	1420	1420	1420	Stretching vibration of CH_3	[81]
	2920	2920	2920	vibration of CH_2	[81]
	2980	2980	-	vibration of CH_2	[81]

Table4.2: FTIR and Raman assignments of crystalline C12A7

Compound	FTIR	Raman I	Raman II	Bonding	Reference
C12A7	530	520	520	Vibration of C12A7 lattice framework	[84]
	790	780	780	Vibration of O^{2-} ions	[84]
	3620	3620	-	Bending vibration of OH^-	[81], [82]
	3650	3660	-	Bending vibration of OH^-	[81], [82]

4.2 Sol-gel technology

Sol-Gel process involves the transition of a system from a sol (liquid) into a gel (solid). A *sol* is defined as a colloidal suspension of solid particles in which the dispersed phase is so small (~1-1000nm) that gravitational forces are negligible and interactions are dominated by Van der Waals attractions and surface charges. A *gel* is a substance that contains a continuous solid network enclosing the liquid phase. Gels are established when the attractive dispersion forces (Van der Waals forces) cause the particles to stick together to form a network [85-87].

Using sol-gel it is possible to obtain solutions of high homogeneity and controlled concentration without using expensive equipment. Sol-gel technology has other certain attractive features such as the ease of forming films of controllable thickness,

the protective environment formed around the particles which can prevent crystal growth and aggregation, the possibility of using high purity starting materials and coating films on substrates with complex shapes. Another merit of Sol-Gel chemistry is the possibility to impregnate or "dope" many chemical species into the pores of the formed gel by adding them to the sol [88], [89].

In the sol-gel process, the starting compounds known as "precursors" will be used for the preparation of sol. These precursor compounds are highly soluble chemical substances which are easily converted into chemically reactive forms of hydrated oxides on hydrolysis. Two main groups of precursor compounds are metal salts (inorganic salts) or metal alkoxides (metal organic compounds). In the present investigation the binary oxide compound is formed through using both types of precursors. Sol-gel science and technology involves the introduction of a versatile range of chemical compounds, as well as various preparation routes accordingly. A complete study of the science behind sol-gel technology lies outside the scope of this project. In simple words, the process involves a two step hydrolysis and condensation reaction of the precursor with water [85], [90].

4.3 Hydrolysis and Condensation

As mentioned earlier the precursor will react with water to form the metal oxide. The hydrolysis process may be completed (so that all the OR groups will be replaced by OH groups), or stop while the metal is only partially hydrolyzed. This depends on

the amount of water and catalyst present. The condensation will be followed by the hydrolysis leading to the liberation of a small molecule such as water or alcohol while two partially hydrolysed molecules link together.

4.3.1 Solution Chemistry of C12A7

One of the main requisite of sol-gel technology is the development of appropriate precursor. Two ideal candidates for this purpose that have been extensively used are metal alkoxides and metal salts. Metal Alkoxides which are derivatives of alcohols are inexpensive and easily accessible organic compounds, meeting the criteria to be used as sol-gel precursor. The main disadvantage of metal alkoxides is their sensitivity to atmosphere moisture, making them difficult to work with. Metal salts are also extensively used as the precursor, where they are readily converted to metal oxides by thermal decomposition.

The present work involves the production of both CaO and Al_2O_3 metal oxides in appropriate nominal concentration leading to the formation of C12A7. This route produces crystalline C12A7 nanoparticles loaded with O^{2-} /OH^- ions through hydrolysis-condensation process. For this purpose CaO has been prepared using metal salt, while Al_2O_3 is prepared using metal alkoxides.

Solution Chemistry for $Al(OBu)_3$ Precursor:

For the preparation of Al2O3 using metal alkoxide, the experiments were carried out using a $Al(OBu)_3$/ethyl acetoacetate solution with a molar concentration of 1:1 diluted with ethanol. As stated earlier, metal alkoxides are sensitive to atmosphere moisture and water. $Al(OBu)_3$ as the metal alkoxide being used in this work is following the same route, being hydrolytically unstable, with immediate precipitation when hydrolysed. However modifying $Al(OBu)_3$ using ethyl acetoacetate(etac) mediates the hydrolysis of Al^{3+} ions, through substitution of monodentate butoxy ligands of $Al(OBu)_3$ with etac groups. Etac groups will be bonded to Al atoms in enolic form [63].

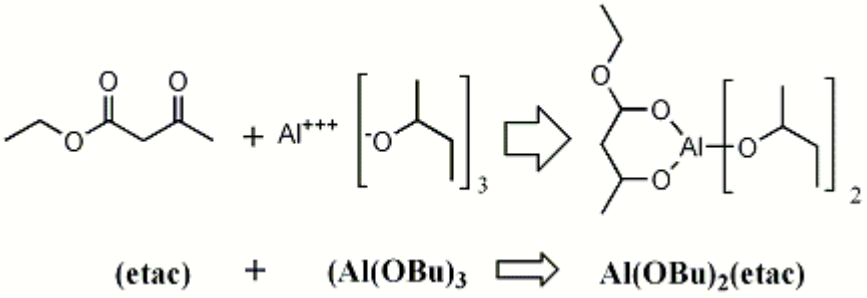

Hydrolysis is carried out by addition of distilled water with a molar ratio of $Al(OBu)_3$: H_2O=1:3. During hydrolysis of the modified $Al(OBu)_2$(etac) compound, etac groups will be separated from the compound in both enolic and ketonic forms. Following the separation of butoxy ligands, AlO bonding will be exposed to OH bonding of water,

resulting in the formation of boehmite (AlOOH). The reaction at this water content may be derived as:

$$Al(OC_4H_9)_2(etac) + 3H_2O \rightarrow AlOOH(H_2O) + etac + 2C_4H_9OH \qquad (4.1)$$

The acid concentration used in the synthesis of AlOOH particles was chosen at molar ratio of Al_2O_3: HCl = 1 : 0.15, thereby reducing the pH of the solution from 10.4 to 8, well below the isoelectric point of boehmite particles. Such acid regulation will reduce the chance of agglomeration due to columbic interactions between particles [68].

Solution Chemistry for $Ca(NO_3)_2$ Precursors:

For the preparation of CaO a metal salt is used as the precursor. Dissolving $Ca(NO_3)_2.4H_2O$ as the precursor in ethanol, the calcium nitrate crystals will be dissolved, forming a homogenous dispersion of this crystalline phase in ethanol as the organic solvent. $Ca(NO_3)_2.4H_2O$ is partially hydrolyzed using distilled water with molar ratio of $Ca(NO_3)_2.4H_2O$: H_2O=3 : 4 to form the second precursor for C12A7 solution. Addition of water expels some salt ions to form HNO_3, decreasing the pH of the solution to 4 below the isoelectric point of CaO particles. Therefore the solution formed required no further acid addition.

$$3Ca(NO_3)_2 + 4H_2O \rightarrow 4CaO + 6HNO_3 \qquad (4.2)$$

The sol-gel process starts with a homogenous solution of AlOOH and $Ca(NO_3)_2$ in ethanol solvent with the concentrations meeting the nominal composition of the C12A7 compound. The monodispersed, stable solution formed undergoes a series of chemical reactions and phase transformations during hydrolysis, condensation and thermal treatment, the nature of which are not yet clear. Here, a versatile range of chemical reactions and phase transformations associated with these phenomena will be identified through a series of structural and analytical characterization techniques, which exploits each of these events.

4.4 Drying and Sintering

During drying, evaporation of organic solvents (ethanol in the present experiment) progressively facilitates the formation of amorphous phase from the solution. Continued drying of the sol and evaporation of the solvent promotes the inorganic precursors and organic additives into the desired structure.

This stage can be divided into the following steps:

1. The excess liquid will evaporate and the body shrinks.

2. The body becomes to stiff to shrink, receding the liquid into the interior.

3. The liquid becomes isolated and will evaporate within the body, leaving pores [91].

In this experiment a wide range of thermal treatment temperatures are employed in order to specifically define the appropriate temperature. Thermal treatment of the dried gel is known as “sintering”. Sintering is defined as the process of densification, eliminating pores via viscous flow and diffusion. During the sintering the structure becomes denser and the pores collapse gradually. When the temperature reaches the glass transition temperature of the material the structural relaxation will occur and increasing the temperature further will result in the viscous flow of the material [92]. Finally a dense, solid material will be formed in which higher temperatures will result in its crystallisation. Here the thermal treatment will lock in the nano-caged structure of C12A7 and develops covalent bonds of Ca-O-Al to form the framework.

4.5 Film Formation

Apart from all the advantages that mentioned earlier, one of the most technologically important aspects of the sol-gel processing is that, before the gelation occurs in the solution, the fluid sol is ideal for the fabrication of thin films by common coating techniques such as dipping, spinning, spraying, electrophoretic and thermophoretic.

The deposition method used in the current project was spin coating. As demonstrated in figure 4.7, Spin coating consists of four stages:

1. *Deposition*- The liquid is dispersed on the surface.
2. *Spin Up*- The liquid will be driven radially outward by centrifugal forces.
3. *Spin Off*- The excess liquid will flow to the perimeter and will leave as droplets.
4. *Evaporation*- The water and solvents will evaporate as the first mechanism of thinning [93].

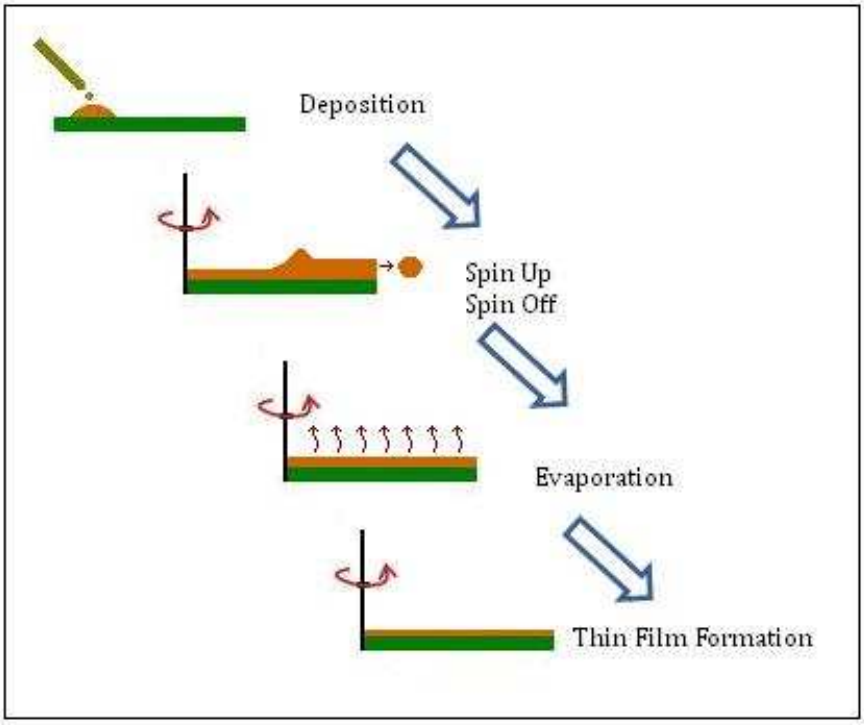

Figure 4.7: The four stages of the spin coating process are sequential in that dispersed solution outflows radially by centrifugal forces. Solvent evaporation continues throughout the process

The most noticeable advantage of spin coating is the uniformity of the film produced. As the liquid flows to the perimeter during the spin-off stage the film becomes more uniform in thickness and once uniform tends to keep its uniformity [93].

4.6 Chemical Analysis of Sol-gel Process

As discussed above sol-gel processing involves a series of chemical reactions through which the hydrolysis and condensation of the solution occurs. Investigation of the chemistry behind sol-gel synthesis is of significant importance for accurate control over reactions and phase transformations. FTIR and Raman are believed to be the most reliable characterization techniques for the analysis of chemical reactions. Here we will extend our knowledge regarding the sol-gel processing of C12A7 through FTIR and Raman analysis of the C12A7 prepared before and after heat treatment.

4.6.1 FTIR Spectroscopy

In FTIR the infra-red radiation is illuminated to the sample, where part of the beam is transmitted through the sample and the rest is absorbed. The spectrum obtained includes a series of intense, isolated and reliable absorption bands of fundamental vibrational frequencies of the molecular bondings within the sample. Apart its simplicity, speed and sensitivity, FTIR provides unique molecular fingerprint typical to each material. In fact, each material is formed as a result of specific geometry of particular atoms unique to that material. The intensity of each peak is representative of the amount of corresponding molecular bonding [71].

Conducting the FTIR spectroscopy before and after thermal treatment an extensive understanding of the chemical reactions involved in the sol-gel synthesis

of C12A7 is provided. As presented in figures 4.1 and 4.2, the FTIR spectra of C12A7 shows significant differences between two loadings of dried gel and crystalline phase.

The presence of AlOOH, $Ca(NO_3)_2$ is expected in C12A7 dried gel as the main element for the formation of final C12A7 phase. In figure 4.2 four featured bands at 740 cm^{-1}, 815 cm^{-1}, 1060 cm^{-1} and 1370 cm^{-1} are assigned to Ca-O-NO_2 (as a bivalent metallic nitrate) with C_{2v} symmetry [80], [81]. On the other hand, the presence of AlOOH is evidenced by the appearance of four absorption bands at 420 cm^{-1}, 520 cm^{-1}, 620 cm^{-1} and 740 cm^{-1}, assigned to Al-O vibrations [83], [84]. The hydroxyl groups attached to Al-0 vibrate at 3500 cm^{-1} for the stretching and at 980 cm^{-1}, 1020 cm^{-1} and 1060 cm^{-1} for the bending vibrations [81], [82], [84].

As stated earlier, the hydrolysis of $Al(OBu)_2$(etac) is initiated by the separation of both etac and butoxy groups attached to AlO. The observation of the absorption peaks at 1735 cm^{-1} and 1615 cm^{-1} corresponding to stretching vibrations of C-O bonding for free etac groups in ketonic and enolic forms respectively, conclusively suggests that etac is present in the dried gel as a separate phase in both possible forms [63]. If attached to AlO, etac would be present only in enolic form. An absorption band due to C-H bondings occurs at 1170. The presence of CH_2 is evidenced by two absorptions at 2920 cm^{-1} and 2980 cm^{-1} while the absorption bands at 1370 cm^{-1} and 1420 cm^{-1} are assigned to CH_3 bonding vibration. Finally carbon bondings give rise to two absorptions at 1300 cm^{-1} and 1520 cm^{-1} for C-C and C=C bondings respectively [63], [81].

Separated from AlO as a result of hydrolysis, butoxy ligands give rise to absorption bands in the FTIR spectrum of C12A7 dried gel. As illustrated in figure 5.2, the absorption band at 1060 cm^{-1} is due to the C-O stretching vibration of butoxy ligands, while the Ch_2 and CH_3 vibrations occur at the same absorption bands as those of etac groups [81].

Comparing FTIR pattern for amorphous and crystalline C12A7 provides evidence of the removal of all organic compounds as a result of thermal treatment. Such comparison is also an asset to demonstrate the cage formation in crystalline C12A7. The absorption bands due to the symmetrical vibration of Ca-O-NO_2, as well as the ones in the range of 400-700 cm^{-1} arising from the presence of AlOOH virtually disappear in the FTIR pattern of crystalline C12A7. Typical reported peaks for crystalline C12A7 phase are observed in our data. As stated above there is no evidence of individual Ca-O or Al-O bondings in the FTIR spectrum of crystalline C12A7. Ca, Al and O atoms are confined together to form the Ca-O-Al cage structure vibrating at 530 cm^{-1} exclusively. The free oxygen ions which are trapped inside the cages vibrate at 790 cm^{-1} [84]. Finally the thermal treatment of C12A7 in air is favourable for the incorporation of OH^- ions inside the cages. These ions are identified with the absorption band at 3620 cm^{-1}. The upshift of the absorption peaks due to OH vibration compared to hydroxyl groups in amorphous phase is believed to be due to the fact that OH^- ions inside the cage are loosely bound to the cage wall, vibrating at lower energy levels and higher wavelengths [81], [82].

4.6.2 Raman Spectroscopy

Not all of the normal modes of vibration in a molecule can be excited by FTIR. Raman spectroscopy is complementary to FTIR in the measurement of fundamental molecular vibrations.

Accordingly our FTIR experimental findings are supported and complemented by Raman spectroscopy which was carried on with the same loadings as FTIR. Corresponding Raman shifts are in complete agreement with FTIR data. Figures 4.3 to 4.6 illustrate how the Raman shifts due to organic and inorganic compounds present in amorphous dried gel disappear in the crystalline sample. Comparing FTIR and Raman data the most significant feature is the absent of some specific absorption peaks in Raman spectra conducted in two different laser intensities. The FTIR absorption band at 815 cm^{-1} due to the Ca-O-NO2 bonding is absent in the Raman spectra with lower laser intensity, however increasing the laser intensity this peak is detectable through Raman spectroscopy. The same fact applies to the FTIR absorption band at 520cm^{-1} due to Al-O vibrations. In the same way, some vibrations are not detectable at high laser intensity. An example of such phenomena is noticeable at the FTIR absorption band at 1615 cm^{-1} due to stretching vibration of C-O of etac in enolic form. Specific bonding vibrations may be Raman inactive and not detectable at any laser intensity. These bands are detectable at 1735 cm^{-1} due to stretching vibrations of C-O of etac in ketonic form.

In figure 4.6 visible are two strong Raman shifts at 520 nm and 780 nm due to the crystal structure of C12A7 solely. This pattern perfectly demonstrates how the thermal treatment was adequate to remove all other compounds and form the preferred bondings.

Chapter 5

Morphology and Compositional Studies

Post-fabrication C12A7 samples were subjected to heat treatment at various temperatures in order to achieve desired crystal structure. The morphological and compositional properties of the final C12A7 samples are highly affected by their structure and crystallisation. For this purpose Simultanous Thermal Analysis (STA), X-Ray Diffraction (XRD) and Energy Dispersive X-Ray spectroscopy (EDX) were conducted to develop the knowledge of chemical and physical changes during the heat treatment process because it is important for optimizing the sol-gel processing for device manufacture. This chapter discusses the results of these investigations with physical interpretations.

5.1 Results of Thermal Analysis

Simultaneous Thermal Analysis (STA) was used to investigate the phase transformations and any other thermal phenomena that would occur during heat treatment. Figures 5.1 and 5.2 illustrate the Simultaneous DSC/TGA spectra of the

powders obtained upon heat treatment up to 1100°C at the rate of 10°C/min. This technique measures the difference between the energy inputs and also the change in the mass as a function of temperature showing the weight change or phase transformation between ambient temperature and 1100˚C.

In the DSC diagram there are a number of endothermic and exothermic peaks that are attributed to the phenomenon that occurs at each temperature. These phenomena are listed in Table 5.1.

Three regions of weight loss were observed in the TGA diagram. Table 5.2 lists the phenomena responsible for each of these weight losses. No obvious weight loss was seen above 600°C.

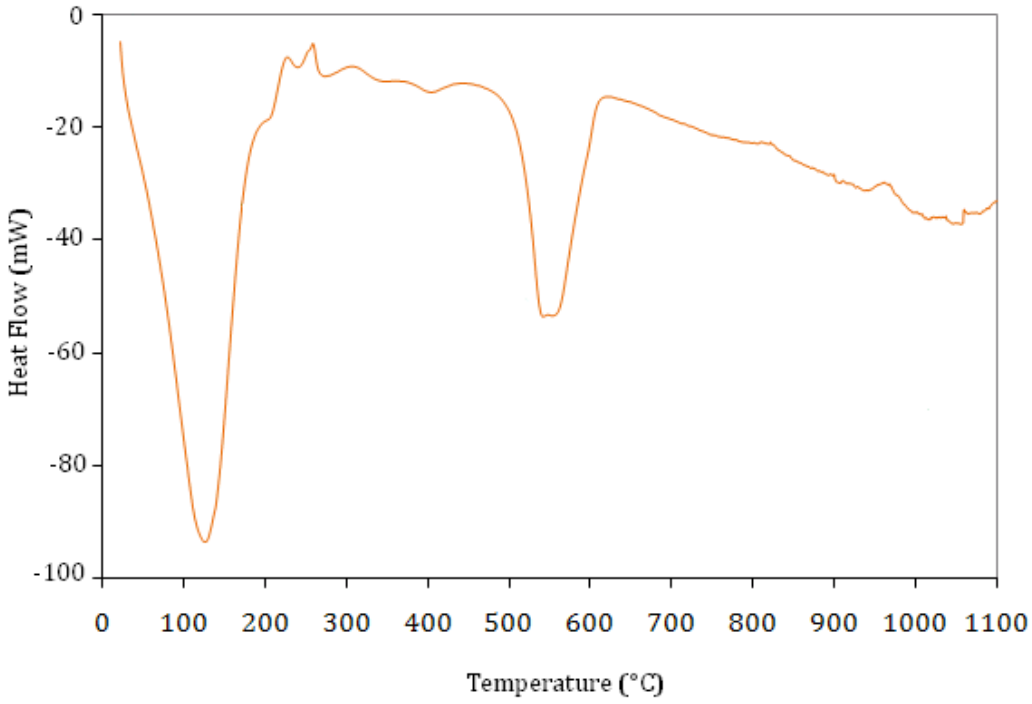

Figure 5.1: DSC pattern of C12A7 dried gel obtained at a heating rate of 10°C/min in a temperature range of 20°C to 1100°C

Table 5.1: List of corresponding phenomena for heat flow changes observed in DSC pattern of C12A7 dried gel during thermal treatment

Temperature (°C)	Peak	Phenomenon	Reference
120	Endothermic	Loss of remaining water and organic solvents	[94], [95]
250	Exothermic	Oxidation of residual organic materials	[67], [96]
250-400	Endothermic	Dehydration of calcium nitrate precursor	[96]
420	Endothermic	Transformation of boehmite to γ-Al_2O_3	[67], [97]
550	Endothermic	Complete decomposition of calcium nitrate to CaO	[95], [99]
820	Exothermic	Crystallization of CaO	[95], [100]
950	Exothermic	Transformation of γ-Al_2O_3 to α-Al_2O_3	[94]

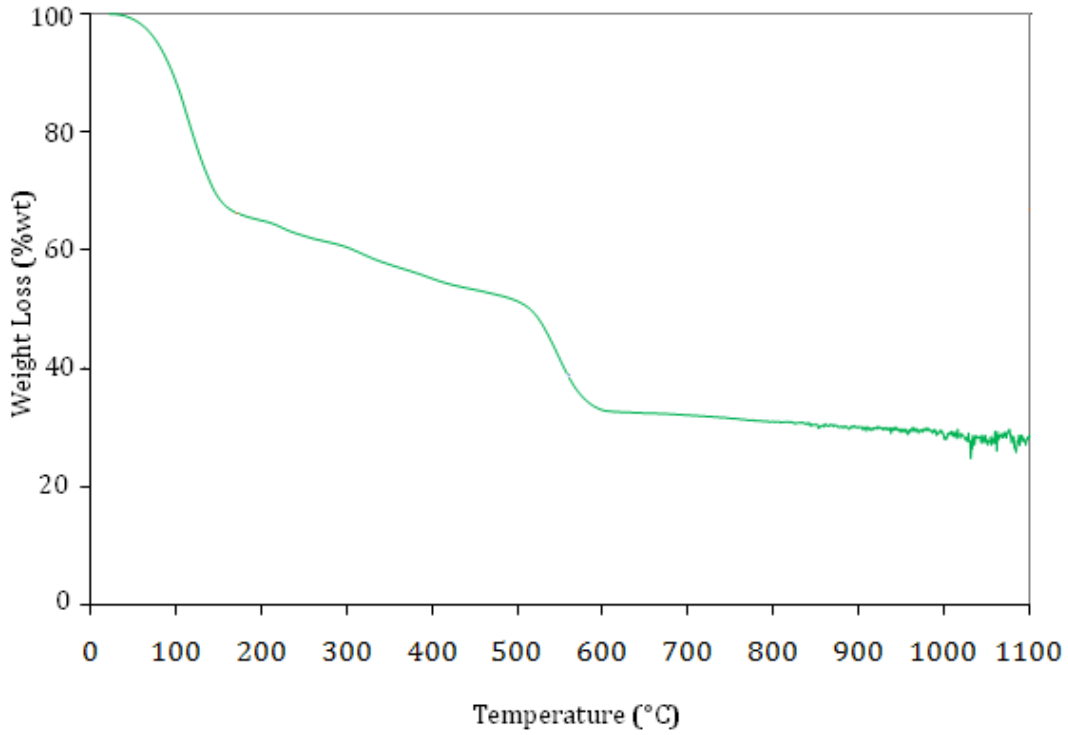

Figure 5.2: TGA pattern of C12A7 dried gel obtained at a heating rate of 10°C/min in a temperature range of 20°C to 1100°C

Table 5.2: List of corresponding phenomena for weight changes observed in TGA pattern of C12A7 dried gel during thermal treatment

Temperature (°C)	Phenomenon	Reference
23-150	Loss of water and organic solvents	[94], [95]
150-500	Dehydration of calcium nitrate and boehmite to γ-Al_2O_3 transformation	[67], [96]
500-600	Decomposition of calcium nitrate to CaO	[95], [98]

The final aspect of the thermal analysis shows how the phenomena involved in the thermal treatment are related to time and heating rate. For this purpose we have conducted the same STA characterisation using three different heating rates of 5°C/min, 10°C/min and 20°C/min. Figure 5.3 shows the corresponding graphs.

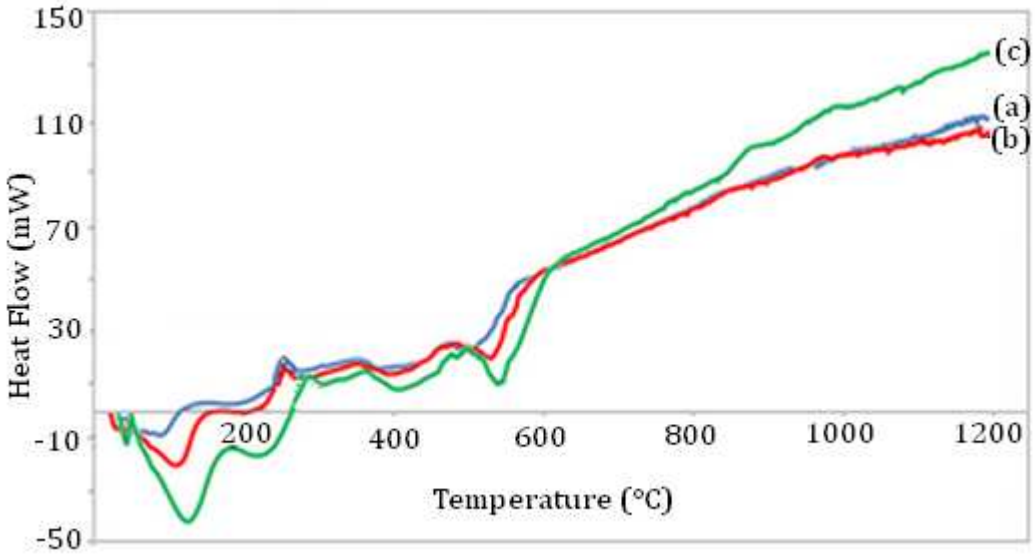

Figure 5.3: STA Pattern of C12A7 dried gel exposed to different heating rates from room temperature to 1200°C. Trace (a) shows the heating rate of 5°C/min, trace (b) is due to 10°C/min heating rate and trace(c) illustrates the 20°C/min heating rate

5.2 Phase Transformation in C12A7

Upon application of thermal treatment of the residue powder of the Sol-gel derived C12A7 there are a number of chemical reactions and phase transformations which occur, leading to the formation of equilibrium C12A7 crystalline phase. As demonstrated in the FTIR and Raman studies, in sol-gel synthesis of C12A7 a number of organic and inorganic components are involved. These chemical and elemental characterization procedures confirmed that during sol-gel processing and the following thermal treatment all the organic/inorganic residue, water and solvents are removed, and the only product remaining is C12A7 with O^{2-} ions trapped inside. We have employed Simultaneous Thermal Analysis (STA) to study any weight change or phase transformation between ambient temperature and 1100˚C.

STA provides a combination of Differential Scanning Calorimetric (DSC) and Thermogravimetric Analyzer (TGA), measuring both enthalpy changes (DSC) and weight gain or weight loss (TGA) during sample transitions as a function of temperature or time. This technique measures the difference between the energy inputs and also the change in the mass as a function of temperature. For the STA analysis the C12A7 dried gel is subjected to a controlled temperature program from room temperature to 1100˚C. The results show a number of endothermic and exothermic peaks arising from different phase and weight changes at various temperatures. These studies were necessary in order to identify the critical

temperature for phase transformations and crystallisation of C12A7 and also the evaporation temperatures for any water, solvents or organic residue.

As depicted in the DSC pattern (figure 5.1), there are a number of endothermic and exothermic peaks that are attributed to the phenomenon which occurs at each temperature. The tetra hydrate molecule attached to $Ca(NO_3)_2$ will boil off giving rise to an endothermic peak at 120°C depending on heating rate [95]. Calcium nitrate will undergo a continuous decomposition process from 250°C – 550°C, during which $Ca(NO_3)_2$ is transferred to CaO [95], [98]. This event is completed at 500°C with a deep endothermic peak in the DSC pattern. This phase is then crystallized at 820°C with the appearance of an exothermic peak. AlOOH present in the sol will not undergo any crystallisation during our thermal treatment, with no evidence of such crystallisation observed in STA patterns (and XRD pattern as will be discussed in the following sections). AlOOH is directly transferred to γ-Al_2O_3 with the appearance of an endothermic peak at 420°C [67], [97]. These results confirm the endothermic nature of this phase transformation. At 950°C the appearance of an exothermic peak illustrates the crystallisation of γ-Al_2O_3 and its transformation to α-Al_2O_3 [94]. It is noteworthy that despite the crystallisation of both CaO and α-Al_2O_3, they do not exist as detached phases. In fact, they do interact with each other to form the framework of C12A7 crystal. C12A7 framework formation is initiated at 900°C -1000°C (as detectable in XRD pattern presented in the following sections). The equilibrium crystal structure of C12A7 is completely formed at 1100°C.

Considering the TGA pattern in figure 5.2, three regions of weight loss are observable. The first region between room temperature to 150°C is due to the removal of tetra hydrate molecule attached to $Ca(NO_3)_2$, water and organic solvents [94], [95]. The dehydration of calcium nitrate and boehmite to γ-Al_2O_3 phase transformation is responsible for the weight loss in the temperature range of 150°C-500°C [67], [96]. The final weight loss region is between 500°C to 600°C and is due to the decomposition of calcium nitrate to CaO. No obvious weight loss was seen above 600°C [95], [98].

This investigation provided information about the phase transformation occurring during the crystallisation of C12A7, revealing required temperature for each phenomenon involved.

Another aspect of the thermal analysis of C12A7 is showing how the phenomena involved in the thermal treatment are related to time and temperature (figure 5.3). Transitions such as evaporation, decomposition, oxidation and crystallization are kinetic phenomena. Therefore they are all functions of both time and temperature [100]. This statement validates the shifts to higher temperatures through increasing the heating rate as observed in figure 5.4. Such sensitivity is believed to be an asset in indentifying the kinetic nature of transitions.

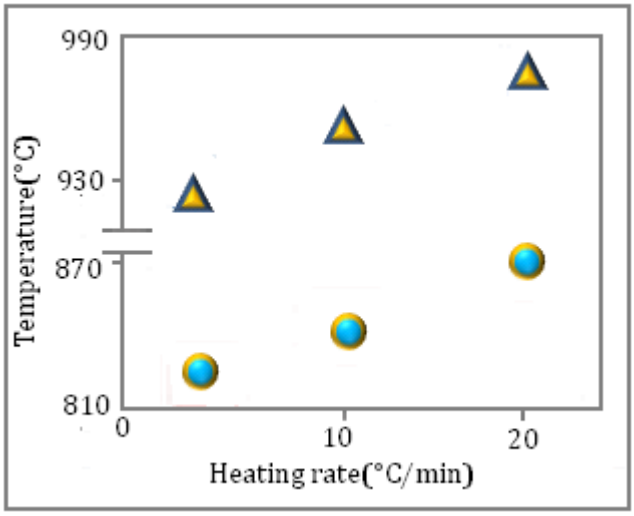

Figure 5.4: Graph showing the direct relation between heating rate and the temperature for exothermic peaks due to CaO crystallization and γ-Al_2O_3 to α-Al_2O_3 transformation. The patterns show the kinetic nature of the events occurring and their dependence on time and temperature

Figure 5.4 also illustrates how the heating rate directly affects the heat flow. The heat flow signal in STA spectrum can be described as:

$$\frac{dQ}{dt} = C_p \frac{dT}{dt} + f(T,t) \qquad (5.1)$$

Where $\frac{dQ}{dt}$ is the differential heat flow rate, C_p is the heat capacity, $\frac{dT}{dt}$is the heating rate and f(T,t) is the kinetic heat flow. This equation shows how the heat flow is directly related to the heating rate [100].

5.3 Results of Elemental Analysis

5.3.1 X-Ray Diffraction

Figure 5.5 shows the X-Ray diffraction patterns for the samples annealed at different temperatures ranging from 700°C to 1200°C. A good agreement is observed between the obtained spectra and those reported from the standard data of C12A7 cubic structure. Table 5.3 summarizes the results of the analysis of the XRD pattern for the sample heat treated at 1100°C, comparing the data to those obtained from International Centre for Diffraction Database.

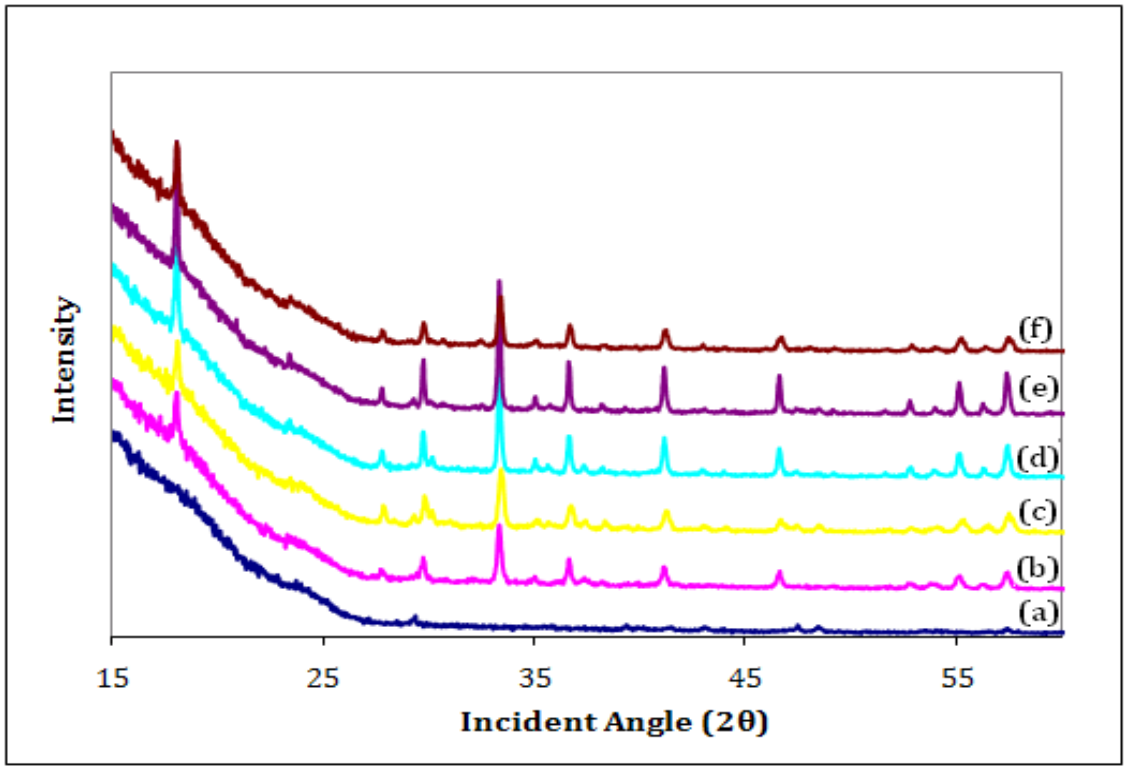

Figure 5.5: XRD diagram of C12A7 sol-gel film annealed at different temperatures; (a) 700°C, (b) 800°C, (c) 900°C, (d) 1000°C, (e) 1100°C and (f) 1200°C

Figure 5.6 shows a sequence of data collected from the HTXRD performed on amorphous C12A7 dried gel in the temperature range of 23°C-1200°C. During the course of these measurements the development of C12A7 crystalline phase is studied. These data will then be compared with those obtained from STA to investigate how these two set of data are in agreement with each other.

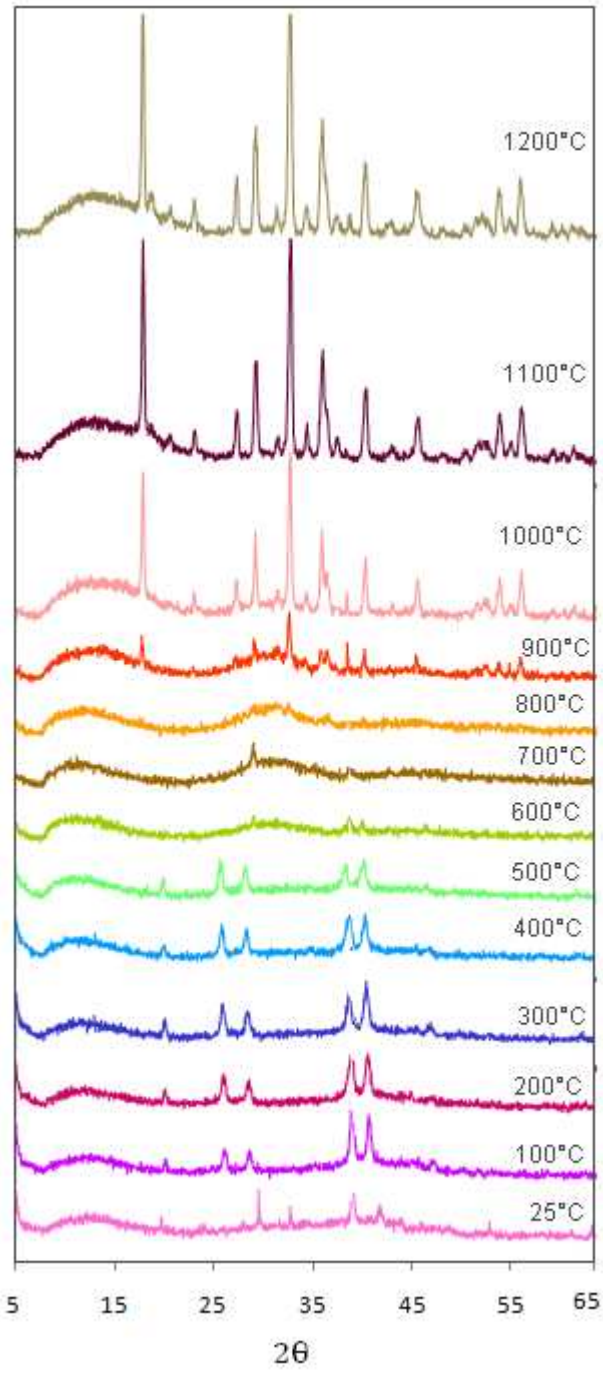

Figure 5.6: HTXRD Pattern of C12A7 obtained at temperature intervals from room temperature to 1200°C

5.4 Elemental and Structural Analysis of C12A7

The crystal structure of a chemical compound can be determined using X-Ray diffraction (XRD). Similar to FTIR and Raman, the XRD pattern of each crystalline material is a unique fingerprint of its atomic structure. Therefore XRD is among the most practical tools for observation of crystalline phases, especially if there is any alteration within the structure due to influential parameters.

In the present work the effect of heat treatment temperature on the crystal structure of C12A7 films has been investigated through XRD. The heat treatment temperature strongly influences the crystal structure of any crystalline material. For C12A7 the thermal analysis conducted on the identical C12A7 sol-gel residue show that the crystallisation results in the release of residual organic compounds, decomposition of precursor compounds and the phase transformation from amorphous gel to crystalline phase when heated to 1100°C. Such crystallisation is the possible result of cage formation using O^{2-} ions as templates, which remain in the structure confirmed from FTIR and Raman spectroscopy.

XRD patterns of C12A7 films subjected to heat treatment at various temperatures ranging from 700°C to 1200°C are presented in figure 5.5. A good agreement is observed between the measured d-values and those reported from the standard data of C12A7 cubic structure, as listed in table 5.3.

Table 5.3: d-Spacings and lattice indices of dominant reflections of standard C12A7. Data obtained from International Centre for Diffraction Database compared with the observed peaks for the sample heat treated at 1100°C

Reference			**Observed**			**Indices**		
2θ	d(A°)	I	2θ	d(A°)	I	h	k	l
18.11	4.895	999	18.1	4.9	439	2	1	1
29.78	2.997	252	29.7	3	92	4	0	0
33.4	2.681	691	33.3	2.7	218	4	2	0
36.69	2.447	340	36.6	2.5	88	4	2	2
41.21	2.189	241	41.1	2.2	80	5	2	1
46.66	1.945	199	46.6	2	67	6	1	1
55.2	1.663	183	55.1	1.7	56	6	4	0
57.47	1.602	209	57.3	1.6	71	6	4	2

It is therefore concluded that the process of crystallisation is initiated at 800°C and will be completed at 1100°C. The film heated at 700°C was believed to be completely amorphous and no crystallisation was observed at temperatures below 800°C. The crystal structure appears to be disrupted at temperatures higher than 1100°C resulting in weakening of the XRD peaks. The deterioration of the peaks was visible in the XRD diagram for the sample heated at 1200°C. It can be concluded from these results that the ideal temperature for the heat treatment of C12A7 is 1100°C.

This temperature will be used more in the following surface morphology analysis, which is shown in figure 5.5 (pattern (e)).

5.4.1 Crystallite Size Analysis by X-ray Diffraction

Structural analysis through XRD not only provides useful information about the crystalline phase formation in the material, but it is possible to evaluate other fundamental parameters affected as a result of heat treatment through a series of mathematical calculations. Such evaluation is based on the peak broadening of the XRD pattern, which may be caused by crystallite size changes as well as strain effects within the crystal.

Williamson-Hall:

In 1953 Williamson and Hall introduced a simple method based on a series of mathematical calculations to evaluate both crystallite size and lattice strain through their contribution to the values of the full width at half maximum (FWHM) of the XRD pattern. According to the equation developed, the crystallite size and the lattice strain of the materials is related to the FWHM as:

$$\beta_f^* = {}^{1}/_{\langle D \rangle_v} + 2\langle \varepsilon \rangle d^* \qquad (5.2)$$

where $\langle D \rangle_v$ is the crystallite size, $\langle \varepsilon \rangle$ is the lattice deformation value, β_f^* is the integral width of a reciprocal lattice point and d^* is the distance of the point from the origin of the reciprocal lattice. β_f^* and d^* values can be calculated from:

$$\beta_f^* = \beta_f cos\theta/\lambda \tag{5.3}$$

$$d^* = 2dsin\theta/\lambda \tag{5.4}$$

where β_f is the full width at half maximum and d is the corresponding d-value at the Bragg angle θ [101], [102].

The values of β_f and d are calculated from figure 5.5 using Panalytical X'pert Highscore program. These calculations lead to a Williamson-Hall plot of β_f^* versus d^*. This plot is presented in figure 5.7 for our calculations. As can be observed, this plot is found to be linear for the samples heat treated at temperatures ranging from 800°C to 1200°C. The sample heat treated at 700°C does not show any sign of crystallinity and has not been considered for the following calculations. The intercept of these plots can be used to calculate crystallite size, while strain is derived from the gradient. Values of mean apparent volume-weighted crystallite size $\langle D \rangle_v$ and effective relative lattice deformation $\langle \varepsilon \rangle$ were estimated from the intercept and slope of the graph, respectively. These values are listed in table 5.4 for various heat treatment temperatures.

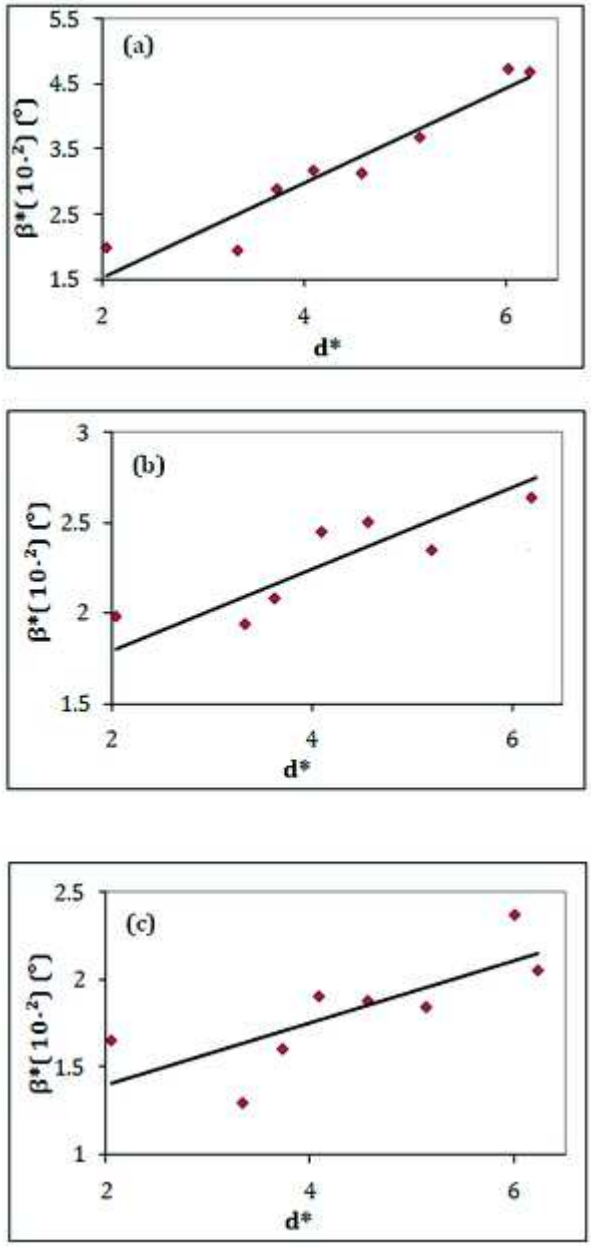

Figure 5.7: Williamson-Hall plot for samples heat treated at (a) 800°C, (b) 900°C, (c) 1000°C, (d) 1100°C and (e) 1200°C

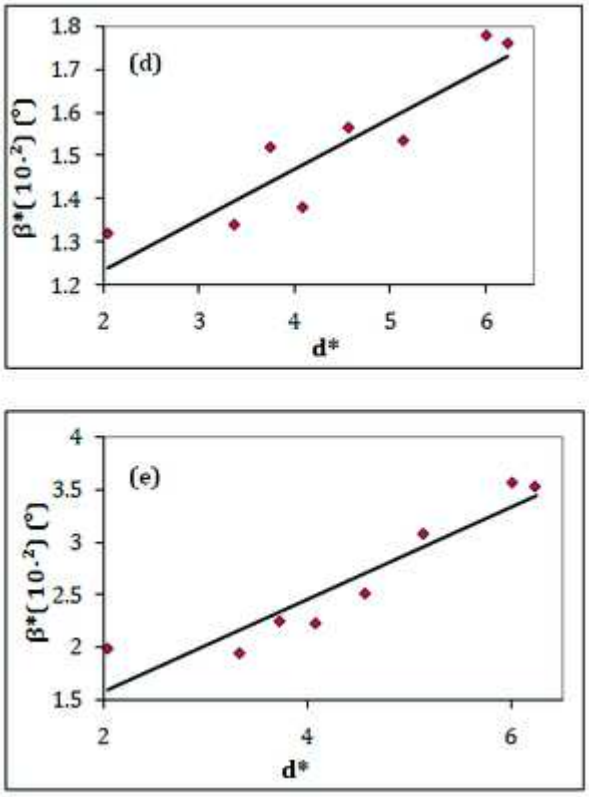

Figure 5.7 (continued)

Table 5.4: Lattice strain and crystallite size values obtained from Williamson-Hull plots in figure 6.6 for samples heat treated at different temperature ranging from 800°C to 1200°C

Temperature (°C)	ε (x 10^{-6})	<D> (nm)
800	3.35	244
900	1.15	75
1000	0.9	95
1100	0.6	100
1200	2.2	144

The values of lattice strain and crystallite size for samples heat treated at temperature rang of 800°C-1200°C are schematically compared in figure 5.8 and 5.9, respectively. As depicted in figure 5.8, the crystallite size values were found to increase from 75nm to 145nm with the rise in annealing temperature from 900°C to 1200°C. Such increase in the grain size was predictable since increasing annealing temperature will improve the conditions for the crystal growth. As a fact higher temperatures will facilitate crystal growth and will result in larger grain size [102].

The large size of crystallites in the sample heat treated at 800°C is a good example of lack of sufficient kinetic energy for atomic arrangement and crystal structure formation. Consequently the long range order causing the scattering of X-Ray beam is not well defined, therefore broadening of the scattered X-Ray intensity occurs [78].

Crystallite growth is also observed for the sample heat treated at 1200°C. As confirmed through the thermal analysis, the crystallisation of C12A7 will start at

820°C with the development of CaO phase and will be completed at 1100°C. In this range for temperature the crystal structure will improve and the XRD pattern shows better defined scattered X-Ray peaks. Further rise in heat treatment temperature will only corrupt the crystal structure and the long range order. Such disruption may not be observable in crystallite size measurements, but can be identified through the lattice strain measurements.

As illustrated in figure 5.9, increasing thermal treatment temperature from 900°C to 1100°C causes a reduction in lattice strain from $1.15X10^{-6}$ to $0.6X10^{-6}$. These results are in agreement with the strain relaxation phenomena. It is confirmed that heat treatment will result in lattice relaxation and consequently decreasing the lattice strain values. The phenomenon reported for the sample heat treated at 1200°C can be truly observed in the lattice strain values. Increasing heat treatment temperature to 1200°C caused a sudden increase in lattice strain. This effect is a consequence of the crystal structure disruption at high annealing temperatures as mentioned earlier. The high values of lattice strain of the sample heat treated at 800°C is also noteworthy. This effect was expected since the 800°C heat treatment temperature would not provide adequate kinetic energy for atoms to be arranged in C12A7 crystal structure, taking more random ordering which consequently increases the lattice strain.

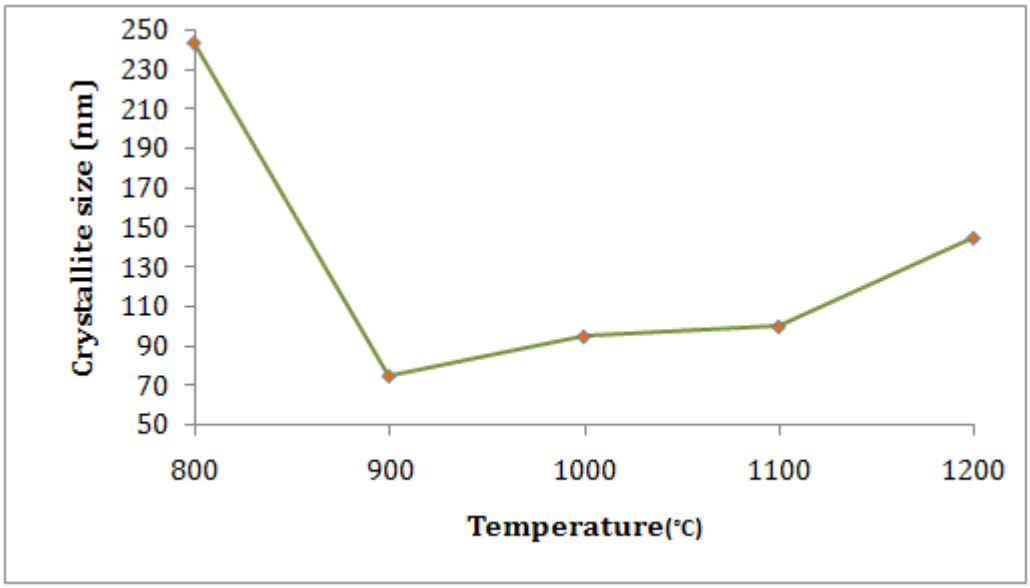

Figure 5.8: Crystallite size versus heat treatment temperature derived from Williamson-Hall pattern

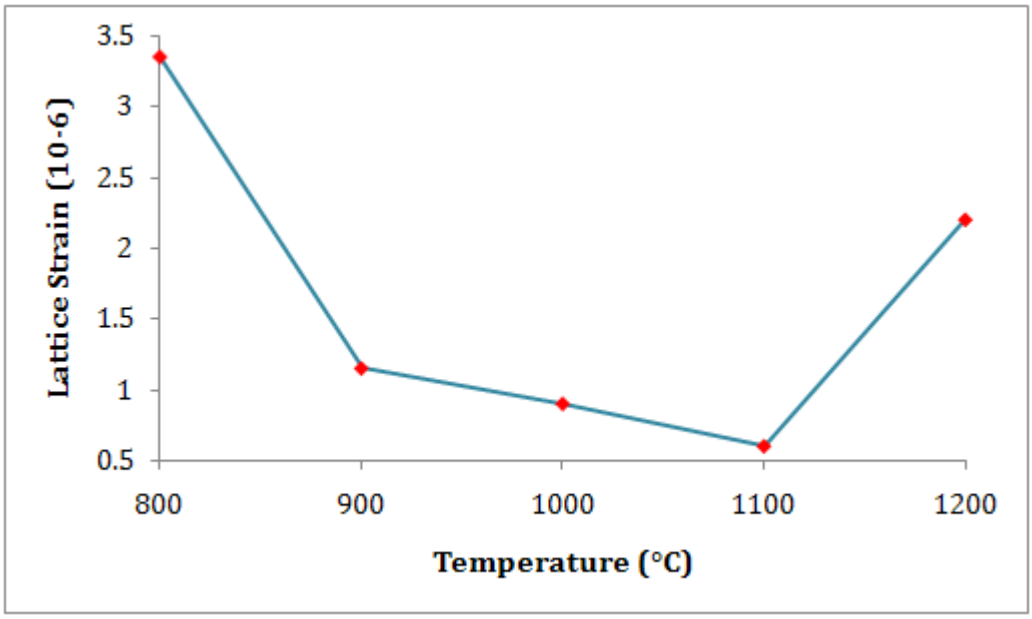

Figure 5.9: Lattice strain versus the heat treatment temperature derived from Williamson-Hall pattern

5.4.2 High Temperature XRD (HTXRD)

HTXRD allows X-Ray spectroscopy while the sample is subjected to thermal treatment. Diffraction patterns can be collected at specified temperature intervals during heat treatment, providing a route for observation of any structural changes during crystallisation. In the present project HTXRD is found a reliable tool in identifying any phase transformation that may occur as a consequence of sol-gel processing.

Figure 5.6 shows a sequence of data collected from the HTXRD performed on amorphous C12A7 dried gel in the temperature range of 23°C-1200°C. A new phase began to form at 100°C, which by 400°C completely dominated the XRD pattern. This phase completely diminishes at 600°C and there is no visible structural change is observed from 600°C to 900°C. At 900°C a new crystalline phase is formed, with increasing crystallinity up to 1200°C.

During the sol-gel process two distinct compounds will be formed at room temperature; one is $Ca(NO_3)_2$ and the other is AlOOH. Calcium nitrate is a metallic salt and exists as a cubic crystalline phase in space group *P213* at room temperature. It is reported that if the solvent used to dissolve $Ca(NO_3)_2$ is removed, this phase can recrystallise into calcium nitrate [98]. This structure is depicted in figure 5.10 (a) with the diffraction pattern at 400°C fitting the one for $Ca(NO_3)_2$ collected from International Centre for Diffraction Database. This pattern remains strictly identical to the one for $Ca(NO_3)_2$ up to 500°C. As stated in thermal analysis, calcium nitrate

will undergo a continuous decomposition process from 250°C – 550°C, during which $Ca(NO_3)_2$ is transferred to CaO [95], [96], [98]. This event is completed at 500°C - 560°C. Such phase transformation causes the disappearance of the diffraction pattern of $Ca(NO_3)_2$ at 600°C.

AlOOH present in the sol will not undergo any crystallisation during our thermal treatment, with no evidence of such crystallisation observed in neither HTXRD nor STA patterns. AlOOH is directly transferred to γ-Al_2O_3 at 420°C [90], [97], while γ-Al_2O_3 is transformed to α-Al_2O_3 at 950°C [94].

It is noteworthy that despite the crystallisation of both CaO and α-Al_2O_3, they do not exist as detached phases. In fact they do interact with each other to form the framework of C12A7 crystal. C12A7 framework formation is initiated at 900°C - 1000°C as detectable in HTXRD pattern obtained at 900°C or above. The cubic crystal structure of C12A7 is completely formed at 1100°C in a $I\bar{4}3d$ space group. This structure is depicted in figure 5.10 (b) fitting the one for C12A7 collected from International Centre for Diffraction Database. As confirmed through Williamson-Hall calculations increasing the thermal treatment temperature to those higher than 1100°C will affect the crystal distortion.

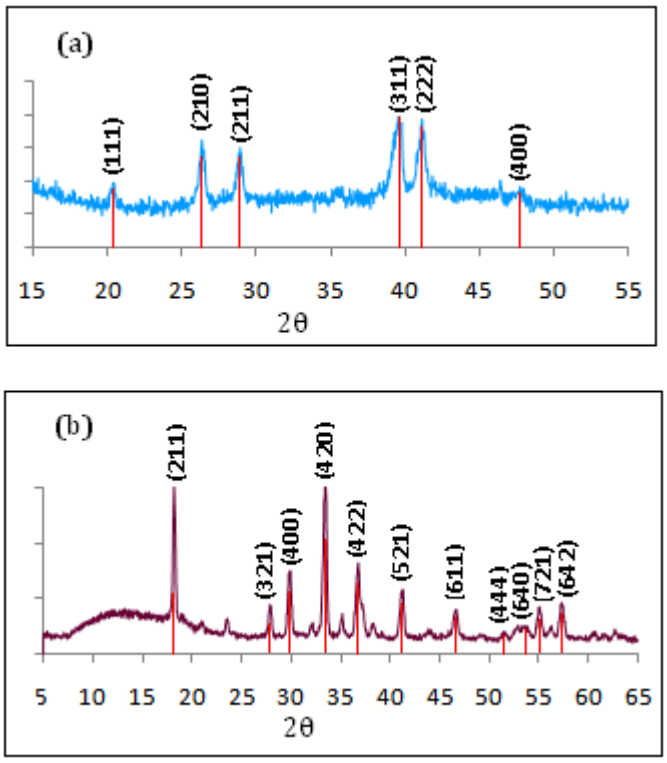

Figure 5.10: Fitted XRD pattern for (a) $Ca(NO_3)_2$ at 400°C HTXRD and (b) C12A7 at 1100°C HTXRD, (Reference data collected from International Centre for Diffraction Database)

5.5 Elemental Analysis using EDX

EDX spectroscopy is normally used as a complementary to XRD. In this technique a high energy beam of charged particles is radiated to the sample surface, causing X-Ray beam emission from the surface. This chemical characterisation technique is based on the same principle as of XRD, which is each element has a unique response

to the incident charged particles targeting its atomic structure. This characteristic feature allows identification of each element present on the film surface through its X-Ray fingerprint.

Figure 5.11 shows the EDX results performed on the surface of the sample heat treated at 1100°C for 3 hours. The elemental composition of the sample surface composition was found to be of 35.57 : 64.43 (wt %) ratio for Al_2O_3:CaO. This value is in agreement with C12A7 nominal composition.

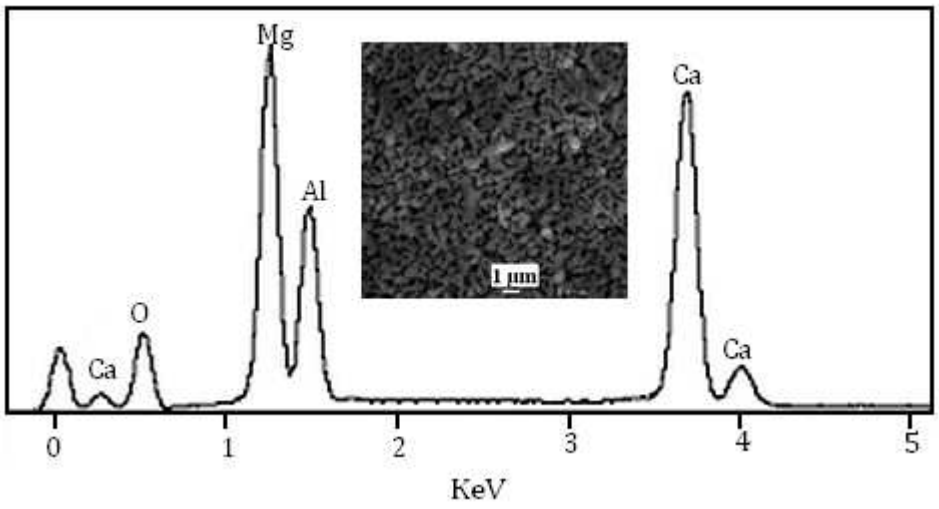

Figure 5.11: EDX spectrum of C12A7 film heat treated at 1100°C for 3 hours. Inset shows the SEM image of the surface EDX data were collected

Chapter 6

Energy Band Diagram of C12A7

The present investigation aims to cover the theoretical interpretation of the energy band- diagram of C12A7 through optical characteristics. For this purpose this chapter is presented to provide the required knowledge for the analysis of the optical response of C12A7. Various absorption behaviors occurring in amorphous and crystalline materials are explained, as well as a simplified approach to use Tauc's law is introduced.

6.1 Optical Spectroscopy

Figure 6.1 shows the optical absorption spectra obtained from the films deposited on MgO single crystal <100>. This spectroscopy is conducted in the visible range wavelength. The films were exposed to thermal treatment at 900°C, 1000°C and 1100°C. There are two absorption peaks observable within these spectra. Using the optical absorption data it is possible to employ these findings to understand the energy band diagram of this material.

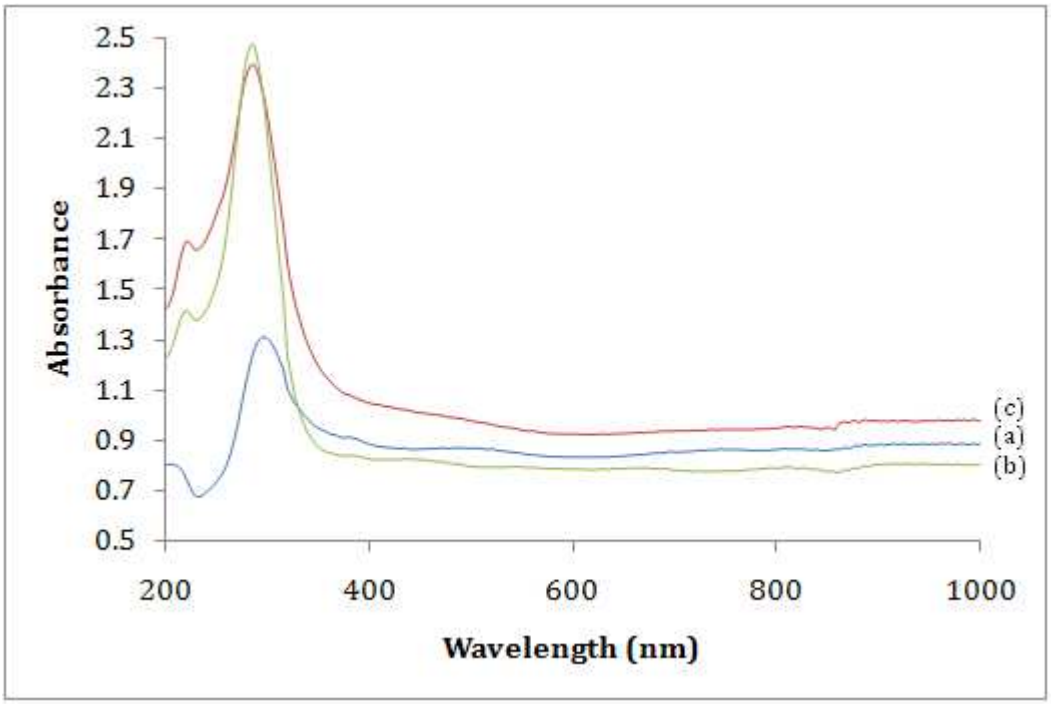

Figure 6.1: Absorption as a function of wavelength for samples heat treated at various temperatures ranging from 900-1100°C

6.2 Optical Spectroscopy

Optical spectroscopy is believed to be the most reliable technique to characterize the band structure of an amorphous or crystalline solid. The principle of optical absorption can be explained through band theory.

When the photon hits a solid, electrons will be excited from their ground state to their excited state. If the photon energy is large enough the electrons will be excited from the valence band to the conduction band, causing the optical absorption at that

specific photon energy. A large gap between the valence band and the conduction band is representative of an insulating or dielectric solid, where a small band gap is the characteristic of semiconductors [103]. The photon energy required for the absorption to happen should be equal or greater than that of the band gap:

$$hv = \frac{hc}{\lambda} \geq E_g \qquad (6.1)$$

where h is Planck's constant, v is the frequency of the incident photon, λ is the wavelength of the incident photon and E_g is the energy band gap of the solid. Such excitation is normally identified as a sudden increase in the absorption at the required photon energy [71].

The insulating and semiconducting materials can be subdivided to direct/indirect categories according to the geometry of their energy-band diagram. Those in which the highest occupied valence band (HOMO) is at the same position in k-space as the lowest unoccupied conduction band (LUMO) are termed direct band material. On the other hand if the HOMO and LUMO occur at different k values the crystalline material is called indirect gap material. The mechanism of charge transition is schematically illustrated in figure 6.2, which shows the Energy-band diagram versus k-space for a direct and indirect band gap material [104], [105]. In this diagram E is the kinetic energy and k is the wave vector of the electron or hole and they are related to each other as:

$$E = \frac{h^2 k^2}{4\pi^2 m_*} \qquad (6.2)$$

where $m_*$is the electron or hole effective mass [105-108].

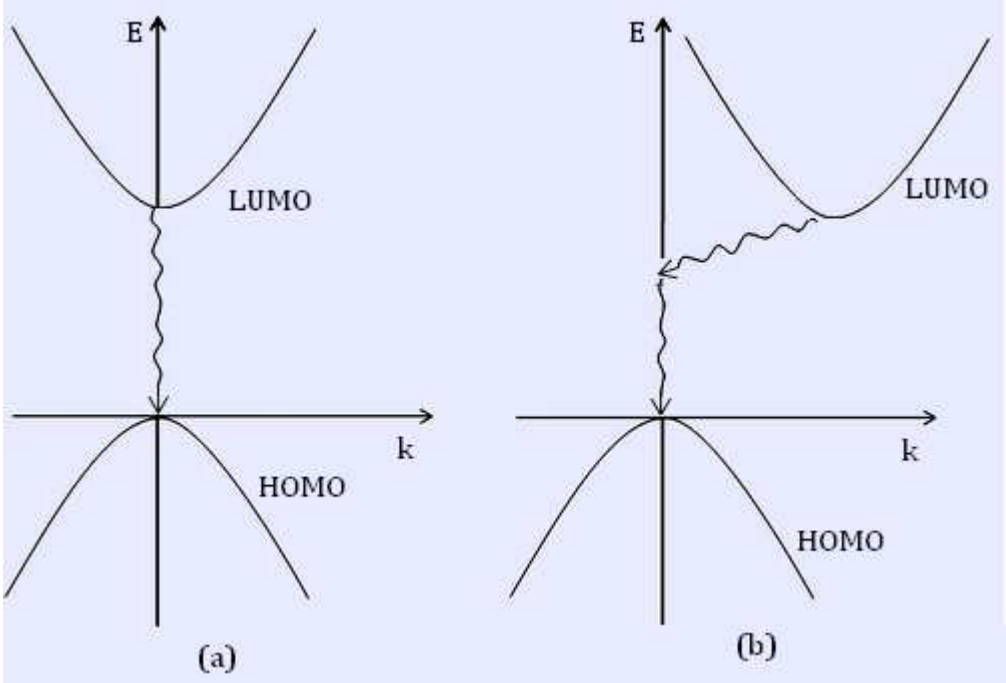

Figure 6.2: Energy-Band diagram of (a) direct, (b) indirect band gap material, showing the position of LUMO and HOMO

The optical absorption spectrum of direct band gap solids can be divided into two main sections:

1) Tauc Absorption Region; where the photon energy is greater than the band gap of the solid and the Absorption can be related to the photon energy according to Tauc's law:

$$A(hv) = \left(\frac{Bd}{hv}\right)(hv - E_{Tauc})^{1/2} \qquad (6.3)$$

where the parameter E_{Tauc} represents the Tauc's energy gap and B is a constant depending on the minimum metallic conductivity σ_o, refractive index μ, the width of band edges ΔE and the nature of electronic transition [109-111].

2) Urbach Absorption Region in which the absorption depends exponentially on the photon energy, which is described as:

$$A = A_0 \exp\left[\left(\frac{hv - E_o}{E_u}\right)\right] \qquad (6.4)$$

where σ is the steepness parameter and K is the Boltzmann constant and E_u is the Urbach's energy.

6.2.1 Urbach's Principle

According to Density of States (DOS) and carrier contribution theory the DOS for a carrier transition is related to the energy band gap of solid through an equation similar to that of Tauc's Law:

$$N(E) = \frac{4\pi(2m_r)^{3/2}}{h^3}(hv - E_g)^{1/2} \qquad (6.5)$$

where N(E) is DOS (that is the number of available states for occupation at each energy level), m_r is the reduced effective mass (related to the electrons and holes effective mass) [109-111].

In theoretical calculations if $E_g=hv$ then $N(E)=0$, which means that the DOS is zero at the band gap of the solid. In practice this is not valid. In 1953 Urbach was the first to find the exponential increase of the absorption with the photon energy, introduced as "Urbach's tail". As illustrated in figure 6.3 the band tails are formed as a result of the perturbation of the valence and conduction bands smearing due to disordering caused by structural features as well as induced external factors such as doping [112].

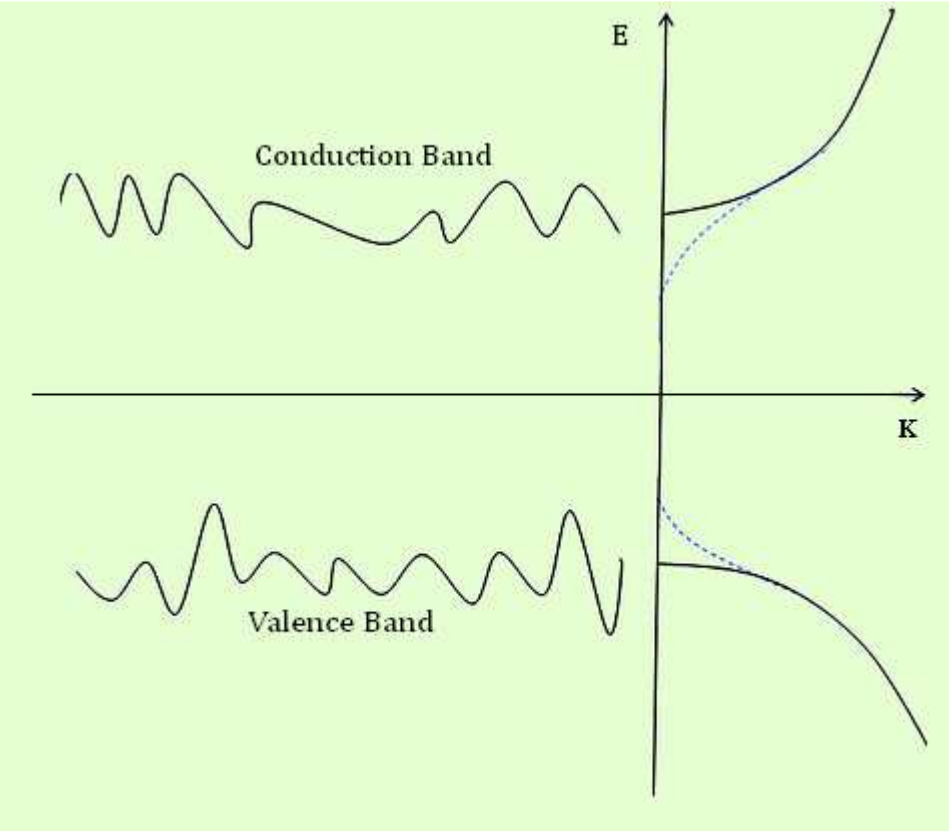

Figure 6.3: The disordering of the conduction and valence band and the resulting band tails (dashed lines). The solid lines show the density of states without perturbation.

The presence of intrinsic and extrinsic defects or impurities greatly affects the distribution of the states, causing more perturbation.

6.3 Optical Studies on C12A7

Figure 6.4 shows the absorption spectra of C12A7 films subjected to heat treatment at temperature ranges of 900°C-1100°C as a function of incident photon energy. Using calculations derived from Tauc's law, different energy levels associated within C12A7 has been evaluated. The values of the Urbach energy (E_u) are identified as a modification to the fundamental energy level values.

It is observed from the spectra presented in figure 6.4 that there are two distinct absorption regions for each of the samples under investigation. The first region with much higher intensity appears in the photon energy between 3.7-4.6eV, while the second one is noticeable in the photon energy range of 4.6-5.8eV.

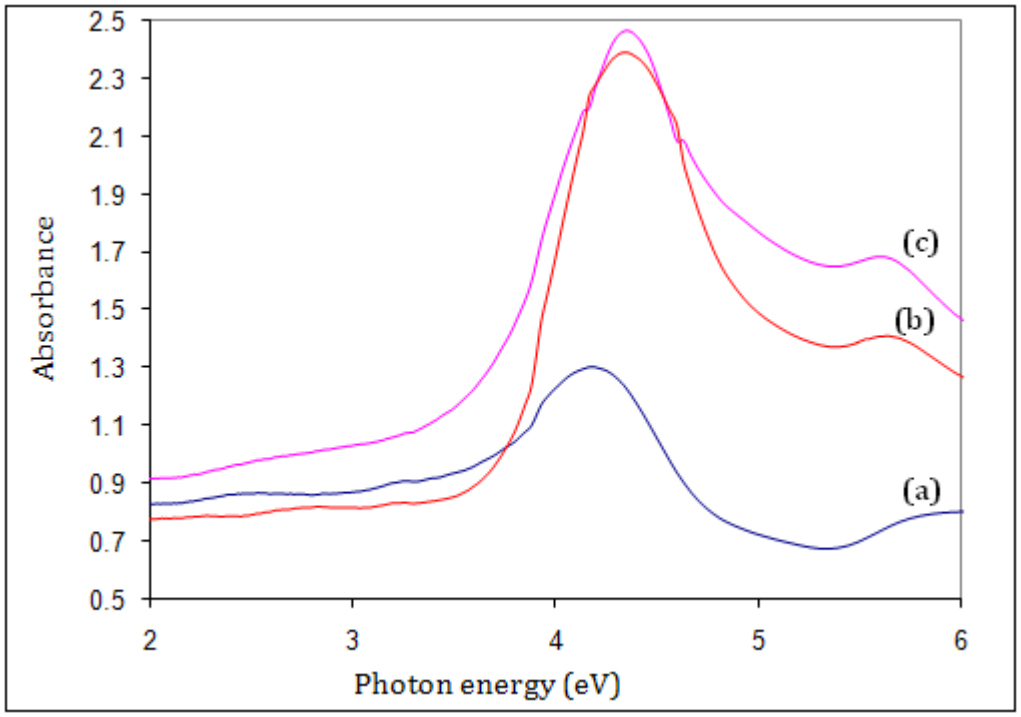

Figure 6.4: Absorbance spectra of samples heat treated at (a) 900°C, (b) 1000°C and (c) 1100°C

6.3.1 Tauc's Calculations

Employing Tauc's law to the optical absorption spectrum is a useful tool in exploiting various features of electronic structure of a material. According to Tauc when a quantum of radiation is focused on a material, the absorption as a function of photon energy can be expressed as:

$$A(hv) = \left(\frac{Bd}{hv}\right)(hv - E_{Tauc})^n \qquad (6.6)$$

where the parameter E_{Tauc} and the power index n represent the Tauc's energy gap and the electronic transitions associated with optical processes, respectively. B is a constant depending on the minimum metallic conductivity σ_o, refractive index μ, the width of band edges ΔE and the nature of electronic transition [113], [114]. The power index can only take values of 1, 2, 3, 1/2, 1/3, depending on the electronic transition nature. When n=1/2 it indicates allowed direct transition, while n=2 and n=3/2 represent allowed indirect and forbidden indirect transitions [115], respectively.

Equation (6.7) can be rewritten as:

$$\frac{Y}{Y'} = \frac{hv - E_{Tauc}}{n} \qquad (6.7)$$

where Y=A(hv) and

$$Y' = \frac{d[A(hv)hv]}{d(hv)}$$

A fit to the experimental data revealed a straight line, the slope of which gives values for n indicating the transition nature while the intercept is E_{Tauc}/n where the E_{Tauc} can be easily extracted.

Figures 6.5 shows the ratio $^{Y}/_{Y'}$ vs. *hv* for the absorption regions of 3.8-4.3eV for the samples heat treated at two annealing temperatures of 1000˚C and 1100˚C.

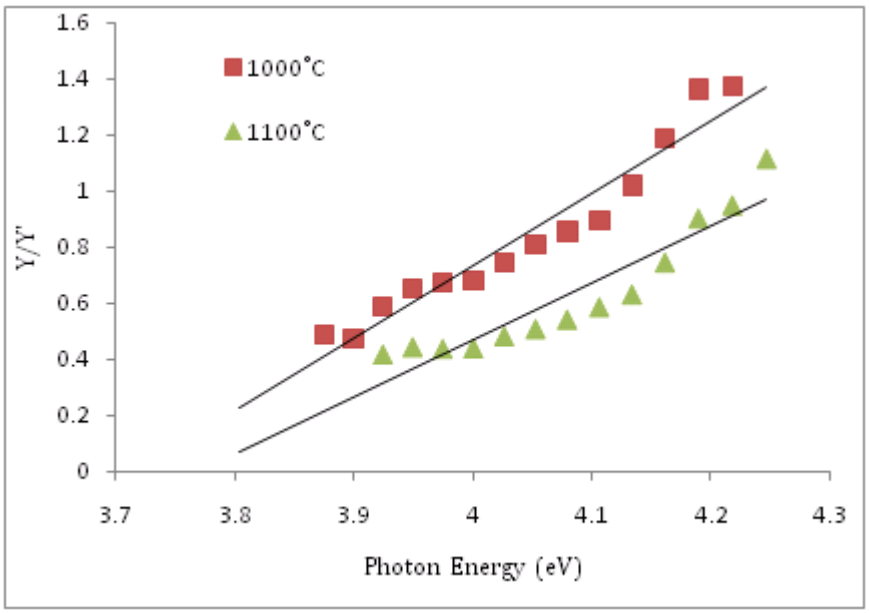

Figure 6.5: Graphs showing the linear dependence of Y/Y′ on incident photon energy in the range of 3.75-4.3eV for samples heat treated at 1000˚C and 1100˚C

The values of Tauc's energy gap are plotted in figure 6.6 versus heat treatment temperature. As can be observed higher thermal treatment temperature has a direct effect on the Tauc energy gap. Increasing the thermal annealing temperature directly affects the degree of crystallisation, leading to the appearance of more crystallites within the region on which the beam is focused. This would consequently

lead to less perturbation in the electronic structure of C12A7, resulting in the appearance of larger energy gaps [116].

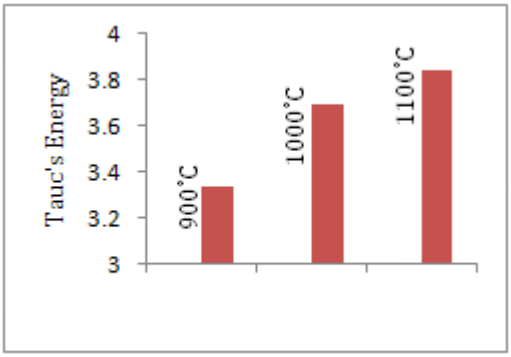

Figure 6.6: Tauc's energy gap versus thermal annealing temperature for C12A7 thin films

The Tauc's calculations also revealed that electronic transition within any allowed energy level of C12A7 is a "direct transition" in k-space taking the value of ½ for the power index.

6.3.2 Urbach's Calculations

The absorption spectra show an extending tail for lower photon energies below the band edge for the absorption edge in the region ranging from 3.7-4.3eV. This

band tail can be evaluated using Urbach's rule. To evaluate the Urbach's energy, the logarithmic variation of A is plotted against photon energy *hv* in the 3.8-4.2eV region. This plot is presented in figure 6.7 for several thermal treatment temperatures between 900°C-1100°C for C12A7 thin films. Linear dependence at each temperature is observed over a wide range of *hv*.

This behaviour is in agreement with Urbach's rule. The values of Urbach's energy were evaluated through fitting the linear part of the lnA versus *hv* as:

$$\propto = \propto_0 \exp\left[\frac{\sigma}{KT}(hv - E_o)\right] \qquad (6.8)$$

Urbach's energy is defined as $E_u = \frac{KT}{\sigma}$, where σ is the steepness parameter and k is the Boltzmann constant [117], [118]. Knowing that α=2.3A/d, where d is the thickness of the film, it is possible to rewrite equation (6.8) as:

$$A = A_0 \exp\left[\left(\frac{hv - E_o}{E_u}\right)\right] \qquad (6.9)$$

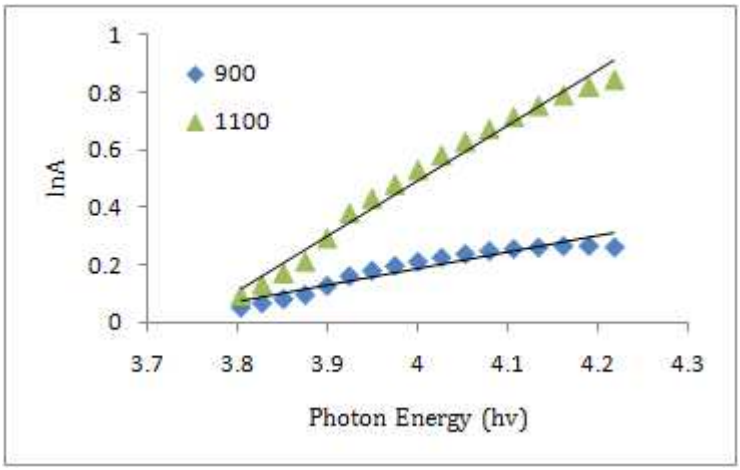

Figure 6.7: lnA versus hv plot showing the linear dependence of lnA on incident photon energy in the range of 3.75-4.3eV for samples heat treated at 1000˚C and 1100˚C

The value of E_u can be calculated from the gradient of the linear plot. Figure 6.8 shows how Urbach's energy values decrease with increasing heat treatment temperature. Increasing heat treatment temperature decreases the perturbation of the energy levels, decreasing the extension of these bands into the band gap [119-121]. These values along with the values obtained from Tauc's calculations are listed in table 6.1.

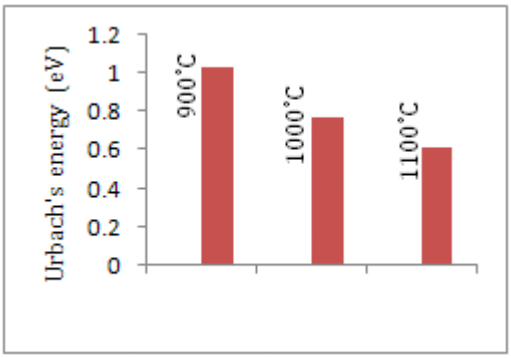

Figure 6.8: Urbach's energy gap versus thermal annealing temperature for C12A7 thin films

Table 6.1: Tauc's energy, Urbach's energy fundamental energy gap, power index and electronic transition evaluated from Tauc and Urbach's calculations for C12A7 thin films heat treated at 900°C, 1000°C and 1100°C

Temperature	**900˚C**	**1000˚C**	**1100˚C**
Tauc Energy (E_{Tauc})	3.34eV	3.70eV	3.84eV
Urbach Energy (E_u)	1.03eV	0.77eV	0.62eV
Band Gap Energy (E_g)	4.37eV	4.47eV	4.46eV
Power Index (n)	0.51 (±0.001)	0.48 (±0.001)	0.47 (±0.001)
Nature of Transition	Direct	Direct	Direct

These calculations have only been applied to the lower absorption region of 3.8-4.3eV. The higher absorption region between 4.6-5.8eV has lower intensity and is extended over a wide photon energy. Such characteristics make it impossible to apply the same calculations for the absorption range. We have therefore estimated the energy gap from the maximum absorption values for this region.

6.4 Energy-Band Diagram of C12A7

The estimated energy level for the transition in K-space related to the absorption region under investigation is demonstrated in figure 6.9. As illustrated the energy levels are extended into the band gap.

Finding the calculated and estimated values for the fundamental energy levels involved in the electronic structure of C12A7, we have estimated the energy-band diagram of C12A7 based on these values. These values are in good agreements with the values derived by previous researchers using Quantum Mechanics (QM) Cluster modelling [52].

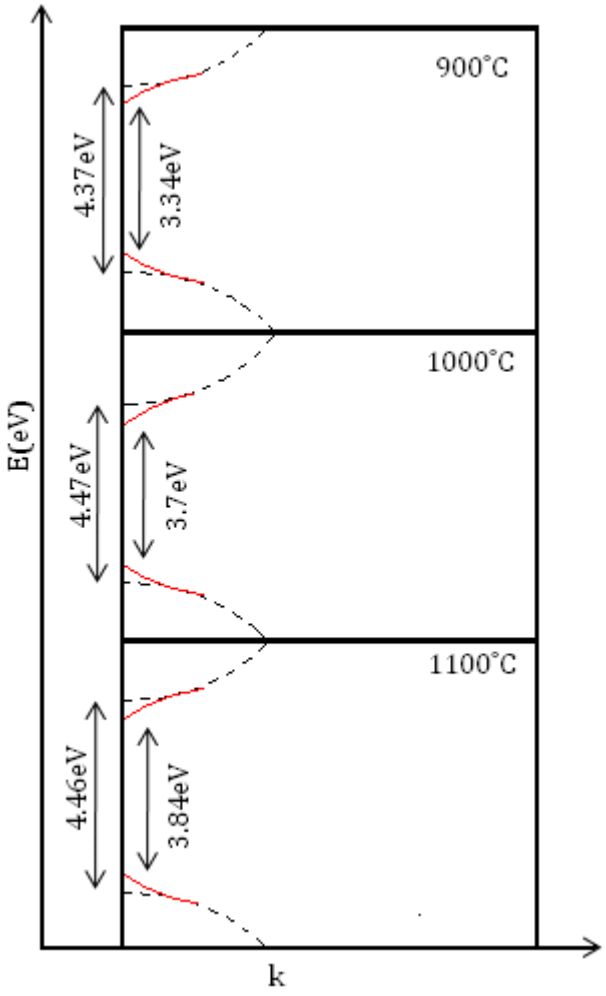

Figure 6.9: Energy diagram estimated for C12A7 films heat treated at different temperatures showing the tails of states. The dashed lines show the distribution of states in the unperturbed situation.

The optical characteristics of C12A7 and the cause of the appearance of the absorption regions are directly related to the presence of nanocages and trapped oxygen ions.

Shushko et al., have carried out a comprehensive calculation on the energy levels of one-electron states associated with the framework with and without extra-framework species. It has been revealed that there are two unoccupied states present in the electronic structure of C12A7:

(i) *Framework Conduction Band* (FCB): i.e., the states associated with the framework alone forming a FCB ~7.3eV above the valence band;

(ii) *Cage Conduction Band* (CCB): i.e., the states localized in the cages formed as a result of the positive charge of the cage wall. These states form a narrow CCB that is ~5.9eV above the top of the valence band [52].

Figure 6.10 shows the one-electron energy levels and the position of O^{2-}.

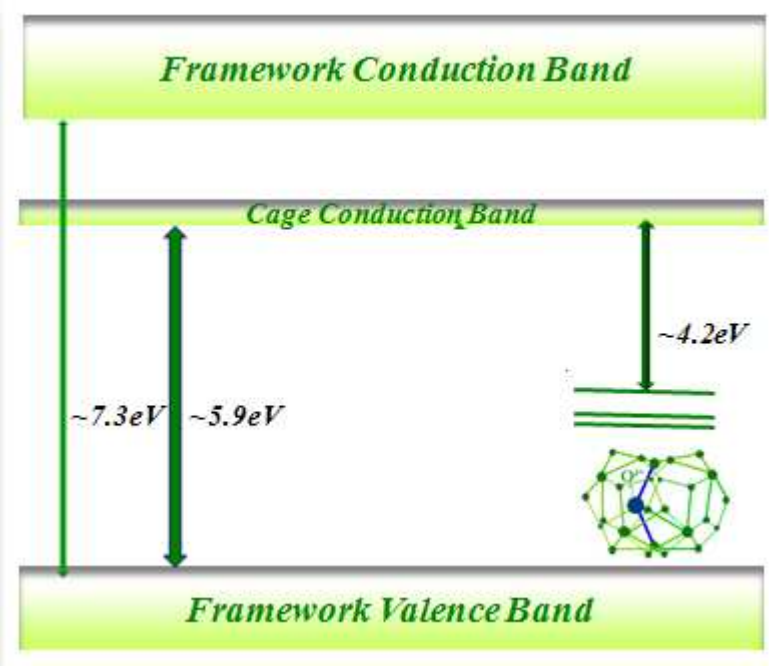

Figure 6.10: One electron energy states formed by framework and extra-framework species of C12A7.

Due to the presence of O^{2-} ions three 2p states are introduced at 1.1eV, 1.2eV and 1.8eV above the top of the valence band. The first absorption region observed in the optical absorption spectra ranging from 3.7eV to 4.3eV is mainly attributed to the states formed by O^{2-} ions inside the cages. According to the embedded cluster calculations employed by *Shushko et al*, the O^{2-} ions have an off-centre configuration inside the cages. This configuration induces an unoccupied state inside the occupied cage hosting O^{2-} being identified as a perturbed CCB state. As a result, two CCB states are localised within the QM cluster rather than one. Thus, there will be six O^{2-}→CCB

transitions occupying the energy range from 3.7eV to 4.4eV. The presence of O^{2-} ions contribute to the region of energy from 3.7eV to 4.6eV observed in the optical absorption spectra.

The region of energy from 4.6eV to 5.6eV is occupied by O^{2-}→FCB transitions. At energy levels higher than 5.6eV they began to overlap with VB→CCB transitions. There is also a chance of OH^- being incorporated inside the cages as a result of heat treatment in air. These ions form two energy levels within C12A7 one electron state. The first one is associated with the transition from OH^- ions CCB which is formed at 5.1eV. Due to a large spatial separation of the states formed by OH^- ions as the extra-framework species and the empty cages, the probability of an OH^-→CCB transition is low. The probability of an OH^-→FCB transition is much greater and forms a state at ~5.7eV. The absorption peak at 5.7eV due to OH^-→FCB transition overlaps the O^{2-}→FCB and VB→CCB [52].

Chapter 7

Conclusion and Future Work

7.1 Conclusion

The sol-gel derived binary compound, C12A7 of the CaO - Al_2O_3 system was successfully fabricated from transparent and homogenous sols. Precise control over the chemical composition of precursors, concentration of solvents and water and the pH of the sol were found to be the most important parameters. Appropriate molar ratios are listed in table 7.1.

Table 7.1: Molar ratios of the starting materials for sol-gel fabrication of C12A7

Molar Ratio	**Reaction**
$Al(OBu)_3$: etac=1:1	modified $Al(OBu)_2(etac)$ complex formation
$Al(OBu)_3$:H2O: HCl = 1: 3: 0.075	successful hydrolysis of $Al(OBu)_3$
$Ca(NO_3)_2$. $4H_2O$: ethanol = 2 : 5	dissolution of $Ca(NO_3)_2$. $4H_2O$
$Ca(NO_3)_2$. $4H_2O$: H_2O = 3:4	partial hydrolysis of $Ca(NO_3)_2$

For this purpose the pH of the solution was adjusted as follows:

- pH $_{AlOOH\ sol}$ =8- below the IE point of AlOOH particles
- pH $_{CaO\ sol}$ = 4- below the IE point of CaO particles

The effect of heat treatment on pristine was studied with conducting the heat treatment at various temperatures. The crystallisation temperature for both C12A7 powders and thin film was confirmed to be 1100°C, according to XRD studies. A grain growth of 75nm to 145nm and reduction in lattice strain from $1.15X10^{-6}$ to $0.6X10^{-6}$ were found using Williamson-Hall calculations.

The nature of the chemical reactions involved in the sol-gel processing was investigated using FTIR and Raman spectroscopy. It was also revealed that all the chemical compounds present in the dried gel were removed after thermal treatment.

STA measurements revealed the phase changes and chemical decompositions occurring during thermal treatment. These phenomena included water and solvent evaporation, calcium nitrate decomposition, boehmite to γ-Al_2O_3 transition and C12A7 crystallisation at different temperatures.

UV-Vis spectroscopy of such uniform film revealed information about the energy band diagram of C12A7 which are necessary for future work. The energy levels of C12A7 were calculated using Urbach's rule and Tauc's calculations. C12A7 follows a direct charge transition and has a wide band gap of ~7.3eV. The presence of a number of energy levels in this oxide has made C12A7 a candidate for efficient

electronic/optoelectronic applications. According to our calculations the energy levels are assigned as follow:

- O^{2-}→CCB Transitions - 3.7eV to 4.4eV
- O^{2-}→FCB Transitions - 4.6eV to 5.6eV
- VB→CCB Transitions - 5.6eV
- OH^- → CCB Transitions - 5.1eV
- OH^-→FCB Transitions - 5.7eV

7.2 FUTURE WORK

Further investigation is required to utilize sol-gel processing for incorporation of high concentrations of electrons into C12A7 nano-caged structure. In particular emphasis should be placed on the use of this amorphous phase as an oxygen ejector layer through which conversion of insulating C12A7 into conductive one will be achieved. As depicted in figure 7.1, a top amorphous sol-gel derived C12A7layer can be deposited on top of the insulating layer fabricated. Subsequent heat treatments will enhance oxygen ions ejection from the insulating layer since amorphous C12A7 is reported to be the most suitable reducing agent. For this purpose a number of parameters should be modified. These parameters include heat treatment atmosphere, temperature and time. The top layer should be etched to obtain the electron doped C12A7 layer.

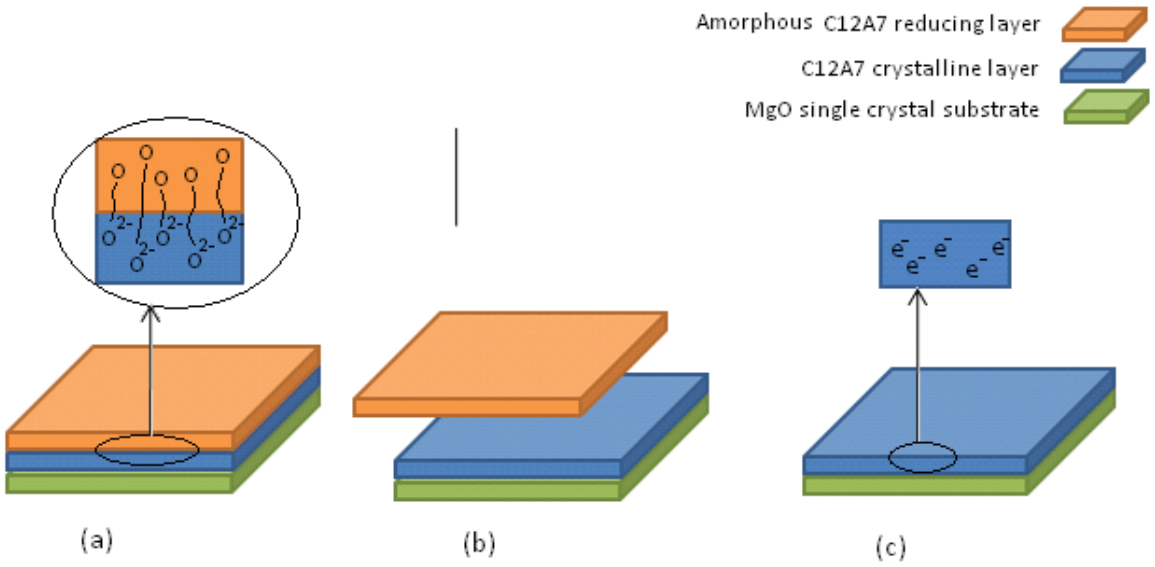

Figure 7.1: A model for electron doping of C12A7 by sol-gel. (a) Heat treatment for the ejection of oxygens to the reducing amorphous C12A7 reducing layer, (b) etching the amodphous layer, (c) electron doped C12A7 thin film.

Such approach can produce high quality conductive layer with possible control over the amount of electron incorporation and further conductivity. Adjusting the conductivity of C12A7 allows the application of this layer for different purposes.

Incorporating electrons into the nano-caged structure of C12A7 introduces novel approaches toward the fabrication of Field Effect Transistor (FET). Semiconducting C12A7 has the potential to be used as the channel semiconductor in FET structures, as explained by *Kamiya et al (2005)* [12]. Insulating C12A7 shows high levels of electrical resistance and can be regarded as a good dielectric oxide. Further investigation into the dielectric properties of C12A7 is required to confirm the suitability of this material as gate insulator. Figure 7.2 shows a model for the

fabrication of FET using both semiconducting and insulating C12A7 as channel and gate insulator respectively.

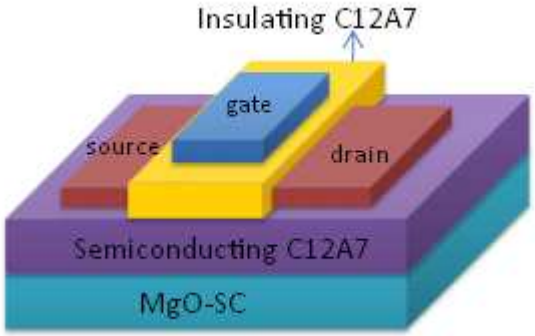

Figure 7.2: Field Effect Transistor structure using C12A7 with different conductivity levels.

Such approach provides better semiconductor-to-insulator interface. Due to similarities in the lattice parameter and structure, the strain at the interface will be minimized and the energy band offset of both conduction and valence band is believed to be small. The highest conductivity of electron doped C12A7 reported up to present is limited to 1500 Scm^{-1}, which is very small compared to that of platinum (9.4×10^6 S m^{-1}). In has been reported that Pt would make good ohmic contact with semiconducting C12A7 [12], but if the metallic conductivity can be enhanced in C12A7 it may be possible to replace Pt with C12A7 as the source and drain.

Another interesting aspect of the current study is the possibility to induce conductivity in amorphous C12A7. C12A7 dried gel has a number of chemicals due to sol-gel processing as confirmed by FTIR and Raman spectroscopy measurements. If

the dried gel is thermally treated to temperature high enough to remove the residual chemicals from the gel, it is possible to use it as the amorphous C12A7. Comprehensive studies into this subject may open new frontiers to obtain semiconducting amorphous C12A7 layers. The main advantage of such approach would be the possibility to utilize a wide range of substrates.

REFERENCES

1. Kamiya T, Hosono H Semicond. Sci. Technol. 20 S92-S102

2. T Kamiya, K Ueda, H Hiramatsu, H Kamioka, H Ohta, M Hirano H Hosono 2005 Thin Solid Films 486 98-103

3. J E Medveda, A J Freeman 2005 Europhysic. Lett. 69 583-587

4. Kamiya T, Hiramatsu H, Nomura K, Hosono H 2006 J. Electroceram. 17 267-275

5. K Nomura, H Ohta, K Ueda, T Kamiya, M Hirano, H Hosono 2003 Science 300 1269-1272

6. P V Shushko, A L Shluger, K Hayashi, M Hirano, H Hosono 2003 Thin Solid Films 445 161-167

7. S Matsuishi, S W Kim, T Kamiya, M Hirano, H Hosono 2008 J. Phys. Chem. C. 112 4753-4760

8. E Feldbach, V P Denks, M Kirm, P Libik, A Maaroos, H Mandar, T Avarmaa. K Kunnus 2009 J. Mater. Sci: Mater. Electron. 20 260-263

9. E Feldbach, V P Denks, M Kirm, P Libik, A Maaroos, L Matisen, A Saar, K Kunnus 2007 VUV Spectrsocopy of Nitrogen Treated C12A7 Hasylab Annual Report 2007

10. A Chatterjee, M Nishioka, F Mizukami 2004 Chemical Physics Letters. 390 335-339

11. Y Kohama, S W Kim,T Tojo, H Kawaji, T Atake, S Matsuishi, H Hosono 2008 Phys. Rev. B. 77 092505

12. T Kamiya, S Aiba, M Miyakawa, K Nomura, S Matsuishi, K Hayashi, K Ueda, M Hirano, H Hosono 2005 Chem. Mater. 17 6311-6316

13. M Miyakawa, K Ueda, T Kamiya, M Hirano, H Hosono 2007 J. Ceram. Soc. Jpn 115 No. 9 567-570

14. S W Kim, Hayashi K, Hirano M, Hosono H 2006 J. Am. Ceram. Soc. 89 3294-3298

15. P V Shushko, A L Shluger, Hayashi K, Hirano M, H Hosono 2003 Phys. Rev. Lett. 91 12

16. Y Toda, S W Kim, K Hayashi, M Hirano, T Kamiya, H Hosono 2005 Appl. Phys. Lett. 87 254103

17. Y Toda, H Yanagi, E Ikenaga, J J Kim, M Kobata, S Ueda, T Kamiya M Hirano, K Kobayashi, H Hosono 2007 Adv. Mater. 19 3564-3569

18. K B Kim, M Kikuchi, M Miyakawa, H Yanagi, T Kamiya, M Hirano, H Hosono 2007 J. Phys. Chem. C. 111 No. 24 8403-8406

19. Y Nishio, K Nomura, M Miyakawa, K Hayashi, H Yanagi, T Kamiya, M Hirano, H Hosono 2008 Phys. Stat. Sol. (a). 205 No.8 2047-2051

20. S W Kim, S Matsuishi, M Miyakawa, K Hayashi, M Hirano, H Hosono 2007 J. Mater. Sci: Mater. Electron 18: S5-S14

21. M Miyakawa, K Hayashi, M Hirano, Y Toda, T Kamiya, H Hosono 2003 Adv. Mater. 15 No. 13 1100- 1103

22. C.H. Jung, P.H. Tai, Y.K. Kang, D.S. Jang and D.H. Yoon 2008 Surface and Coatings Technology. 202 5421-5424

23. M Lacerda, J T S Irvine, F P Glasser, A R West 1988 Nature 332 525-526

24. M Miyakawa, Y Toda, K Hayashi, M Hirano, T Kamiya, N Matsunami, H Hosono 2005 J. Appl. Phys. 97 023510

25. K Hayashi, M Hirano, H Hosono 2007 Bull. Chem. Soc. Jpn. 80 No. 5 872-884

26. S W Kim, Y Toda, K Hayashi, M Hirano, H Hosono 2006 Chem. Mater. 18 1938-1944

27. J B Laughlin, J L Sarquis, V M Jones, J A Cox 2000 J. Chem. Edu. 77 No. 1 77-79
28. S Gorer, G Hodes, Y Sorek, R Reisfeld 1997 Mater. Lett. 31 209-214

29. Y Kobayashi, T Ishizaka, Y Kurokawa 2005 J. Mater. Sci. 40 263-283

30. A C Tas 1998 J.Am. Ceram. Soc. 81 2853-2863

31. H Hosono, Y Abe 1987 Inorg. Chem. 26 1192-1195

32. V K Singh, K K Sharma 2002 J. Am. Ceram. Soc. 84 769-772

33. Satoshi Watauchi, Isao Tanaka, Katsuro Hayashi, Masahiro Hirano, Hideo Hosono 2002 Journal of Crystal Growth 237-239 801-805

34. S Matsuishi, Y Toda, M Miyakawa, K Hayashi, T Kamiya, M Hirano, I Tanaka, H Hosono 2003 Science 301 626-629

35. J E Medvedeva 2007 Applied Physics A: Materials Science & Processing. 89 No. 1 43-47

36. A A Goktas, M C Weinberg 1991 J. Am. Ceram. Soc. 74 No. 5 1066-1070

37. Yutaka Adachi, Sung-Wng Kim, Toshio Kamiya, Hideo Hosono 2009 Mater. Sci. Eng. B. 161 76-79

38. P V Shushko, A L Shluger, K Hayashi, M Hirano, H Hosono 2006 Phys. Rev. B. 73 014101

39. H Harimochi, J Kitagawa, M Ishizaka, Y Kadoya, M Yamanishi, S Matsuishi, H Hosono 2004 Phys. Rev. B. 70 193104

40. P M Nikolic, D Lukovic, S Savic, D Urosevic, S Djuric 2003 Science of Sintering 35 147-154

41. P V Shushko, A L Shluger, M Hirano, H Hosono 2007 J. Am. Chem. Soc. 129 942-951

42. N Sakamato, T Watanabe, M Yoshimura 2006 Int. J. Appl. Ceram. Technol. 3 No.4 266-271

43. Y Toda, M Miayawa, K Hayashi, T Kamiya, M Hirano, H Hosono 2003 Thin Solid Films 445 309-312

44. Q Li, H Hosono, M Hirano, K Hayashi, M Nishioka, H Kashiwagi, Y Torimoto, M Sadakata 2003 Surface Science 527 100-112

45. S Yang, J N Kondo, K Hayashi, M Hirano, K Domen, H Hosono 2004 Chem. Mater. 16 104-110

46. H Hosono 2004 Sci. Technol. Adv. Mater. 5 409-416

47. K Hayashi, M Hirano, S Matsuishi, H Hosono 2002 J. Am. Chem. Soc. 124 No. 5

48. Q. X. Li, K. Hayashi, M. Nishioka, H. Kashiwagi, M. Hirano, Y. Torimoto, H. Hosono, and M. Sadakata 2002 Appl. Phys. Lett. 80, 4259-4261

49. K Hayashi, S Matsuishi, T Kamiya, M Hirano, H Hosono 2002 Nature 419 No. 3 462-465

50. H Kamioka, H Hiramatsu, K Hayashi, M Hirano, H Hosono 2004 Journal of Photochemistry and Photobiology A: Chemistry 166 141-147

51. M I Bertoni, T O Mason, J E Medvedeva, A J Freeman, K R Poeppelmeier, B Delley 2005 J. Appl. Phys. 97 103713

52. P V Shushko, D M Ramo, A L Shluger 2007 Phys. Stat. Sol. (a) 204 No. 3 663-669

53. J E Medvedeva A J Freeman 2004 Appl. Phys. Lett. 85 No. 6 955-957

54. T Kamiya, H Ohta, H Hiramatsu, K Hayashi, K Nomura, S Matsuishi, K Ueda, M Hirano, H Hosono 2002 Microelectronic Engineering 73-74 620-626

55. P V Shushko, A L Shluger, M Hirano, H Hosono 2008 Thin Solid Films 516 1350-1352

56. M Miyakawa, M Hirano, T Kamiya, H Hosono 2006 Nucl. Instr. and Meth. in Phys. Res. B. 250 155-158

57. Y Toda, S Matsuishi, K Hayashi, K Ueda, T Kamiya, M Hirano, H Hosono 2004 Ad. Mater. 16 No. 8 685-689

58. M Miyakawa, H Kamioka, M Hirano, T Kamiya, P V Shushko, A L Shluger, N Matsunami, H Hosono 2006 Phys. Rev. B. 73 205108

59. M Miyakawa, H Kamioka, M Hirano, T Kamiya, H Hosono 2006 Nucl. Instr. and Meth. in Phys. Res. B. 250 368-371

60. H Hosono, S W Kim, M Miyakawa, S Matsuishi, T Kamiya 2008 Journal of non-Crystalline Solids 354 2772-2776

61. M Miyakawa, M Hirano, T Kamiya, H Hosono 2007 Appl. Phys. Lett. 90 182105

62. Yasuyuki Mizushima, Makoto Hori, Minoru Sasaki 1993 J. Mater. Res. 8 2109-2111

63. L B Coury, F Babonneau, J Livage 1994 J. sol-gel. Sci. Technol. 3 157-168

64. Y Mizushima, M Hori 1993 J. Mater. Res. 8 No. 11 2993-2999

65. B Himmel, Th Gerber, H Burger, G Holzhuter, A Olbertz 1995 Journal of non-Crystalline Solids. 186 149-158

66. J Escobar, J A De Los Reyes, T Viveros 2003 Applied Catalysis A: General. 253 151-163

67. L Shi, N B Wong 1999 J. Mater. Res. 14 No. 9 3599-3603

68. Xia Changrong, Wu Feng, Meng Zhaojing, Li Fanqing, Peng Dingkun, Meng Guangyao 1996 Journal of Membrane Science. 116 9-16

69. J. Ma, C. H. Liang, L. B. Kong and C. Wang 2003 Journal of Materials Science: Materials in Medicine 14 797-801

70. J Campaniello, P Berthet, F d'Yvire, A Revcolevschi 1995 J. Mater. Res. 10 No. 2 297-301

71. J Garcia Sole, L E Bausa, D Jaque 2005 *An Introduction to the Optical Spectroscopy of Inorganic Solids.* UK, John Wiley and Sons, Ltd pp: 1-38

72. M Fox 2001 *Optical Properties of Solids*. USA, Oxford University Press pp: 1-24

73. R P Bauman 1962 *Absoprtion Spectroscopy*. USA, John Wiley and Sons, Ltd pp: 1-25

74. Elliot 1969 *Infrared Spectra and Structure of Organic Long-chain Polymers*. UK, Edward Arnold Ltd pp: 1-7

75. H A Szymenski 1967 *Raman Spectroscopy: Theory and Practice*. USA, Plenum Press pp: 1-43

76. R E Benner, J R Mitchel, R W Grow 1987 IEEE Transactions on Electron Devices ED-34 No. 8 1842- 1847

77. C Kittel *2005 Introduction to Solid State Physics*. USA, John Wiley and Sons, Ltd pp: 23-43

78. B D Cullity, S R Stock 2001 *Elements of X-Ray Diffraction*. USA, Prentice Hall pp: 89-122

79. E Smith, G Dent 2005 *Modern Raman Spectroscopy.* UK, John Wiley and Sons, Ltd pp: 1-23

80. S D Ross 1972 *Inorganic Infrared and Raman Spectroscopy*. UK, McGraw-Hill Book Company Ltd pp: 95-112

81. K Nakanishi 1962 *Infrared Absorption Spectroscopy*. Japan, Nankodo Company Ltd pp: 1-57

82. Elliot 1969 *Infrared Spectra and Structure of Organic Long-chain Polymers*. UK, Edward Arnold Ltd pp: 83-106

83. S D Ross 1972 *Inorganic Infrared and Raman Spectroscopy*. UK, McGraw-Hill Book Company Ltd pp: 140-185

84. W Dan, L I Yuxue, X Changshan, L I Yichin, W G Uorui, L I Xinghua 2008 Journal of Rare Earths. 26 No. 3 433-438

85. C J Brinker, G W Scherer *Sol-Gel Science: The Physics and Chemistry of Sol-Gel Processing.* USA, Academic Press. Inc pp: 1-17

86. Pierre A C 1998 *Introduction to Sol-Gel Processing.* USA, Kluwer Academic Press pp: 2-8

87. A Garbout, S Bouattour, A W Kolsi 2007 Journal of Crystal Growth 307 219-228

88. A Jianu, L Stanciu, J R Groza, Ch Groza, Ch Latte, E Burkel 2003 Nucl. Instr. and Meth. in Phys. Res. B. 199 44-48

89. Q Meng, J Lin, L Fu, H Zhang, S Wang, Y Zhou 2001 J. Mater. Chem. 11 3382-3386

90. J D Wright, N A J M Sommerdijk 2001 *Sol-Gel Materials: Chemistry and Applications.* The Netherlands, Gordon and Breach Science Publishers pp: 1-14

91. C J Brinker, G W Scherer *Sol-Gel Science: The Physics and Chemistry of Sol-Gel Processing.* USA, Academic Press. Inc pp: 453-509

92. C J Brinker, G W Scherer *Sol-Gel Science: The Physics and Chemistry of Sol-Gel Processing.* USA, Academic Press. Inc pp: 787-835

93. C J Brinker, G W Scherer *Sol-Gel Science: The Physics and Chemistry of Sol-Gel Processing.* USA, Academic Press. Inc pp: 675-738

94. Mahyar Mazloumi, Razieh Khalifehzadeh, S. K. Sadrnezhaad, Hamed Arami 2006 J. Am. Ceram. Soc. 89 3654-3657

95. E Garreta, T Fernandez, S Borros, J Esteve, C Colominas, L Kempf 2002 Mat. Res Soc. Symp. Proc. 724 No. 8.11.1

96. W Brockner, Claus Ehrhardt, M Gjikaj 2007 Thermochimica Acta 456 64-68

97. M Thiruchitrambalam, V R Palkar, V Gopinathan Mater. Lett. 58 3063-3066

98. A K Galwey, C Ettarh 1998 Thermochimica Acta 316 57-73

99. E E Assem 2005 J. Phys. D: Appl. Phys. 38 942-945

100. J H Lienhard IV 2003 A Heat Transfer Textbook USA Phlogiston Press pp: 141-193

101. H Mandar, J Felsche, V Mikli, T Vajakas 1999 J. Appl. Crys. 32 345-350

102. N B Chaure, A K Ray, R Capan 2005 Semicond. Sci. Technol. 20 788-792

103. C Kittel *2005 Introduction to Solid State Physics*. USA, John Wiley and Sons, Ltd pp: 161-182

104. M Fox 2001 *Optical Properties of Solids*. USA, Oxford University Press pp: 92-108

105. L E Shea 1996 *The Essence of Solid-State Electronics*. UK, T. J. Press pp: 115-135

106. C Kittel *2005 Introduction to Solid State Physics*. USA, John Wiley and Sons, Ltd pp: 131-157

107. E O'Reilly 2002 *Quantum Theory of Solids.* UK, Taylor and Francis Group pp: 95-128

108. M Fox 2001 *Optical Properties of Solids*. USA, Oxford University Press pp: 271-280

109. Knief S, W von Niessen 1999 Phys. Review B 59 12940-12946

110. A.F. Maged, A.M. Sanad, M.F. El-Fouly, G.A.M. Amin 1998 J. Mater. Res. 13 1128-1131

111. M M I Khalil, G M Nasr, N M El-Sawy 2006 J. Phys. D: Appl. Phys. 39 5305-5309

112. N F Mott, E A Davis 1979 *Electronic Processes in non-Crystalline Materials*. UK, Clarendon Press pp: 199-314

113. A K Ray, C A Hogarth 1990 J. Phys. D: Appl. Phys. 23 458-459

114. A K Ray, S M Tracey, B McQuillin, S N B Hodgson IEE Proc.-Sci. Meas. Technol. 147 No. 6 301-305

115. A. Majumdar, H. Z. Xu, F. Zhao, J. C. Keay, L. Jayasinghe, S. Khosravani, X. Lu, V. Kelkar, and Z. Shi 2004 J. Appl. Phys. 95, 939-942

116. S A Khan, M Zulfequer, M Husain 2002 Physica B. 324 336-343

117. M Daviti, K M Paraskevopoulos 1999 Mater. Res. Bull. 34 No. 3 381-388

118. S L O'Leary, S R Johnson, P K Lim 1997 J. Appl. Phys. 82 No. 7 3334-3340

119. S M Wasim, G Marin, C Rincon, P Bocaranda, G Sanches Perez 2000 J. Phys. Chem. Sol. 61 669-673

120. M Kranjecec, I P Studenyak, M V Kurik 2009 Journal of non-Crystalline Solids. 355

121. M Kranjcec, I P Studenyak, G S Kovacs, VV Mitrovcij, M I Gurzun, Y V Voroshilov 2002 Mater. Res. Bull. 37 2499-2507